SISSA
Scuola
Internazionale
Superiore di
Studi Avanzati

Mathematics Area - PhD course in
Mathematical Analysis, Modelling, and Applications

Fluid structure interaction problems involving thin active shells and microswimmers

Candidate:
Giovanni Corsi

Advisor:
Prof. Antonio DeSimone

Academic Year 2019-20

Abstract

In this thesis some fluid-structure interaction problems related to swimming are investigated. The broad domain in which the cases can be classified is that of swimming at low-Reynolds numbers, that is in conditions close to the Stokes flow.

In the first part, a simpler flow configuration is considered together with an active structure, to identify possible swimming strategies arising from deformations of a multi-stable shell. After a first analysis, based on numerical simulations, an asymptotic approach is employed aiming to confirm the results analytically.

In the second part a more complex flow model is considered, in order to analyse a case where the Reynolds number is small but possibly finite. The case considered is that of a robotic swimmer in a viscous fluid, inspired by a celebrated paper of Purcell which is revisited here with more modern tools, from numerical techniques to experiments. Numerical solvers are developed to simulate the related flows: particular care is devoted to the scalability and efficiency of numerical methods in order to solve the Navier-Stokes equations within acceptable time constraints. The validity and accuracy of common models for micro swimmers are assessed by comparison of numerical results with experimental results.

Acknowledgements

I would like to thank Antonio De Simone, my advisor, Corrado Maurini and Stefano Vidoli, for their guidance and support throughout the course of my PhD studies. In particular, I am grateful for Corrado's hospitality at L'Institut Jean Le Rond d'Alembert at l'Université Sorbonne, for my period abroad during the PhD.

I wish to acknowledge as well the computational resources provided by SISSA and Université Sorbonne, which made possible the large-scale computations required for the numerical results of this work.

Contents

Chapter 1

Introduction

An important subfield of fluid structure interaction problems is that of swimming problems. In particular, swimming at low Reynolds numbers is a field of research rich, where more analytical results can be achieved, and more results in closed form can be hoped to be obtained. Loosely speaking, this realm is characterized by weak (or absent) inertial terms in the flow, as can be seen by the flow equations Navier-Stokes in non-dimensional form:

$$Re\left(\frac{\partial \mathbf{u}^*}{\partial t^*} + (\mathbf{u}^* \cdot \nabla^*)\mathbf{u}^*\right) = -\nabla^* p^* + \Delta^* \mathbf{u}^*. \tag{1.1}$$

The setting for swimming problems in general consists of a body in a surrounding fluid, that can generate motion by self deformation, without the action of external forces. The simplest case is that when Reynolds number is precisely zero, and the flow surrounding the swimming body can be described by the Stokes equations:

$$\nu\Delta\mathbf{u} - \nabla p = \mathbf{0}, \tag{1.2}$$

where ν is the kinematic viscosity. This case is of great importance for applications in biology, since these conditions are descriptive of the flow that occurs in the case of micro-organisms, or nano-robots that may reproduce them artificially. The complete absence of inertia, that is reflected also by the linearity of equations (1.2), makes the self-propulsion of a body a non-trivial task. In other words, being able to generate motion in a fluid in the absence of external propulsive forces by performing cyclic shape deformations, is achieved at low Reynolds numbers only by certain non-reciprocal shape-change strategies. The simplest cyclic deformations do not generate net motion, a result that is commonly known as the *Scallop Theorem*. This result is a popular example, introduced by Purcell in his seminal paper [49], to illustrate the phenomenon. Briefly, a body (for example a micro-organism) that deforms with a reciprocal stroke akin to that of a scallop (periodical opening and closing of the valves), doesn't move on average over time. This stroke has the characteristic of being described mathematically by a single degree of freedom in time. The result is in stark contrast with what would happen at high Reynolds, where the inertia would play a role and a different flow would be generated, allowing for self-propulsion. Following Alouges and DeSimone [21], if the motion of a swimmer can be described by a law:

$$\dot{c}(t) = V(\xi(t))\dot{\xi}(t), \tag{1.3}$$

then for every periodic stroke ξ, with period T, holds:

$$\Delta c = \int_0^T \dot{c}(t)\mathrm{d}t = 0, \tag{1.4}$$

where it is assumed that all functions involved have sufficient regularity. Therefore, a deformation pattern that is too *naive* does not generate any net motion. The most immediate

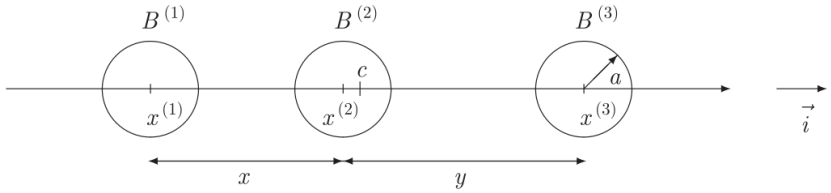

FIGURE 1.1: Representation of a three sphere swimmer in Stokes flow, from [21, 3].

extension of the swimming strategy is that to add another degree of freedom to the deformation: a simple swimmer that exemplifies this configuration is the three sphere swimmer as shown in figure 1.1. This swimmer has two degrees of freedom (denoted as x and y in this case), which can be actuated independently. If one considers the space of admissible shapes, the Scallop Theorem has an immediate graphic description, that is the loop described over one period by the two degrees of freedom must have non-zero area in order to generate a net motion over time. If again $\dot{c}$ denotes the velocity of the centre of mass of the swimmer, then the dynamics of the swimmer can be described by the relation:

$$\begin{pmatrix} f^{(1)} \\ f^{(2)} \\ f^{(3)} \end{pmatrix} = R(x,y) \begin{pmatrix} u^{(1)} \\ u^{(2)} \\ u^{(3)} \end{pmatrix}, \tag{1.5}$$

where u is the velocity of one of the three balls and f the corresponding force acting on it. The relation is given by the matrix R, dependent on the shape, that is symmetric and positive definite. These properties of the matrix derive directly from the flow, and the variational structure of the Stokes equations that govern it. The solution of Stokes flow is the one minimizing the viscous dissipation. Symmetry is a property of reciprocity deriving from linearity and self-adjointness. Positive-definiteness follows from positivity of the viscous dissipation. The dependence of the velocities on the two degrees of freedom is given by:

$$u^{(1)} = \dot{c} - \tfrac{1}{3}(2\dot{x} + \dot{y}), \tag{1.6}$$
$$u^{(2)} = \dot{c} + \tfrac{1}{3}(\dot{x} - \dot{y}), \tag{1.7}$$
$$u^{(3)} = \dot{c} + \tfrac{1}{3}(2\dot{x} + \dot{y}). \tag{1.8}$$

The system can now be solved by introducing the relation $f^{(1)} + f^{(2)} + f^{(3)} = 0$. This is due to the absence of external forces acting on the swimmer, and to the absence of inertia when the Reynolds number of the flow is zero. The system can thus be solved and the general form for the solution is

$$\dot{c} = V_x(x,y)\dot{x} + V_y(x,y)\dot{y}. \tag{1.9}$$

The displacement during one stroke γ, where γ is the boundary of a region ω of the space of admissible shapes, can now be calculated

$$\Delta c = \int_0^T (V_x\dot{x} + V_y\dot{y})\mathrm{d}t = \int_\omega \mathrm{curl}V(x,y)\mathrm{d}x\mathrm{d}y. \tag{1.10}$$

As expected, the net displacement after one stroke will be non-zero only if the shape change describes a curve in the space of admissible shapes which delimits a region of non-zero area. An example of such stroke is reported in figure 1.2, taken from [21], where the optimal stroke is also depicted. Another classic example of swimmer at low Reynolds numbers is Taylor's

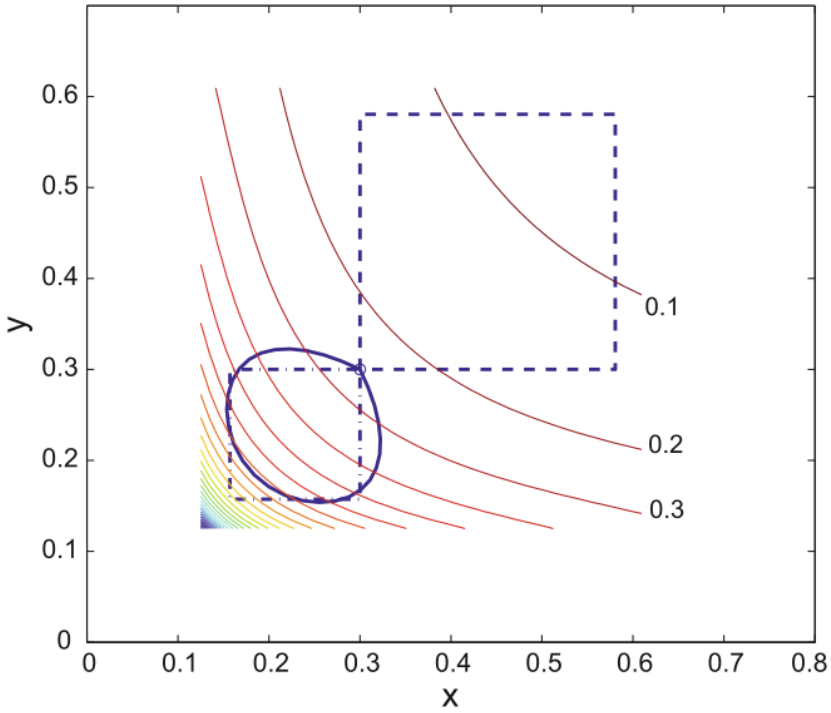

FIGURE 1.2: Possible strokes for the three sphere swimmer, which generate net motion, from [21, 3]. The optimal stroke is also represented.

sheet [59] which is the prototype of a flagellum found in many micro-organisms. This swimmer will be the basic starting point for the first two chapters of this thesis. Here a brief summary of the solution strategy of G.I. Taylor to obtain the solution will be reported. The flow is two-dimensional and Stokesian, while the sheet extends along the x-axis. Let us consider for simplicity the case of a travelling wave of bending propagating along the body, that is

$$y_B = b \sin \xi, \qquad \xi = kx - \omega t, \tag{1.11}$$

resulting in the following boundary conditions for the flow at the surface of the body:

$$u(x_B, y_B, t) = 0, v(x_B, y_B, t) = -b\omega \cos \xi. \tag{1.12}$$

It is important to note that the boundary condition due to the sheet has to be imposed at a position which is moving over time [12]. The Stokes equations in a two-dimensional setting imply that there exists a function ϕ such that

$$u = \frac{\partial \phi}{\partial y}, \qquad v = -\frac{\partial \phi}{\partial x}, \tag{1.13}$$

where the function ϕ will be biharmonic, that is

$$\nabla^4 \phi = 0. \tag{1.14}$$

Choosing a co-moving frame, the additional boundary conditions for the problem to be solved will therefore be, for the half-space $y \geq 0$:

$$\frac{\partial \phi}{\partial y} \to U, \qquad y \to +\infty, \tag{1.15}$$

$$\frac{\partial \phi}{\partial x} \to 0, \qquad y \to +\infty. \tag{1.16}$$

In equation (1.15) we allow for the velocity to tend to a finite constant and unknown value at infinity. This will emerge as the problem is solved and will be precisely the swimming velocity generated by the sheet. With the assumption that the amplitude of the travelling wave be small, the solution of the problem can be sought as a power series in the non-dimensional parameter bk. A general solution of the biharmonic equation, vanishing at infinity, is [11]:

$$V_n = (A_n + kB_n y)e^{-nky} \sin n(kx - \omega t) + (C_n + kD_n y)e^{-nky} \cos n(kx - \omega t), \tag{1.17}$$

and the potential function of the solution, in increasing powers of bk, will be:

$$\phi = \phi^{(1)} + \phi^{(2)} + \dots, \tag{1.18}$$

where the different powers will be given by the contributions of the general solutions of the biharmonic equation:

$$\phi^{(1)} = V_1^{(1)} + U^{(1)} y, \tag{1.19}$$

$$\phi^{(2)} = V_1^{(2)} + V_2^{(2)} + U^{(2)} y, \tag{1.20}$$

$$\dots. \tag{1.21}$$

Substituting the expressions of the solutions and retaining only the terms at order bk gives:

$$\phi_\xi^{(1)}(\xi, 0) = A_1^{(1)} \cos \xi - C_1^{(}1) \sin \xi = \frac{b\omega}{k} \cos \xi, \qquad U^{(1)} = 0, \tag{1.22}$$

therefore resulting in the expression

$$\phi^{(1)} = \frac{\omega}{k} \left[(b + b\eta) e^{-\eta} \sin \xi \right], \tag{1.23}$$

where $\eta = ky$. Thus, the sheet does not swim to order bk. It is necessary to solve for the next power, at order b^2k^2, to obtain a non-zero term $U^{(2)}$, which, after taking the ξ average, results in the expression:

$$U \simeq U^{(2)} = \frac{1}{2} \omega k b^2. \tag{1.24}$$

The sheet is thus able to generate a swimming motion as a second-order effect.

1.1 Finite Reynolds numbers

When the Reynolds number of the flow is low but finite, inertia starts to play a role. An effect which is immediately visible is the loss of fore-aft symmetry in the flow surrounding a fore-aft symmetric translating body, where the classic wake starts to form. The drag exerted on a swimming body will have a further contribution, in addition to the viscous one, that is generally named *pressure drag*. Moreover, when the Stokes approximation holds, time-dependent terms are obviously zero, implying that the fluid will always instantly react and adjust to any variations in velocity of the body, with no inertial forces arising in the instantaneous transients. If, on the other hand, this approximation ceases to hold, variations of the velocity

of the body (during transient motions) will cause a fluid to react with an opposing force due to the mass of it being displaced and accelerated. This reaction is usually called *added mass* in the context of inviscid potential flows, when it can be shown that the reacting force can be seen as an additional inertial force for the body, depending on the mass of fluid that has to be displaced. The concept of added mass, that is defined for potential flow, is also useful when viscosity is present, since for time scales tending to zero, the instant reactions of the flow can still be modelled by the same idea [51].

An important class of problems for low Reynolds flows is that of freely falling, or rising, objects in an unbounded fluid. The objects considered in the literature are mainly those of regular shape like spheres and discs with variable thickness. In this case, the non-dimensional numbers that describe the physics of the flow are slightly different. The factors that determine the flow are gravity force, viscosity and density ratio between the body and the fluid. The latter plays a role also in the importance of added mass effects. The falling or rising velocity is generally unknown a priori, and the Reynolds number cannot be estimated without solving for the flow. A better suited non-dimensional number is thus the Galileo number, defined as:

$$G = \frac{\sqrt{|1 - \frac{\rho_s}{\rho_f}|V^* g d^3}}{\nu}, \tag{1.25}$$

where V^* is the non-dimensional volume of the body, and is equal to 1 for the case of the sphere. The geometry of the body, the Galileo number and the density ratio $\overline{\rho}$ completely determine the flow. The Reynolds number can be defined using the average velocity, known once the solution has been obtained:

$$Re_m = \frac{V_m d}{\nu}. \tag{1.26}$$

Taking as reference the study of Auguste and Magnaudet [5] of freely rising spheres, three different regimes can be identified from the values of the non-dimensional numbers: the case of *heavy* spheres, that is $\overline{\rho} \gg \frac{1}{2}$, intermediate density ratios $G^{-1/2} \ll \overline{\rho} \ll \frac{1}{2}$, and very light bodies $\overline{\rho} \ll G^{-1/2}$. In the first regime, non-instantaneous fluid stresses (that is, stresses of the fluid due to added mass) and body inertia dominate the physics. In the second intermediate regime the acceleration of the fluid also plays a dominant role, for the evolution of the body velocities, while the rotational dynamics are still controlled by the moment of inertia of the body. The last regime, instead, shows completely different behaviours, due to the fact that the fluid acceleration also controls the rotational dynamics of the body, through the viscous process in the Stokes layer [5]. This layer is where the instantaneous effects due to viscosity of the fluid, when the swimming body is accelerating, are non-negligible. This classification also confirms that the inertial effects in the fluid can be described with added mass terms, even if viscosity is present. The viscous stresses have a dominant effect on the flow only if the density ratio is low, as is the case of very light spheres studied in literature. These different mechanisms of interaction between viscosity and inertia of the body and of the fluid determine vastly differing regimes of ascension or fall of a body in a fluid. An example is reported in figure (1.3), for bodies of spherical shape. Increasing the Galileo number, the following regimes can be observed: the starting point is simply a steady vertical trajectory. At slightly higher Galileo numbers the first variation encountered is that of oblique trajectories: steady and oblique (denoted by + in figure) or oblique and oscillating with small amplitude and either low (symbol $*$) or high ($\times$) frequency. Increasing further the Galileo numbers, zigzagging trajectories are observed ($\circ$ in figure), an example of such trajectory is given in figure (1.4). The right-most points represent three-dimensional and chaotic regimes. Another classic case is that of falling or ascending discs: the problem is slightly more complex due to the loss of spherical symmetry, however the regimes of motion observed are similar to those of spherical

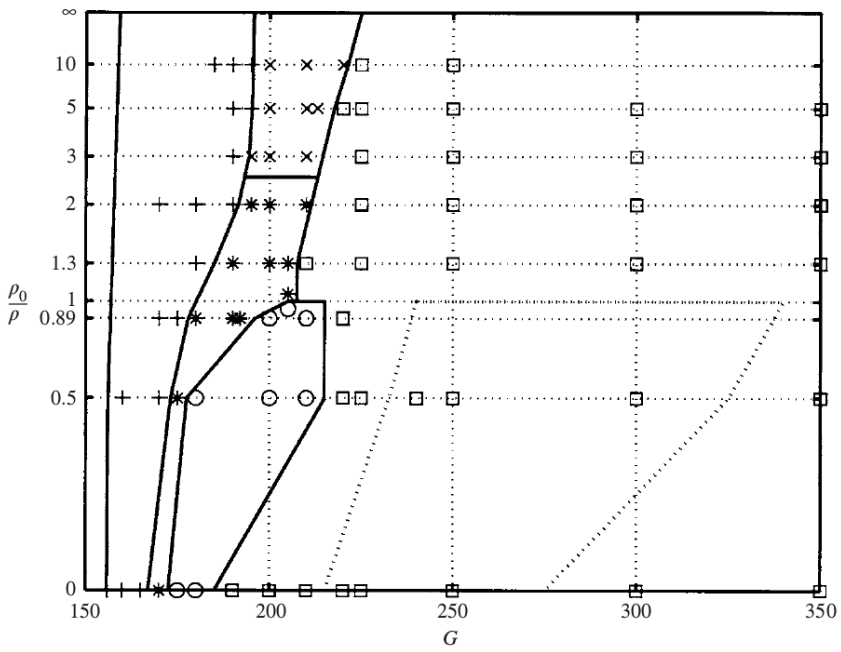

FIGURE 1.3: Different states for the free fall or free ascension of a sphere in a viscous fluid, from [35].

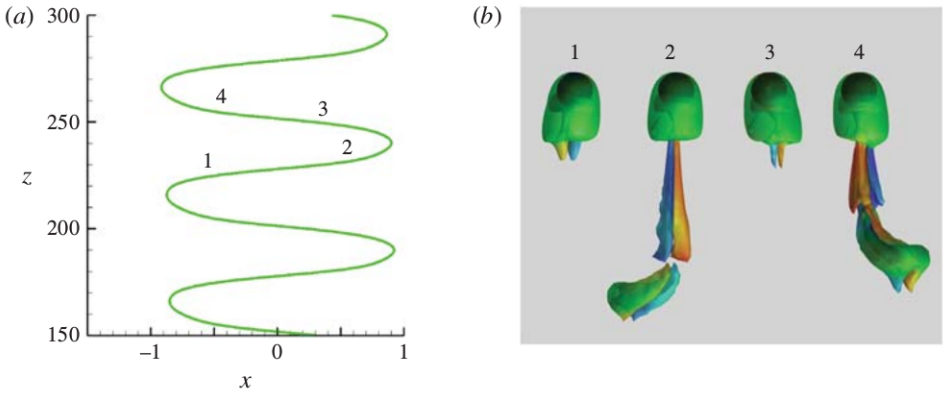

FIGURE 1.4: Different states for the free fall or free ascension of a sphere in a viscous fluid, from [5].

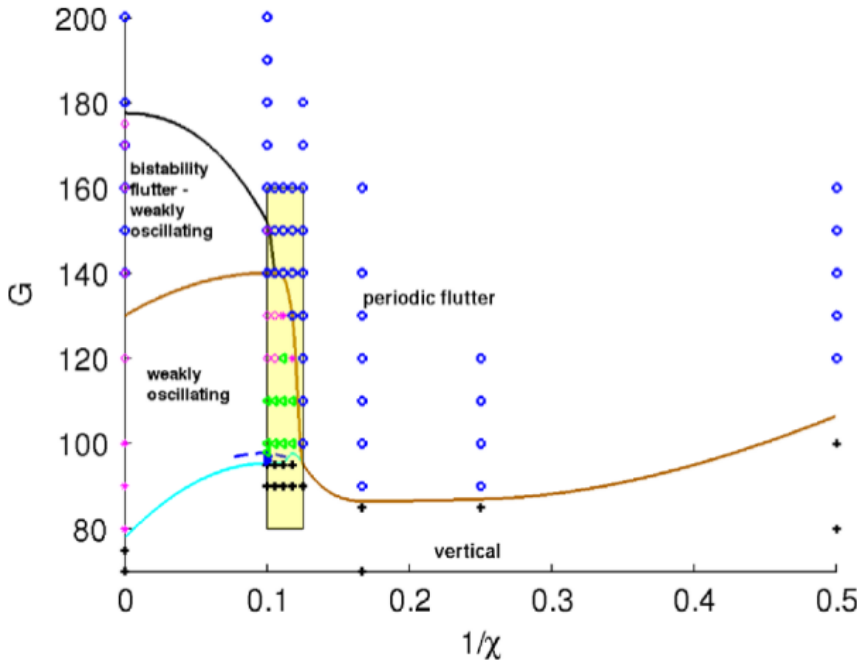

FIGURE 1.5: Different states for the free fall or free ascension of discs for different aspect ratios, from [13].

objects. This introduces another non-dimensional number for the flow, that is the aspect ratio $\chi = d/h$. For lower Galileo numbers, steady vertical or oblique paths will be observed, while for higher values the motion will become oscillating with a zigzagging path. An example, taken from [13] is given in figure (1.5), for varying ranges of aspect ratio χ and a density ratio $\overline{\rho} = 0.99$.

1.2 Outline of the work

The topics presented so far are the background for the work in this thesis. In chapter 2 the swimming problem of a thin shell in Stokes flow is studied, looking for analogies with the swimmer proposed by Taylor. The contents of this chapter are taken from [17].

In chapter 3 the analogy with the solution of Taylor's sheet is further investigated analytically by using an asymptotic approach.

In chapter 4 a different problem, inspired by the work of Purcell is studied: a prototypical robotic swimmer, inspired by the shape of flagellar micro-swimmers is studied both numerically and experimentally. Free-falling experiments play a crucial role in Purcell's protocol to predict the performance of a robotic flagellar swimmer starting from the hydrodynamic properties of the cargo (the head) and of the flagellar propeller. In spite of being a well studied problem of great relevance for current research on biomedical applications of bio-inspired micro-robotics, a quantitative analysis combining theory, numerical simulation and experiments is attempted here for the first time.

Chapter 2

A neutrally stable shell in a Stokes flow: a rotational Taylor's sheet

2.1 Abstract

In a seminal paper published in 1951, Taylor studied the interactions between a viscous fluid and an immersed flat sheet which is subjected to a travelling wave of transversal displacement. The net reaction of the fluid over the sheet turned out to be a force in the direction of the wave phase-speed. This effect is a key mechanism for the swimming of micro-organisms in viscous fluids. Here, we study the interaction between a viscous fluid and a special class of non-linear morphing shells. We consider pre-stressed shells showing a one-dimensional set of neutrally-stable equilibria with almost cylindrical configurations. Their shape can be effectively controlled through embedded active materials, generating a large-amplitude shape-wave associated to precession of the axis of maximal curvature. We show that this shape-wave constitutes the rotational analogue of a Taylor's sheet, where the translational swimming velocity is replaced by an angular velocity. Despite the net force acting on the shell vanishes, the resultant torque does not. A similar mechanism can be used to maneuver in viscous fluids.

2.2 Introduction

The problem of locomotion at low Reynolds numbers has been initiated by the groundbreaking paper of G.I. Taylor [59], which has had an enormous impact and continue to motivate a substantial amount of research (see e.g. [39], the references cited therein, and the more than one thousand references that have cited this review paper since its publication ten years ago).

The model proposed by Taylor is one of the simplest (and yet enlightening) examples of swimming through low Reynolds number flows that can be treated analytically. In [59], he considered the self-propulsion mechanism of a two-dimensional sheet, immersed in a viscous fluid, on which waves of transversal displacement propagate. Assuming these waves have small amplitude, a perturbative expansion of the boundary conditions can be used to compute the swimming speed of the oscillating sheet. In more detail, if an unbounded fluid is considered, and the undeformed sheet coincides with the plane $y = 0$, the travelling wave propagating in the x direction will cause a vertical displacement

$$y_0 = b \sin(k(x - vt)), \tag{2.1}$$

where b is the amplitude, k the wave number and v is the wave phase speed. In a reference frame moving with the sheet, the boundary condition on the velocity of the fluid in contact with the sheet [39] will be:

$$\mathbf{u}(x, y_0(x, t)) = -bkv \cos(k(x - vt))\mathbf{e}_y, \tag{2.2}$$

while it is expected that infinitely far from the sheet a uniform and steady flow will be observed

$$\lim_{y\to\infty} \mathbf{u}(x,y) = -U\mathbf{e}_x, \tag{2.3}$$

where U is the swimming speed of the sheet. With this choice of frame, the swimming speed appears as an unknown boundary condition for the problem. Given the assumption of small amplitude, Taylor shows that expanding the boundary condition (2.2) in powers of the dimensionless parameter bk, and knowing the form of the general solution for the 2D Stokes flow, one can solve the problem approximating U with an increasing order of accuracy. The problem, as posed, is therefore closed even if the unknown appears as a boundary condition. Up to second order terms in bk, this velocity is

$$U = -\frac{1}{2}v(bk)^2. \tag{2.4}$$

Taylor's analysis can be used to show that, when deformations are small, travelling waves of bending (resp. stretching) cause translation in the direction opposite (resp. the same direction) to the waves, see [11]. This paradigm has been used innumerable times, for example in [24], which is one of the most popular attempts at reproducing the mechanisms of Taylor sheet in micron-sized artificial systems. In spite of this, there are still subtleties to be clarified when the amplitude of the deformations is large, including the inversion of the sign of the velocity, the possible trajectories and the characterization of optimal beats, see *e.g.* [4, 15].

Several variants of the concept of the Taylor's swimming sheet have been proposed in the literature. Lauga and co-workers extended the Taylor's series expansion of the solution to large amplitudes waves [52] and considered the case of sheet immersed in a viscoelastic fluid [40]. Katz [37] studied the influence of the confinement on the resulting swimming speed, showing that in specific configurations the confinement can improve the swimming efficiency. The case of bending waves in cylinders was studied by Taylor himself [58] and more recently in [54], whilst [41] deals with a helicoidal geometry. Dasgupta et al.[19] reports interesting experimental results on the case of a cylinder with a rotating wave of radius modulation in viscous and viscoelastic fluids.

In this work, we propose a new rotational analogue of the Taylor's sheet. Our analysis is motivated by the recent, and growing interest in the mechanics of shape-shifting structures [9, 30, 20, 32, 33, 53]. We study a particular class of prestressed thin shells [33], and ask ourselves the question of what happens when these solid shells are immersed in a viscous fluid. As detailed later, these structures (which in the present case will be of circular or elliptical shape) attain, when actuated, a periodic pattern of shape-change, which is characterized by an almost constant curvature. Intuitively, the shell shape is almost cylindrical; its axis of maximal curvature performs a precession over time and the stored elastic energy is almost independent of its orientation. The shell is *neutrally-stable* and its shape can be controlled by a weak embedded actuation [33]. The resulting deformation is the same as the one due to the propagation of a circular wave of displacement, transversal to the plane of the flat configuration of the shell. Thus, the shell can be seen as a rotational version of the Taylor's swimming sheet. The goal of this work is to address whether this device can be used as an artificial swimmer in a viscous fluid. In previous work on helical and cylindrical, see e.g. [54, 41], the use of symmetries and the fact that the structure is infinitely extended in one direction, allowed the authors for the effective reduction of the problem dimension. Instead, in the present case, the structure is finite, the shell deformation breaks the axial-symmetry, and we are forced to study a fully three-dimensional problem. We consider a simplified model for the shell. Assuming that the shell is inextensible and with uniform curvature, we retain a single degree of freedom, corresponding to the orientation of the direction of maximal curvature. In this framework, solving elementary Stokes problems with an adaptive finite element technique, we

calculate the hydrodynamic coefficients modeling the interaction between the structure and the fluid. Hence, we solve the resulting fluid-structure interaction problem when either the structural shape or the actuating forces are prescribed.

In the following, Section 2.3 presents the mechanics of the neutrally-stable shell, along with the relevant notation and the velocity fields generated under actuation. The swimming problem in a Stokes flow is formulated in Section 2.4, while Section 2.5 reports the numerical results. Conclusions are drawn in Section 2.6.

2.3 Neutrally stable cylindrical shells

Several recent works have shown that shell structures can exhibit a particularly rich behavior thanks to the interplay between geometrical non-linearities and pre-stresses. A basic example is the case of an initially flat thin isotropic bimetallic disk $\mathcal{D} := \{X^2 + Y^2 < R^2\}$ of radius R subjected to a temperature loading. Because of the different expansion coefficients of the two layers composing the disk, a uniform temperature loading of the disk induces a uniform isotropic inelastic curvature, say $\bar{\mathbf{k}} = \bar{c}\,\mathbf{I}$, where $\mathbf{I}$ is the 2×2 identity tensor. As shown by [63, 53, 30, 20], for sufficiently large $\bar{c}$, the disk can be modeled as an inextensible but flexible elastic surface, whose shape is characterized by an almost uniform curvature $\mathbf{k}$. The inextensibility condition implies that the Gaussian curvature $\det(\mathbf{k})$ of the disk at the equilibrium remains equal to the initial Gaussian curvature, which is zero for an initially flat disk. Hence, the equilibrium shape should verify the condition $\det(\mathbf{k}) = 0$. Under the uniform curvature assumption, this implies a cylindrical equilibrium shape with a curvature

$$\mathbf{k}(c,\varphi) = c\,\mathbf{e}_S(\varphi)\otimes\mathbf{e}_S(\varphi), \tag{2.5}$$

where $\mathbf{e}_S(\varphi) = \cos\varphi\,\mathbf{e}_X + \sin\varphi\,\mathbf{e}_Y$ is the axis of curvature, as sketched in Figure 2.1, and the symbol $\otimes$ means the tensor product $(\boldsymbol{u}\otimes\boldsymbol{v})\cdot\boldsymbol{w} = (\boldsymbol{v}\cdot\boldsymbol{w})\,\boldsymbol{u}$. Here and henceforth, $\mathrm{X}(O,\mathbf{e}_X,\mathbf{e}_Y,\mathbf{e}_Z)$ will denote an ortho-normal fixed reference frame, with $\mathbf{e}_Z$ orthogonal to the initial disk mid-plane $\mathcal{D}$. For a perfectly isotropic disk, the elastic energy at the equilibrium is independent of the orientation φ, and reads as [33, 53]

$$\mathcal{E}(c,\varphi) = \frac{\pi R^2 E\,h^3}{12(1-\nu^2)}\left(\frac{c^2}{2} + (1+\nu)(\bar{c}^2 - c\,\bar{c})\right), \tag{2.6}$$

where h is the disk thickness and (E,ν) are its Young modulus and Poisson ratio. The stable equilibrium shapes of the disk are the minimizers of (2.6). For a given inelastic curvature $\bar{c}$, there is a continuous manifold of *neutrally stable* equilibria of curvature $c = (1+\nu)\bar{c}$, characterized by the same energy, independently of φ. Such a structure may be interesting for shape-control applications. Indeed, within the neutrally stable manifold, the shell can be deformed with vanishing actuation forces, while preserving a non-negligible stiffness for different deformation modes. This concept has been exploited in [33], by showing how to control a full precession of the axis of curvature of the disk with a weak multi-parameter piezoelectric actuation, see Figure 2.1. However, real structures are not perfectly isotropic. As shown in [33], slightly anisotropic disks are bistable and the actuation effort required to accomplish the full precession depends on a measure of their anisotropy.

The shape-change associated to the neutrally stable mode, *i.e.* the precession of the curvature axis, gives rise to a traveling wave where the velocity of each point of the disk is almost transversal to the mid-plane. This motion can be seen as the rotational analogue of the motion of the Taylor's swimming sheet (2.1). To study the interaction of this structural motion with a surrounding fluid, we need a complete description of its kinematics, which is given below.

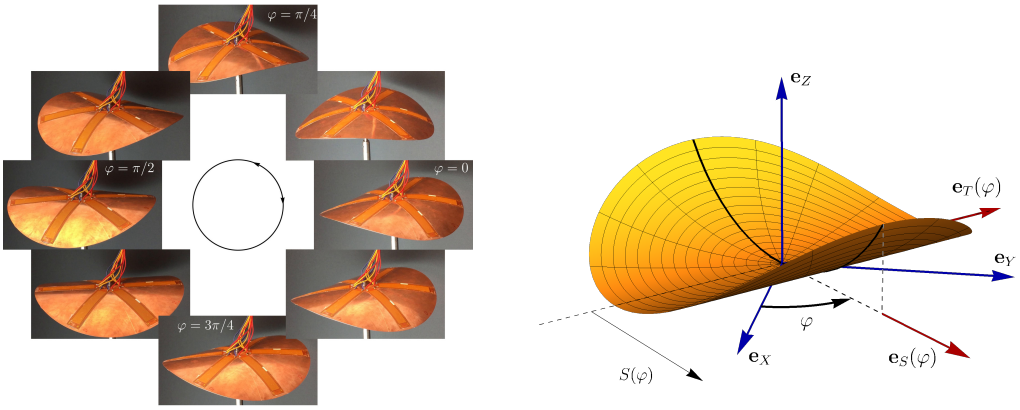

FIGURE 2.1: Shape-wave in the piezoelectric actuated neutrally stable shell. Left: Experiments from [33]. Kinematics and notation for the cylindrical shell used in this study, where φ gives the rotation of the curvature axis.

Let us denote by

$$\mathbf{X} = X\mathbf{e}_X + Y\mathbf{e}_Y \quad \text{such that} \quad X^2 + Y^2 \leq R^2, \tag{2.7}$$

the material points of the shell mid-plane in its flat reference configuration. For a curvature in the form (2.5), their current placement reads as

$$\mathbf{x} = \boldsymbol{\chi}(\mathbf{X}; c, \varphi) = \mathbf{X} + \left(\frac{\sin(c\,S(\mathbf{X},\varphi))}{c} - S(\mathbf{X},\varphi)\right)\mathbf{e}_S(\varphi) + \left(\frac{1-\cos(c\,S(\mathbf{X},\varphi))}{c}\right)\mathbf{e}_Z, \tag{2.8}$$

where $\mathbf{e}_S(\varphi)$ and $\mathbf{e}_T(\varphi)$ are a pair of rotating orthonormal axes corresponding to the directions of maximal and vanishing curvatures, respectively, and

$$\begin{aligned} S(\mathbf{X},\varphi) &= \mathbf{X}\cdot\mathbf{e}_S(\varphi) = X\cos\varphi + Y\sin\varphi, \\ T(\mathbf{X},\varphi) &= \mathbf{X}\cdot\mathbf{e}_T(\varphi) = -X\sin\varphi + Y\cos\varphi, \end{aligned} \tag{2.9}$$

are the coordinates of a material point $\mathbf{X}$ along these rotating axes.

For a generic motion $\mathbf{x} = \hat{\mathbf{x}}(\mathbf{X},t) = \boldsymbol{\chi}(\mathbf{X}; c(t), \varphi(t))$, the Lagrangian description of the velocity field is given by

$$\mathbf{U}_s(\mathbf{X},t) = \frac{\partial\,\hat{\mathbf{x}}(\mathbf{X},t)}{\partial t} = \left.\frac{\partial\boldsymbol{\chi}}{\partial c}\right|_t \dot{c}(t) + \left.\frac{\partial\boldsymbol{\chi}}{\partial\varphi}\right|_t \dot{\varphi}(t), \tag{2.10}$$

where

$$\frac{\partial\boldsymbol{\chi}}{\partial c} = \tfrac{c\,S\cos(c\,S)-\sin(c\,S)}{c^2}\,\mathbf{e}_S + \tfrac{c\,S\sin(c\,S)+\cos(c\,S)-1}{c^2}\,\mathbf{e}_Z = \tfrac{S^2}{2}\mathbf{e}_Z - \tfrac{c\,S^3}{3}\mathbf{e}_S + o(c), \tag{2.11}$$

$$\frac{\partial\boldsymbol{\chi}}{\partial\varphi} = T\,(\cos(c\,S)-1)\,\mathbf{e}_S + \left(\tfrac{\sin(c\,S)}{c} - S\right)\,\mathbf{e}_T + T\sin(c\,S)\,\mathbf{e}_Z = c\,S\,T\,\mathbf{e}_Z + o(c), \tag{2.12}$$

are the velocity modes associated to variations of the curvature amplitude and the curvature axis, respectively. Here $o(c)$ means a quantity vanishing faster than c as $c \to 0$. These velocity modes are sketched in Figure 2.2.

In the following, we will study the fluid problem forced by these velocity fields on the moving surface of the disk. For the sake of simplicity, we will focus on the case where the curvature varies as in (2.5) with a constant c, which corresponds to the motion of a perfectly isotropic disk. The case of weakly anisotropic structures would introduce only minor

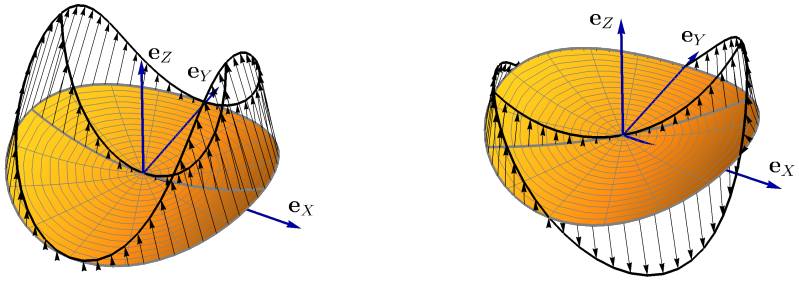

FIGURE 2.2: Velocity modes of the disk associated to variations of the curvature amplitude (left) and the curvature axis orientation (right), see Equations (2.10)-(2.12).

perturbations to this motion, that we will ignore.

In the following we will model the structure as a thick shell occupying in its reference configuration the three-dimensional domain $\Omega_s \equiv \mathcal{D} \times [-h/2, h/2]$. We will denote by Ω_s' its deformed configuration under the action of the mapping (2.8). We will extend the mapping χ defined on the midplane $\mathcal{D}$ to Ω_s by using a nonlinear shell kinematics.

2.4 Stokes flow and forces from the fluid to the structure

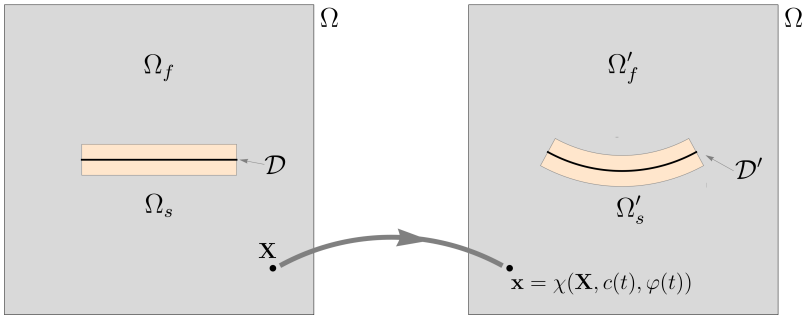

FIGURE 2.3: Structural (Ω_s, Ω_s') and fluid (Ω_f, Ω_f') domains in the reference and current configurations.

2.4.1 Problem formulation

We study the interaction between the shell and a viscous fluid. It is assumed that the Reynolds number is low enough ($\mathrm{Re} \ll 1$), and that the actuation is slow enough, such that the equations of motion for the fluid flow simplify to the (steady) Stokes equations. We neglect also the structural inertial effects and assume that the shell moves quasi-statically. As usual in fluid-structure problems, we adopt a Lagrangian description for the structure and a Eulerian description for the fluid. To correctly model the large displacement of the structure during the motion, we consider a geometrically nonlinear model.

We start by considering the case (2.4.1) where the shell deformation is assigned. In this framework we compute the forces exerted by the fluid on the shell for several actuation

conditions. This is a preliminary step to asses the potential behavior of the neutrally stable shell with embedded actuation as a *pump* or a *swimmer*. Hence, we generalize these results to the case (2.4.1) of a coupled fluid-structure interaction. For a perfectly neutrally stable shell, we are able to solve a minimal version of the coupled problem giving a relation between prescribed actuation forces and the resulting rotation speed.

Swimming problem at imposed precession speed

The computational domain for the fluid is taken as $\Omega'_f = \Omega \setminus \Omega'_s$, where Ω is a closed box containing the fluid, see Figure 2.3. The case of an unbounded flow is approached for $|\Omega| \to \infty$. Hence, to determine the fluid flow for a given structural motion, we solve the Stokes equations for the fluid velocity $\mathbf{u}$ and the pressure p imposing the structural velocity field on the boundary between the fluid and the structure for a given shape Ω'_s. They read as

$$\nabla p + \triangle \mathbf{u} = 0, \quad \nabla \cdot \mathbf{u} = 0 \quad \text{in}\, \Omega'_f, \tag{2.13}$$

with the boundary conditions

$$\mathbf{u} = \mathbf{u}_s(\mathbf{x}, t) \quad \text{on} \quad \partial\Omega'_f \cap \partial\Omega'_s, \tag{2.14}$$

$$\mathbf{u} = \mathbf{0} \quad \text{on} \quad \partial\Omega'_f \cap \partial\Omega. \tag{2.15}$$

The velocity field imposed on the boundary is the Eulerian version of the velocity field of the shell given in (2.10), superposed with a rigid motion:

$$\mathbf{u}_s(\mathbf{x}, t) = \dot{\mathbf{p}} + \dot{\boldsymbol{\alpha}} \times \mathbf{x} + \left.\frac{\partial \boldsymbol{\chi}}{\partial \varphi}\right|_{\mathbf{X}=\hat{\mathbf{x}}^{-1}(\mathbf{x},t)} \dot{\varphi}, \tag{2.16}$$

where we assumed $\dot{c} = 0$. Here, $\dot{\mathbf{p}}$ is the velocity of the shell corresponding to a rigid translation of the center of the disk and $\dot{\boldsymbol{\alpha}}$ the axial vector associated to a rigid rotation. For $c\,R < \pi$, the inverse map $\hat{\mathbf{x}}^{-1}(\mathbf{x}, t)$ can be calculated explicity. For $\varphi = 0$, it reads as

$$S = \operatorname{sign}(x)\,\frac{\arccos(1 - c\,z)}{c}, \quad T = y, \quad Z = 0,$$

and the Eulerian velocity field is

$$\left.\frac{\partial \boldsymbol{\chi}}{\partial \varphi}\right|_{\hat{\mathbf{x}}^{-1}(\mathbf{x},t)} = \operatorname{sign}(x)\left(\frac{\sqrt{(2-cz)cz} - \arccos(1-cz)}{c}\mathbf{e}_T + y\sqrt{(2-cz)cz}\,\mathbf{e}_Z\right) - c\,z y\,\mathbf{e}_S \tag{2.17}$$

The generic case $\varphi \neq 0$ can be obtained by a simple rotation of the and $x - y$ around the z-axis.

Given the solution of the Stokes problem for an imposed velocity field on the boundary, one can evaluate the force and moment resultant of the stresses that the fluid exerts on the structure as follows:

$$\boldsymbol{F} = \int_{\partial\Omega'_s} \boldsymbol{\sigma}\boldsymbol{n}\,\mathrm{d}s, \quad \boldsymbol{M} = \int_{\partial\Omega'_s} \boldsymbol{x} \times (\boldsymbol{\sigma}\,\boldsymbol{n})\,\mathrm{d}s, \tag{2.18}$$

where $\boldsymbol{\sigma} = p\,\mathbf{I} + 2\mu\,(\nabla\mathbf{u} + \nabla\mathbf{u}^T)$ is the Cauchy stress in the fluid, $\boldsymbol{n}$ is the unit normal pointing inside the fluid, $\mathrm{d}s$ denotes the surface measure and $\boldsymbol{x}$ is the position vector of the generic point in the current configuration. We take the center of disk $\boldsymbol{o}$ as the origin and as the pole for the moment $\boldsymbol{M}$. Because of the linearity of the Stokes equations and the linearity of the velocity field (2.16) imposed on the boundary with respect to $(\dot{\boldsymbol{p}}, \dot{\boldsymbol{\alpha}}, \dot{\varphi})$, also $(\boldsymbol{F}, \boldsymbol{M})$ will depend linearly on $(\dot{\boldsymbol{p}}, \dot{\boldsymbol{\alpha}}, \dot{\varphi})$. Hence we can write

$$\begin{pmatrix} \boldsymbol{F} \\ \boldsymbol{M} \end{pmatrix} = \boldsymbol{\mathcal{K}} \begin{pmatrix} \dot{\boldsymbol{p}} \\ \dot{\boldsymbol{\alpha}} \end{pmatrix} + \begin{pmatrix} \mathbf{k}_{\boldsymbol{p}\varphi} \\ \mathbf{k}_{\boldsymbol{\alpha}\varphi} \end{pmatrix} \dot{\varphi}, \qquad \boldsymbol{\mathcal{K}} := \begin{pmatrix} \mathbf{K}_{\boldsymbol{pp}} & \mathbf{K}_{\boldsymbol{p\alpha}} \\ \mathbf{K}_{\boldsymbol{p\alpha}}^T & \mathbf{K}_{\boldsymbol{\alpha\alpha}} \end{pmatrix}, \tag{2.19}$$

where $\boldsymbol{\mathcal{K}}$ is a symmetric negative-definite 6×6 matrix, because of the dissipative nature of the Stokes equations. The components of the columns of $\boldsymbol{\mathcal{K}}$ can be computed by solving 6 problems where only one of the components of $\dot{\boldsymbol{p}}$ or $\dot{\boldsymbol{\alpha}}$ is set to one, whilst the other are set to zero, and evaluating the corresponding force and moment resultants with (2.18). Similarly, the two 3×1 vectors $\mathbf{k}_{\boldsymbol{p}\varphi}$ and $\mathbf{k}_{\boldsymbol{\alpha}\varphi}$ are computed by solving the Stokes problem with $\dot{\boldsymbol{p}} = \dot{\boldsymbol{\alpha}} = \mathbf{0}$ and $\dot{\varphi} = 1$.

If the body is completely unconstrained, one can deduce the instantaneous free *swimming* velocity of the shell by imposing the quasi-static equilibrium conditions $\boldsymbol{F} = \mathbf{0}$, $\boldsymbol{M} = \mathbf{0}$, giving

$$\begin{pmatrix} \dot{\boldsymbol{p}} \\ \dot{\boldsymbol{\alpha}} \end{pmatrix} = -\boldsymbol{\mathcal{K}}^{-1} \begin{pmatrix} \mathbf{k}_{\boldsymbol{p}\varphi} \\ \mathbf{k}_{\boldsymbol{\alpha}\varphi} \end{pmatrix} \dot{\varphi}. \tag{2.20}$$

Assuming that the resultants on the body vanish corresponds to the *zero-thrust* velocity-generating function of the swimmer according to Lighthill [42]. Here, we study the relevant particular case where the shell rigid motion is the composition of a translation along the Z axis, controlled by $\dot{p}$, and a rotation around the same axis, controlled by $\dot{\alpha}$:

$$\dot{\boldsymbol{p}} = \dot{p}\, \boldsymbol{e}_Z, \qquad \dot{\boldsymbol{\alpha}} = \dot{\alpha}\, \boldsymbol{e}_Z. \tag{2.21}$$

The constraints are supposed to be perfect so that

$$\boldsymbol{F} \cdot \boldsymbol{e}_Z = 0, \qquad \boldsymbol{M} \cdot \boldsymbol{e}_Z = 0. \tag{2.22}$$

Using (2.19), (2.21) and (2.22) we obtain the equations for the constrained swimming as

$$\begin{pmatrix} k_{pp} & k_{p\alpha} \\ k_{p\alpha} & k_{\alpha\alpha} \end{pmatrix} \begin{pmatrix} \dot{p} \\ \dot{\alpha} \end{pmatrix} + \begin{pmatrix} k_{p\varphi} \\ k_{\alpha\varphi} \end{pmatrix} \dot{\varphi} = \begin{pmatrix} 0 \\ 0 \end{pmatrix}, \tag{2.23}$$

where

$$\begin{aligned} &k_{pp} = \mathbf{K}_{\boldsymbol{pp}} \boldsymbol{e}_Z \cdot \boldsymbol{e}_Z,\ k_{p\alpha} = \mathbf{K}_{\boldsymbol{p\alpha}} \boldsymbol{e}_Z \cdot \boldsymbol{e}_Z,\ k_{\alpha\alpha} = \mathbf{K}_{\boldsymbol{\alpha\alpha}} \boldsymbol{e}_Z \cdot \boldsymbol{e}_Z, \\ &k_{p\varphi} = \mathbf{k}_{\boldsymbol{p}\varphi} \cdot \boldsymbol{e}_Z,\ k_{\alpha\varphi} = \mathbf{k}_{\boldsymbol{\alpha}\varphi} \cdot \boldsymbol{e}_Z. \end{aligned} \tag{2.24}$$

The coupling coefficient of the resistance matrix $k_{p\alpha}$ relates the coupling between the rigid body translation and rotation of the structure, and is associated to the chirality of the structural shape [39]. From a dimensional analysis of the Stokes problem, we can deduce that the relevant coefficients can be written as follows

$$\begin{aligned} &k_{pp} = \mu R\, \hat{k}_{pp}(c, \varphi), \quad k_{p\alpha} = \mu R^2\, \hat{k}_{p\alpha}(c, \varphi), \quad k_{\alpha\alpha} = \mu R^3\, \hat{k}_{\alpha\alpha}(c, \varphi), \\ &k_{p\varphi} = \mu R^2\, \hat{k}_{p\varphi}(c, \varphi), \quad k_{\alpha\varphi} = \mu R^3\, \hat{k}_{\alpha\varphi}(c, \varphi), \end{aligned} \tag{2.25}$$

where $\hat{k}_{ij}$ are dimensionless scalar functions of the two shape parameters (c, φ) of the disk.

Swimming problem at imposed actuation forces

In Section 2.3 we presented an inextensible uniform-curvature structural model where the shell is described by two degrees-of-freedom: the curvature amplitude c and direction φ. For an almost neutrally stable shell the stiffness with respect to c is much higher than the one with respect to φ. As far as the inextensible shell model is pertinent, this stiffness ratio is vanishing independently of the shell thickness and Young modulus, see [33, 32]. Hence, we will study the coupled fluid-structure interaction under the further approximation that c is constant, and φ is the only structural degree-of-freedom left to describe the shell deformation.

In this framework the shell equilibrium equation is written as:

$$k_{p\varphi}\dot{p} + k_{\alpha\varphi}\dot{\alpha} + k_{\varphi\varphi}\dot{\varphi} + \frac{\partial \mathcal{E}(c,\varphi)}{\partial \varphi} = \bar{M}, \tag{2.26}$$

where $\bar{M}$ is a "twisting" moment modeling the effect of the embedded actuation, see [33], and $k_{\varphi\varphi}$ is the drag on the precession motion. This last coefficient can be computed by evaluating the tractions $\boldsymbol{\sigma n}$ for the Stokes problem with $\dot{\boldsymbol{p}} = \dot{\boldsymbol{\alpha}} = \mathbf{0}$ and $\dot{\varphi} = 1$ and projecting them on the velocity field (2.12), *i.e.*

$$k_{\varphi\varphi} = \int_{\partial\Omega_s'} \boldsymbol{\sigma n} \cdot \left.\frac{\partial \boldsymbol{\chi}}{\partial \varphi}\right|_{\hat{\mathbf{x}}^{-1}(\mathbf{x},t)} \mathrm{d}s. \tag{2.27}$$

The system obtained coupling (2.26) with (2.23), is a minimal version of the coupled fluid-structure problem at imposed actuation forces. Its solution allows us to determine the swimming speeds $\dot{p}$ and $\dot{\alpha}$ as a function of the applied moment $\bar{M}$. Remark that for a perfect neutrally-stable shell the elastic force $\partial\mathcal{E}(c,\varphi)/\partial\varphi$ vanishes, as the elastic energy $\mathcal{E}(c,\varphi)$ in (2.6) does not depend on the curvature direction φ. This fact will be exploited in Section 2.52.5.32.4.1.

Eq. (2.26) can be extended to account for further structural deformation modes (*e.g.* c), and inertial effects. However, this is out of the scope of the present work. The rest of the chapter is devoted to determine the coefficients in (2.25) and understand the key properties of the flow generated by the shell deformation. This will allows us to deduce the properties of the neutrally stable shells as swimmers, when driving the precession of the curvature axis with an embedded actuation.

2.4.2 Numerical methods

To obtain the forces and torques acting on the immersed shell, we follow the procedure reported below:

1. Generate the mesh for the holed fluid domain, $\Omega_f' = \Omega \setminus \Omega_s'$, where Ω_s' is the deformed configuration of the shell, see Figure 2.3-left.

2. Solve the outer Stokes problem on the deformed domain Ω_f' forced by the Eulerian velocity field (2.17) on the solid boundary. We use an adaptive finite element solver, based on a *a posteriori* error indicator.

3. Integrate, using (2.18), the stresses on the boundary $\partial\Omega_s' \cap \partial\Omega_f'$ to obtain the resultant force and moment exerted by the fluid on the shell.

The holed domain Ω_f' is discretized with tetrahedral elements using the mesh generator `gmsh` [26]. The Stokes problem is discretized and solved with standard finite elements techniques, implemented through the `FEniCS` [2] framework in `python` language. Using a solid domain with finite thickness allows us to represent different values of the stresses on the top and bottom shell surfaces without resorting to more involved numerical methods, such as Discontinuous Galërkin for the finite element approximation. We adopt a Taylor-Hood discretization of the displacement and pressure field on piecewise quadratic and piecewise linear Lagrange finite elements, respectively. Hence, we use iterative solvers and pre-conditioners provided by `PETSc` [7] to solve the underlying saddle problem on multiple processors. Iterative mesh adaptation is performed using a standard *a posteriori* error estimator for the Stokes problem [1].

The simulation is performed on a cylindrical box $\Omega = \{|Z| < H,\ (X^2 + Y^2) < L^2\}$. The size of the mesh and the size of the bounding box Ω are set to correctly reproduce the results of analytical solutions, in special cases in which such solutions are available. The influence

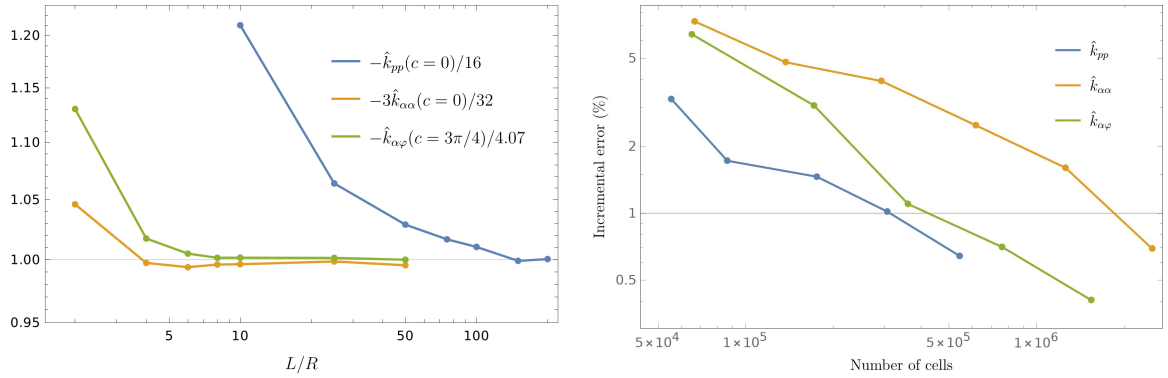

FIGURE 2.4: Numerical convergence of the hydrodynamic coefficients in (2.25) for a circular shell. Left: convergence with respect to the size L of the bounding box Ω; $\hat{k}_{pp}(c=0)$ and $k_{\alpha\alpha}(c=0)$ have been scaled with respect to their analytical values, whilst $\hat{k}_{\alpha\varphi}$ is scaled with respect to its numerical value when $L = 200R$. Right: convergence with respect to the number of FE cells for $L = 100\,R$.

of the size of the box is shown in Figure 2.4(left), which reports the drag coefficients $k_{pp}(c)$ and $k_{\alpha\alpha}(c)$ for the case of a flat disk $c = 0$. The numerical results converge to the analytic estimates for unbounded domains, respectively $\hat{k}_{pp}(c) = -16$ and $\hat{k}_{\alpha\alpha}(c) = -32/3$, see [38, 34]. The results of Figure 2.4 are obtained on a cylindrical box of eight $H = 100\,R$.

Figure 2.4(right) shows the percentage incremental error with respect to the total number of finite element cells. In the numerical simulations we use an adaptive mesh refinement based on the *a posteriori* error estimate suggested in [1]. Once the total error is summed over all the cells, only the ones having percentage error higher than a fixed fraction are refined using the method of [47]. This process is iterated until the evaluation of the forces and moments on the shell converge within a 0.5% variation with respect to the previous step.

Overall, considering the errors due the discretization and the finite size of the box, we can safely assume that the results produced in the rest of this analysis are accurate within an error margin of 1%.

2.5 Results

This section presents the results of the numerical simulations, performed to calculate the hydrodynamic coefficients in equation (2.23). Both the cases of swimming at imposed speed and at imposed actuation are considered. Hence, we rationalize the key features of the flow generated by the shell deformation. We will consider first the case of a circular shell. In the last subsection, we will present the result for the elliptic case.

2.5.1 Hydrodynamics coefficients for a circular shell

We solve numerically three Stokes problems defined by the following velocity fields on the fluid-structure interface:

1. Rigid body translation in the Z-axis direction: $\dot{p} = 1, \dot{\alpha} = \dot{\varphi} = 0$ to compute k_{pp} and $k_{p\alpha}$;
2. Rigid body rotation around the Z axis: $\dot{\alpha} = 1, \dot{p} = \dot{\varphi} = 0$ to compute $k_{\alpha\alpha}$;
3. Precession of the curvature axis: $\dot{\varphi} = 1, \dot{p} = \dot{\alpha} = 0$ to compute $k_{p\varphi}$, $k_{\alpha\varphi}$, and $k_{\varphi\varphi}$.

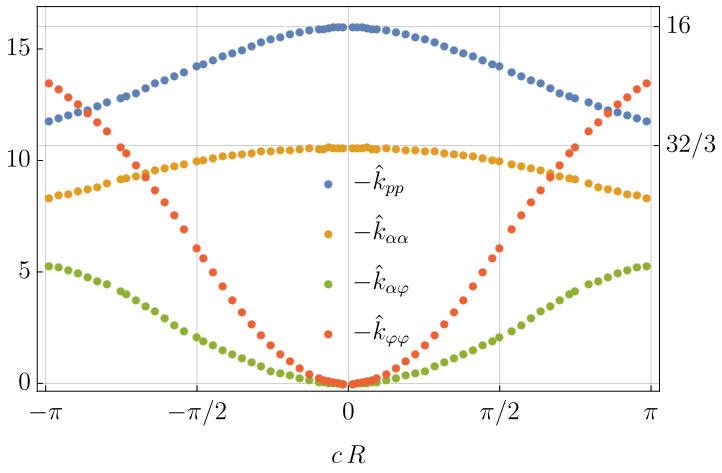

FIGURE 2.5: Coefficients of hydrodynamic resistance (2.25) as functions of the curvature c of a circular shell; $\hat{k}_{\varphi\varphi} = \mu R^3 k_{\varphi\varphi}$ is the dimensionless form of the drag (2.27).

The hydrodynamics coefficients (2.25) are computed by evaluating the associated force and moment resultants as in (2.18). These coefficients generally depend on the amplitude, c, and orientation, φ, of the shell curvature. In the case of a shell with a circular flat reference configuration, the symmetries of both the geometry and the loading imply the following simplifications:

- All the hydrodynamics coefficients are independent of φ. Without loss of generality one can set $\varphi = 0$. This is tantamount to choose the reference frame $\{O, \mathbf{e}_S, \mathbf{e}_T, \mathbf{e}_Z\}$ in (2.23).
- The coupling coefficient $k_{p\alpha}(c)$ vanishes for any value of c. This coefficient, being the torque resultant for an imposed rigid translation $\dot{p}\,\mathbf{e}_Z$, vanishes because the shell shape and the load are invariant under reflections with respect to $\mathbf{e}_T - \mathbf{e}_Z$ and $\mathbf{e}_S - \mathbf{e}_Z$ planes.
- The pumping force resultant $k_{p\varphi}(c)$ vanishes for any curvature c. This is due to the symmetries of the shell shape and the following properties of the velocity field (2.10): $U_S(S,T) = U_S(-S,T) = -U_S(S,-T)$, $U_T(S,T) = -U_T(-S,T) = U_T(S,-T)$, $U_Z(S,T) = -U_Z(-S,T) = -U_Z(S,-T)$, where $U_i = \partial_\varphi \boldsymbol{\chi} \cdot \boldsymbol{e}_i$.

Figure 2.5 reports the dimensionless version of the hydrodynamics coefficients $\hat{k}_{pp}(c)$, $\hat{k}_{\alpha\alpha}(c)$, $\hat{k}_{\alpha\varphi}(c)$, and $\hat{k}_{\varphi\varphi}(c)$ as a function of the dimensionless curvature $c\,R$. These plots are universal and independent of any physical parameter. The values reported here are computed on domains sufficiently large to neglect the effect of the bounding box Ω, $L = 200R$ in Figure 2.4.

The value of $k_{p\varphi}(c)$, not reported in Figure 2.5, turns out to be zero at the numerical accuracy, as anticipated above. A simple intuitive justification is the following: the precession of the axis of curvature causes (mainly) different sectors of the disc to move upwards or downwards in the direction that is perpendicular to the plane of the flat disc. Due to the geometry of the shell, the area of the sectors of the disc that move up or down is identical and therefore no net momentum flux is generated, and thus the integral of stresses over the shell should be zero. This is visually confirmed by inspecting the fluid-to-structure contact forces distribution reported in the top inset of Figure 2.6. They respect the same symmetries of the components U_i of the velocity field imposed on the boundary.

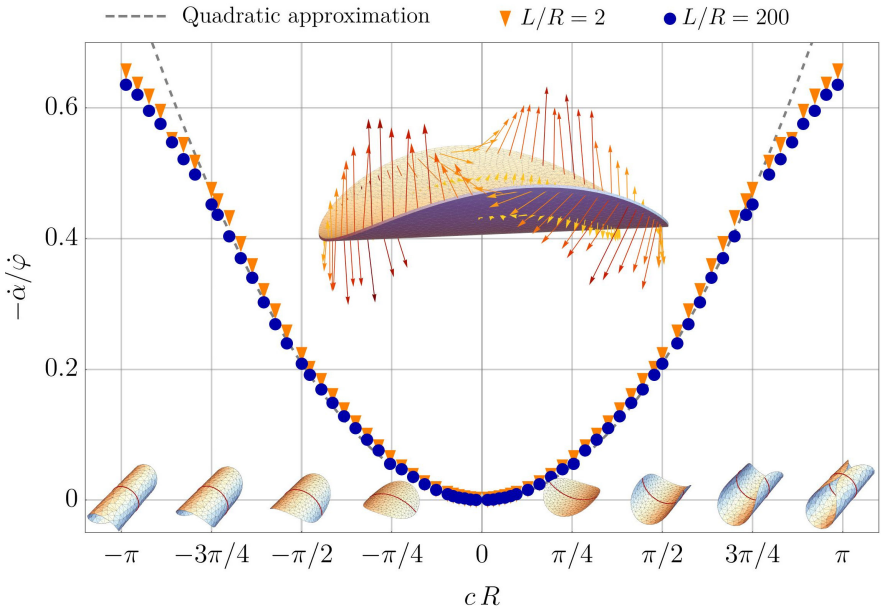

FIGURE 2.6: Rotational swimming velocity $\dot{\alpha}$ for a circular shell generated by the precession velocity of the curvature axis $\dot{\varphi}$; blue dots: numerical results for a cylindrical box of radius $L/R = 200$; orange triangles: numerical results for a box of radius $L/R = 2$; dashed line: quadratic approximation for moderate curvature (2.30). Inset: Fluid-to-structure net contact forces distribution for $cR = 0.8$ as found by extracting from the numerical simulation the jump of the contact force between the upper $(+)$ and lower $(-)$ shell surfaces, $[\![\boldsymbol{\sigma}\boldsymbol{n}]\!] = \boldsymbol{\sigma}^{+}\boldsymbol{n}^{+} - \boldsymbol{\sigma}^{-}\boldsymbol{n}^{-}$.

2.5.2 Swimming problem at imposed precession speed $\dot{\varphi}$

Applying in (2.23) the simplifications due to the symmetry reported above, one can readily solve the swimming problem at imposed precession speed $\dot{\varphi}$ to get:

$$\dot{p}(c) = -\frac{k_{p\varphi}(c)}{k_{pp}(c)}\,\dot{\varphi} = 0, \qquad \dot{\alpha}(c) = -\frac{k_{\alpha\varphi}(c)}{k_{\alpha\alpha}(c)}\,\dot{\varphi}. \tag{2.28}$$

The *swimming* motion of the shell is a pure rotation around the Z-axis with a speed $\dot{\alpha}$ driven by a non-vanishing torque resultant $k_{\alpha\varphi}$ in (2.28).

Using the numerical values reported in Figure 2.5, Figure 2.6 summarizes our findings plotting the ratio between the swimming rotation speed $\dot{\alpha}(c)$ and the driving speed $\dot{\varphi}$ of the deformation wave as function of the dimensionless shell curvature cR. The rotational swimming motion driven by the precession of the shell curvature axis is the rotational analogue of the translation swimming motion of the Taylor's sheet [59]. The deformation of the shell can be regarded as a circular traveling wave of transversal displacement.

For a Taylor's sheet, the ratio between the translational swimming velocity U and the phase speed v of the deformation wave is (2.4):

$$\frac{U}{v} = -\frac{1}{2}(b\,k)^2, \quad \text{for} \quad |b\,k| \ll 1. \tag{2.29}$$

In our case, the wave number is fixed to $k = 2/R$, while, in the shallow shell approximation, the wave amplitude scales as $b \propto c\,R^2$. Substituting these relations in (2.29), as $b\,k \sim c\,R$, the rotational velocity is expected in the form $\dot{\alpha}/\dot{\varphi} \propto -(c\,R)^2$.

This is confirmed numerically in Figure 2.6, which shows that the swimming angular speed produced for a symmetric range of curvatures. The numerical data may be fitted by the following quadratic approximation in $c\,R$:

$$\frac{\dot\alpha(c)}{\dot\varphi} \simeq -\frac{1}{12.0}(c\,R)^2 \quad \text{for} \quad |c\,R| \lesssim \frac{3\pi}{4}. \tag{2.30}$$

This approximation is the analogue of the Taylor formula (2.29) for a flat sheet. Our numerical results show that the quadratic approximation is accurate even for $c\,R \simeq 1$. Here, the dimensionless parameter $c\,R$ measures the central angle of the cylindrical configuration of the shell. As show in the lower insets of Figure 2.6 for $c\,R = \pi$, its cross-section with the plane $T = 0$ is a circle. Interestingly, the efficiency of the shell as a rotational swimmer is very robust both with respect to the curvature amplitude and the radius of the confining box. The numerical results for a cylindrical bounding box of radius $L/R = 2$ and $L/R = 200$ are almost indistinguishable and close to the quadratic approximation even for $|c\,R| \to \pi$. The height of the cylinder is fixed here to $H/R = 100$.

2.5.3 Swimming problem at imposed actuation

The swimming problem at imposed actuation consists in solving the system (2.23) and (2.26) for $\dot p$, $\dot\alpha$, and $\dot\varphi$ as functions of $\bar M$.

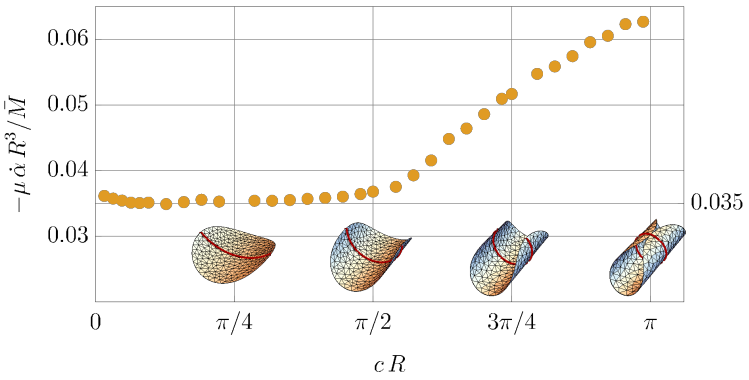

FIGURE 2.7: Swimming rotation speed $\dot\alpha$ for applied moment $\bar M$ as a function of the dimensionless curvature $c\,R$ of a circular shell. The dots are computed from $(2.32)_2$ for the data in Figure 2.5. The value 0.035 has been estimated by a quadratic approximation of the hydrodynamic coefficients near $c = 0$.

In general this is a system of ordinary differential equations in time, but, for a perfectly neutrally-stable shell, the elastic force $\partial\mathcal{E}(c,\varphi)/\partial\varphi$ in (2.26) vanishes. Hence, the system reduces to a linear algebraic system in the velocities $(\dot p, \dot\alpha, \dot\varphi)$. Moreover, for the case of circular shells, the symmetries imply $k_{p\alpha} = k_{p\varphi} = 0$ for any value of the curvature c, see Section 2.52.5.1; the system simplifies to:

$$\begin{pmatrix} k_{pp}(c) & 0 & 0 \\ 0 & k_{\alpha\alpha}(c) & k_{\alpha\varphi}(c) \\ 0 & k_{\alpha\varphi}(c) & k_{\varphi\varphi}(c) \end{pmatrix} \begin{pmatrix} \dot p \\ \dot\alpha \\ \dot\varphi \end{pmatrix} = \begin{pmatrix} 0 \\ 0 \\ \bar M \end{pmatrix}, \tag{2.31}$$

which can readily solved to get

$$\dot p = 0, \qquad \dot\alpha = \frac{k_{\alpha\varphi}(c)\,\bar M}{k_{\alpha\varphi}^2(c) - k_{\varphi\varphi}k_{\alpha\alpha}(c)}, \qquad \dot\varphi = \frac{-k_{\alpha\alpha}(c)\bar M}{k_{\alpha\varphi}^2(c) - k_{\varphi\varphi}(c)k_{\alpha\alpha}(c)}. \tag{2.32}$$

The most interesting result is the "swimming" rotation speed $\dot{\alpha}$ generated by the actuation moment $\bar{M}$, which is plotted in Figure 2.7 using the numerical values of the hydrodynamic coefficients reported in Figure 2.5. We observe two regimes: for $c\,R \leq \pi/2$ the ratio $\dot{\alpha}/\bar{M}$ is almost independent of the curvature whilst for $c\,R > \pi/2$ the swimming efficiency grows almost linearly with the curvature. We do not have a clear explanation for this result; however, we can observe that after the curvature value $c\,R = \pi/2$ the shell starts curling up and tends to a closed cylindrical shape, see the insets in Figure 2.7. It is therefore reasonable to expect a qualitative difference in the dependence of the hydrodynamic coefficients on the curvature in the two regimes. Indeed, $c\,R = \pi/2$ corresponds to an inflection point for the hydrodynamic coefficients in Figure 2.5.

2.5.4 Structure of the fluid flow (circular case)

We now analyze the structure of the fluid flow driven by the precession, $\dot{\varphi} = 1$, of the curvature axis when the shell is clamped ($\dot{\alpha} = 0$, $\dot{p} = 0$) and, hence, acts as a *pump*. Figure 2.8 reports the stream lines (left) and the pressure distribution (right) in a small region around the shell for the loading case (iii) and $c = 0.8/R$. The near-field flow (close to the structure) shows four vortices emanating from the shell in the directions of maximal (S) and vanishing (T) curvatures. The two vortices in the direction of maximal curvature bend upwards following the curvature of the shell. At distance $Z \sim 10R$, they coalesce into a single vortex on the top of the shell, giving the far-field structure of the flow for $Z \to +\infty$.

The key properties of the flow can be rationalized in terms of fundamental solutions of the Stokes equations to point forces. To this end, we project the fluid-to-structure net contact forces, represented in the inset of Figure 2.6, on the Gauss frame associated to the shell mid-surface $\boldsymbol{a}_r, \boldsymbol{a}_\theta, \boldsymbol{n}$. Here, $\boldsymbol{a}_r$ and $\boldsymbol{a}_\theta$ are the radial and circumferential tangent unit vectors, respectively, and $\boldsymbol{n} = \boldsymbol{a}_r \times \boldsymbol{a}_\theta$ is the normal. The components of the net contact force field $F_r = [\![\boldsymbol{\sigma n}]\!] \cdot \boldsymbol{a}_r$, $F_\theta = [\![\boldsymbol{\sigma n}]\!] \cdot \boldsymbol{a}_\theta$, and $F_n = [\![\boldsymbol{\sigma n}]\!] \cdot \boldsymbol{n}$ are plotted in Figure 2.9. The far-field effect of this force field on the fluid flow can be reproduced by four equivalent point forces, one for each quadrant of the shell. To this aim, within the shallow shell approximation, we fix a cylindrical coordinate system $(O, \boldsymbol{e}_r(\theta), \boldsymbol{e}_\theta(\theta), \boldsymbol{e}_Z)$ in the $X - Y$ plane. The equivalent four forces, respecting the same symmetries of the net contact force distribution, are ($i = 1, \dots, 4$)

$$\boldsymbol{F}_i = F_\theta \boldsymbol{e}_\theta(\theta_i) + \text{sign}(\tan\theta_i)(F_r \boldsymbol{e}_r(\theta_i) + F_Z \boldsymbol{e}_Z), \qquad i = 1, \dots 4 \tag{2.33}$$

applied at points $\boldsymbol{x}_i = d\,\boldsymbol{e}_r(\theta_i)$ with $\theta_i = (2i-1)\pi/4$ (points on the bisector lines at distance $d \sim R$ from the center, see the black arrows in Figure 2.9). The velocity field generated by a point unit force applied at the point $\boldsymbol{y}$ in a direction $\boldsymbol{e}$ is:

$$\boldsymbol{G}(\boldsymbol{x}, \boldsymbol{y}, \boldsymbol{e}) = \frac{\boldsymbol{e}}{\|\boldsymbol{x} - \boldsymbol{y}\|} + \frac{\boldsymbol{e} \cdot (\boldsymbol{x} - \boldsymbol{y})}{\|\boldsymbol{x} - \boldsymbol{y}\|^3}(\boldsymbol{x} - \boldsymbol{y}). \tag{2.34}$$

usually called *Stokeslet*. Hence, the far-field approximation velocity field generated by the pattern of the four point forces is calculated by superposing the corresponding *Stokeslet* and taking the series expansion for $d \ll 1$. We get

$$\boldsymbol{v}(\boldsymbol{x}) = \sum_{i=1}^{4} \boldsymbol{G}(\boldsymbol{x}, \boldsymbol{x}_i, \boldsymbol{F}_i) = d\,(F_\theta \boldsymbol{R}(\boldsymbol{x}) + F_r\,\boldsymbol{S}(\boldsymbol{x})) + F_Z\,\boldsymbol{Q}(\boldsymbol{x})\,\frac{d^2}{2} + o(d^3), \tag{2.35}$$

with

$$\boldsymbol{R}(\boldsymbol{x}) = \frac{\boldsymbol{e}_Z \times \hat{\boldsymbol{x}}}{\|\boldsymbol{x}\|^2}, \qquad \boldsymbol{S}(\boldsymbol{x}) = \frac{\sin(2\theta)}{2}\frac{\hat{\boldsymbol{x}}}{\|\boldsymbol{x}\|^2}, \qquad \boldsymbol{Q}(\boldsymbol{x}) = \frac{q(\hat{\boldsymbol{x}})}{\|\boldsymbol{x}\|^3}, \tag{2.36}$$

where $\hat{\boldsymbol{x}} = \boldsymbol{x}/\|\boldsymbol{x}\|$. As the four Stokeslets are distributed on a surface and, due to the symmetry of the problem, the lowest-order contribution in the resulting singular velocity field

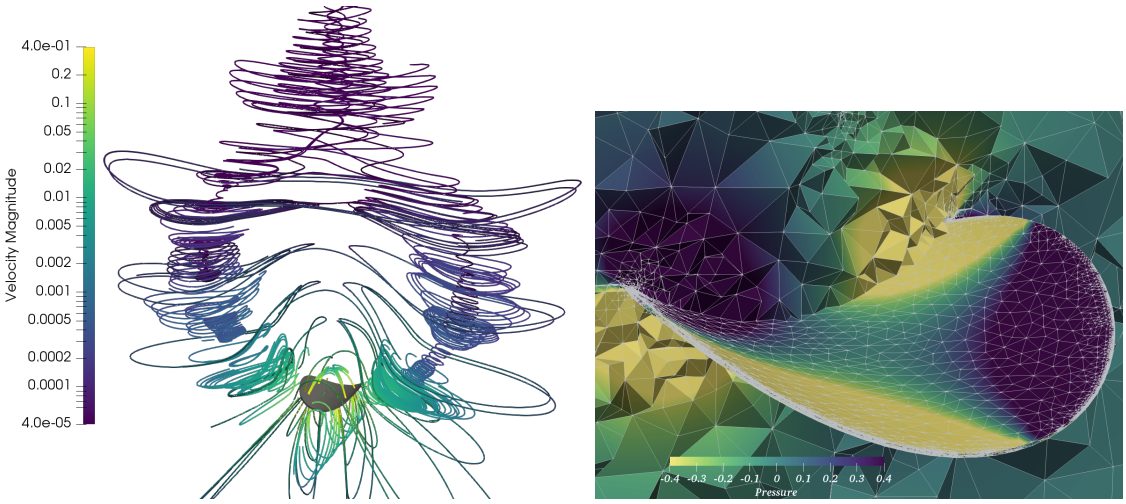

FIGURE 2.8: Structure of the flow generated by the precession of the shell curvature axis with $c = 0.8$ and $R = 1$ for the loading case (iii). Left: Streamlines with the shell in grey. Right: Illustration of the mesh after adaptive refinement used for the 3d finite element calculations; the colors represent the pressure field.

(2.35) is a dipole decaying as $1/\|\boldsymbol{x}\|^2$. The Stokeslet term, decaying as $1/\|\boldsymbol{x}\|$ is instead vanishing. The dipole can be decomposed in a skew-symmetric part, the *rotlet* $\boldsymbol{R}$, and a symmetric part, the *stresslet* $\boldsymbol{S}$. The higher order term in the expansion (2.36) is a *quadrupole* $\boldsymbol{Q}$, see [34], decaying as $1/\|\boldsymbol{x}\|^3$. The explicit analytical expression of $q(\hat{\boldsymbol{x}})$ is available in classical textbooks [48]; we report in Figure 2.10 the corresponding streamlines instead. The field close to the shell surface is dominated by the quadrupole term with its four vortices. Vice-versa the far-field is dominated by the rotlet and stresslet terms. The streamlines resulting by the superposition of $\boldsymbol{R}$, $\boldsymbol{S}$ and $\boldsymbol{Q}$ are sketched in Figure 2.10, which qualitatively reproduces the main structures observed in the direct numerical simulation of Figure 2.8.

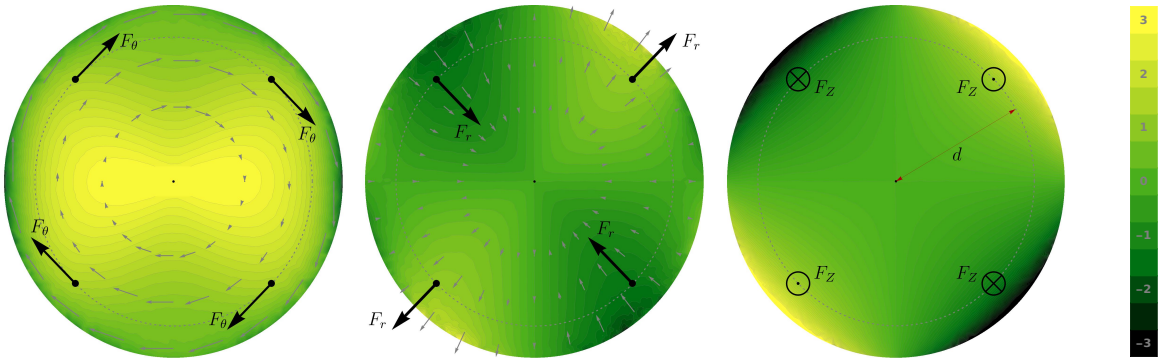

FIGURE 2.9: Decomposition of the net contact force field (see the inset of Figure 2.6) in the circumferential component F_θ (left), the radial component F_r (center), and the pressure p (right). The black arrows are a system of four forces reproducing the same symmetry, and used in the far-field approximation (2.35).

2.5.5 The case of elliptic shells

In the circular case, the force resultant $k_{p\varphi}$ and the coupling coefficient $k_{p\alpha}$ vanish because of the symmetries. For a shell with an elliptical shape in its flat reference configuration, these coefficients are non-null. Moreover, all the coefficients in (2.23)-(2.25) depend on the

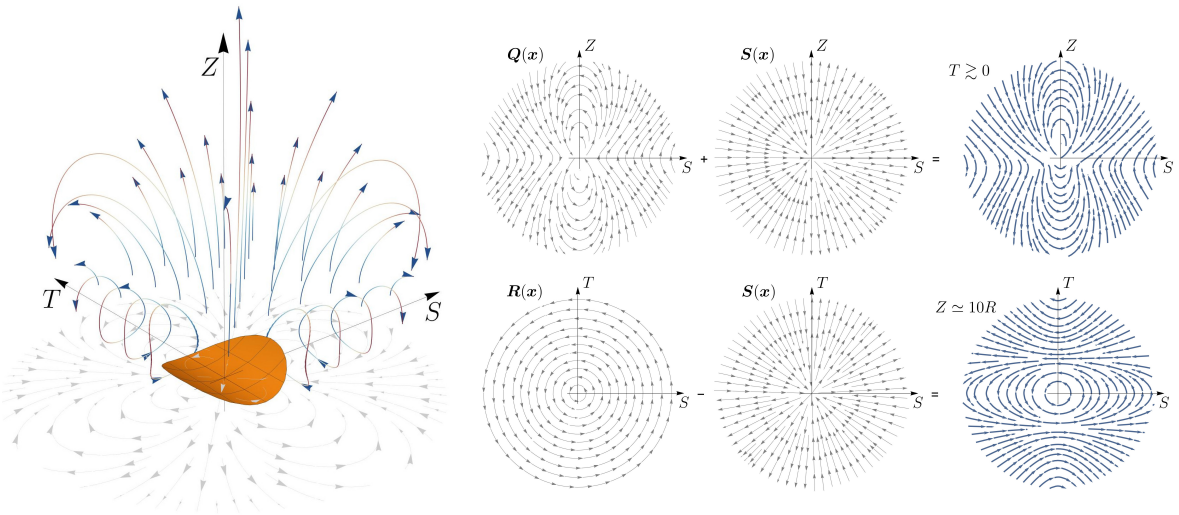

FIGURE 2.10: Qualitative representation of the velocity field by singular solutions, see (2.35) and (2.36). Left: Streamlines of the quadrupole term $\boldsymbol{Q}$. Right: effects of the superposition of a quadrupole $\boldsymbol{Q}$ and a stresslet $\boldsymbol{S}$ in the plane $0 < T \ll 1$ (top) and of a rotlet $\boldsymbol{R}$ and a stresslet in the plane $Z \gg 1$ (bottom).

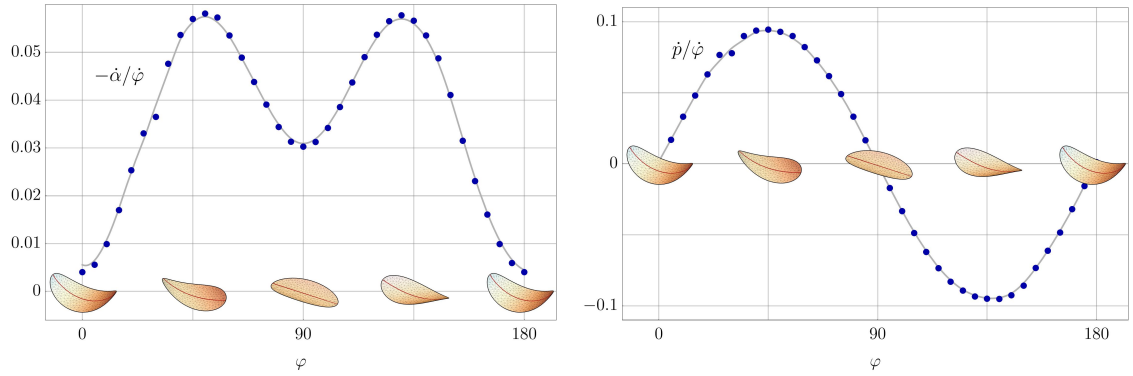

FIGURE 2.11: Rotational ($\dot{\alpha}$) and translational ($\dot{p}$) velocities of an elliptic shell during the precession of its curvature axis (φ): results of a numerical simulation on a shell with semi-axes $R_X = 1$ and $R_Y = 1/2$, and curvature $c = 0.8/R_X$ computed using (2.23).

direction of maximal curvature φ. We report here the results obtained from the numerical simulation for a shell with semi-axes $R_X = 1$ (X direction) and $R_Y = 1/2$ (Y direction) and a curvature amplitude $c = 0.8/R_X$. Figure 2.11 plots the translational and rotational swimming velocities, $\dot{p}$ and $\dot{\alpha}$ as a function of the orientation of the curvature axis $\varphi \in (0, 2\pi)$, during its full precession. In this case, the translation swimming velocity is non-null and the rotational velocity varies during a period. However, the translation velocity (and displacement) is periodic, the shell moves back and forth on the Z-axis while rotating, but there is not a net translation after an integer number of periods. This can be seen as a direct consequence of the *scallop theorem* [49]. The video attached in the Supplementary Material helps to visualize this case.

2.6 Conclusions

It has been shown how the problem of a complex active structure exhibiting spontaneous curvature, moving within a (viscous) fluid, can be connected to classic examples of locomotion

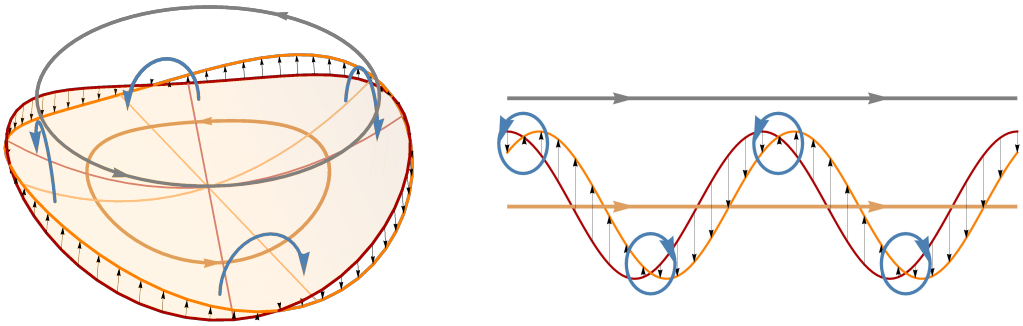

FIGURE 2.12: Schematics of the basic mechanism of the rotational Taylor sheet, extending to the rotational shape wave of neutrally stable disk (left) the physical interpretation of [39] of the classical Taylor sheet with a translation shape wave. We report in red and orange the configuration of the structure at time T and $T + \Delta T$, with small ΔT, in a reference frame moving with the structure, where the black arrows indicate the velocity field of the structure and the blue arrows schematically represent the vorticity in the fluid. The gray arrows indicate the flow velocity at infinity, which is opposite to the swimming velocity in a fixed reference frame.

at low *Reynolds* numbers, in particular the work of Taylor [59]. The main issue in this setting is that linearity of Stokes equations results in the celebrated observation due to Purcell [49], usually referred to as the *scallop theorem:* a reciprocal motion (precisely, a shape-change sequence that is identical after time-reversal [39]) does not generate net motion on average. The scallop theorem implies that the swimming strategy has to satisfy some geometrical requirements in order to be effective. The precession of the curvature axis can be seen as a traveling (circular) wave of transversal displacement, similar to the case of the Taylor sheet. This analogy is summarized in Figure 2.12, which transposes to our case the kinematical interpretation of the Taylor's sheet effect given in [39]. The shape wave generates a system of counter-rotating vortices resulting in a net rotational motion of the swimmer. In the circular case, the symmetry of the problem prevents net translations. Interestingly, if instead the shape of the shell in the flat configuration is elliptic, a net force, and thus instantaneous displacement is generated. The force however is periodic and therefore the displacement is zero over a period.

Directions of further research might involve relaxing the hypothesis of very low *Reynolds* numbers, in order to consider cases when inertia is no longer negligible. This might include exploiting instabilities of thin structures, as bistable clamped tails [9], or pulsatile motions [22]. In this framework, the elastic response of the structure would play a crucial role and can be accounted for by using reduced models or finite-element shell models [31], coupled with a Navier-Stokes solver.

Other interesting applications include the possibility of using the neutrally stable shells studied here to harvest energy from the fluid flow [43, 10] or as deformable mixing devices.

Chapter 3

Asymptotic approach to a rotational Taylor swimming sheet

3.1 Introduction

The swimming problem at low Reynolds numbers has stimulated a great amount of research, resulting in a huge body of literature (see [39]), and it was originally proposed by G.I. Taylor ([59]) in a celebrated paper. Taylor considered the problem of the self-propulsion of a two-dimensional infinite sheet immersed in a viscous fluid. The sheet undergoes periodic deformation due to the propagation of waves of transversal displacement. Assuming these waves have small amplitude Taylor was able, with a perturbative expansion of the boundary conditions, to obtain the corresponding solution of the Stokes problem, and therefore determine the motion of the body. The model is one of the simplest examples of self-propulsion (no external forces are acting on the body) in viscous flow that can be treated analytically. In order to give more details about Taylor's solution, we consider an unbounded 3D fluid domain where the undeformed sheet coincides with the plane $y = 0$. A travelling wave propagating in the x direction will then casue a periodic vertical displacement:

$$y_0 = b\sin(k(x - vt)), \tag{3.1}$$

where b is the amplitude of the wave, and k, v, are the wave number and wave phase speed, respectively. Choosing, as is customary in this kind of problems, a reference frame moving with the sheet, the boundary condition on the velocity of the fluid at the surface of the body will be [39]:

$$\mathbf{u}(x, y_0(x,t)) = -bkv\cos(k(x - vt))\mathbf{e}_y, \tag{3.2}$$

while the other boundary condition is that infinitely far from the sheet the flow be uniform and steady:

$$\lim_{y\to\infty} \mathbf{u} = -U\mathbf{e}_x. \tag{3.3}$$

It should be noted that U, which is the swimming speed, is not known a priori, therefore the value at the boundary will be obtained as a result of the solution of the Stokes flow. Indeed, Taylor showed that by expanding the boundary condition (3.2) in powers of the dimensionless parameter bk, the problem can be solved for each power, approximating U with increasing accuracy. Considering terms of the solution up to second order in bk, the swimming velocity in (3.3) is

$$U = -\frac{1}{2}v(bk)^2. \tag{3.4}$$

The first important result following from (3.4) is that, when deformations are small, travelling waves of bending cause translation in the direction opposite to their propagation. This solution defines a paradigm for swimming at low Reynolds that inspired many applications, as for example in [24], where the mechanism described by Taylor is applied to micron-sized artificial

systems. More recently, strong interest was oriented towards active structures and, notably among these, active shells. In [33], a thin circular shell with spontaneous self-curvature is studied. In particular, the shell is neutrally stable: that is, the curvature axis can be oriented arbitrarily by actuation with very weak (ideally vanishing) forces. Therefore, with proper actuation, one can obtain a particular pattern of periodic deformation, namely the precession of the axis of curvature on the plane of the disc in the flat configuration (see [33] for details). A representation of this periodic deformation, that can be seen as a wave of curvature, is given in figure (3.1), together with a comparison with what happens in the case of Taylor. Therefore, this particular patterns of deformation lead to whether a circular disc, deformed in this way, can be seen as a circular analogue of Taylor's sheet, and what kind of motion patterns can be achieved. In [17], the idealized problem of a disc undergoing such deformations in Stokes flow was addressed numerically. The numerical results pointed at a similarity with the case Taylor in that rotations were generated, in the opposite direction with respect to that of precession of the axis of curvature. On the other hand, no net displacement could be achieved. The results for a wide range of values of curvature were considered (up to the disc sides almost touching) and a relation between precession and induced rotation was obtained, by numerical fitting. The general behaviour of the solution can indeed be estimated by dimensional arguments, both in the case of [17] and that of Taylor, and leads to the same prediction: a quadratic dependence of the swimming velocity on the dimensionless parameter of wave amplitude, which in the case of the disc is given by the (non-dimensionalized) curvature. One important result of the relation obtained by Taylor (3.4) is that the coefficient of this relation is obtained analytically. This completely determines the relation between the actuation and its intensity, namely the wave phase speed v and the dimensionless amplitude bk, and the resulting swimming speed U. In [17], the equivalent swimming action was identified with the rotation rate, $\dot{\alpha}$, and the actuation with the rate of rotation of the axis of curvature (the precession) $\dot{\varphi}$ and the curvature cR (equivalent to the amplitude of the wave), where the curvature c is non-dimensionalized with the radius of the flat disc R, which can be taken with unitary value due to the linearity of the Stokes equations. A relation similar to that of Taylor was then obtained numerically. Here, we proceed with an asymptotic approach, aiming to reproduce Taylor's procedure, in order to confirm analytically some results from [17], namely the quadratic dependence of induced rotation rate on curvature, behaviour of rotations and translations resulting from the precession motion, and value of coefficient. This coefficient is the final result of our analytical argument and determines our equivalent relation for the rotational Taylor sheet, as will be proved:

$$\dot{\alpha} = \frac{1}{10} c^2 \dot{\varphi}. \tag{3.5}$$

These results allow us to back up the numerical results with an analytical confirmation, as well as to further support the analogy of this particular shell as a real-life example of rotational Taylor's sheet.

3.2 Statement of the problem

We consider, as in [17], a circular disc of unitary radius in an unbounded domain filled by a viscous fluid. The reference configuration for the shell is the flat one, which coincides with a circular disk with centre at the origin in the plane $Z = 0$. The deformation is due to the spontaneous curvature of the object, and to the precession of the axis of curvature [33]. In a plane perpendicular to this axis, intersecting the disc, the shape of the body is that of a circular arc. Therefore, the (time-dependent) displacement field for small values of curvature, considering only displacements orthogonal to the plane $Z = 0$ (as the other components are

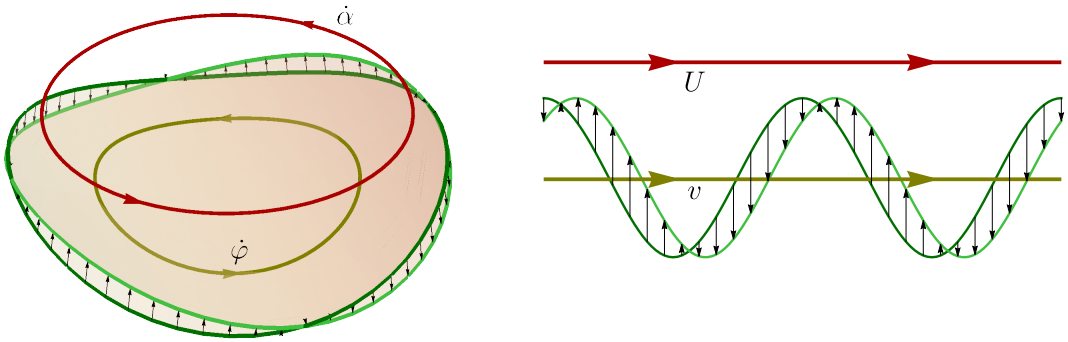

FIGURE 3.1: Left: Representation of the periodic deformation of the shell under actuation, due to change in orientation of the axis of curvature (described by the rate $\dot{\varphi}$). Right: comparison with the periodic deformation of the Taylor swimming sheet, due to the propagation of a wave of bending.

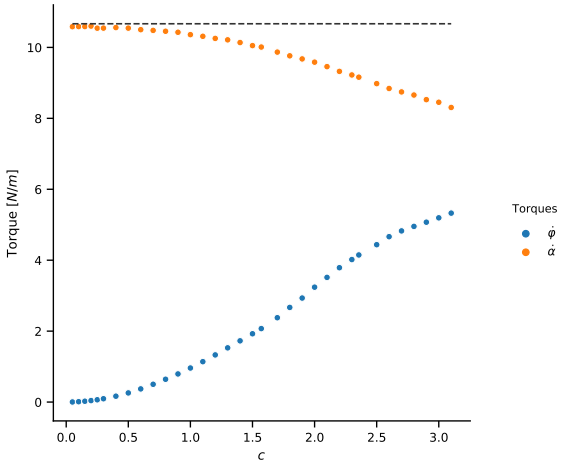

FIGURE 3.2: Torques induced on a disc for imposed unitary precession of the curvature axis, $\dot{\varphi} = 1$, or unitary rotation rate, $\dot{\alpha} = 1$, respectively, from [17]. Dashed line: torque acting on the fluid for unitary rotation rate, known to be 32/3.

of smaller order of magnitude in the approximation of small curvatures), is:

$$w = \frac{1 - \cos(cs)}{c} \simeq \frac{cs^2}{2}, \tag{3.6}$$

where the arc length is $s = X\cos\varphi + Y\sin\varphi$, with φ being the angle between the axis of curvature and the X axis. An example of this deformation is given in figures 3.3 and 3.4. Introducing cylindrical coordinates

$$w \simeq \frac{c(X\cos\varphi + Y\sin\varphi)^2}{2} = c\frac{(r\cos\theta\cos\varphi + r\sin\theta\sin\varphi)^2}{2} = \frac{cr^2}{2}\cos^2(\theta - \varphi). \tag{3.7}$$

Differentiating this displacement in time now yields the velocity perpendicular to the plane of the flat configuration:

$$v = \frac{cr^2}{2} \cdot 2\cos(\theta - \varphi)\sin(\theta - \varphi)\dot{\varphi} = \frac{cr^2}{2}\sin(2\theta - 2\varphi)\dot{\varphi}. \tag{3.8}$$

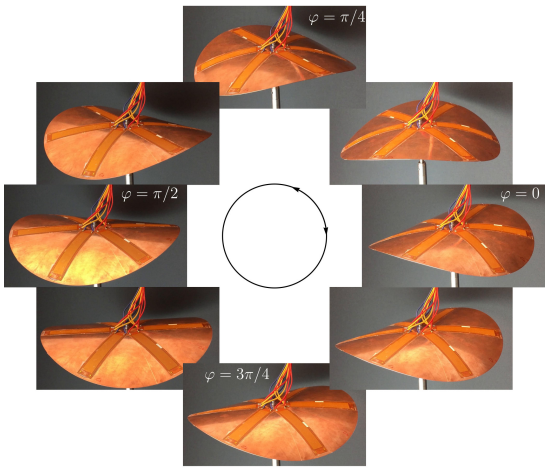

FIGURE 3.3: Precession deformation of the shell over time, from [33].

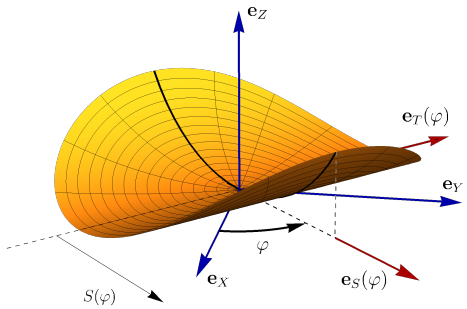

FIGURE 3.4: References for the deformation of the shell, from [17].

In the case of circular shell, the value of φ can be taken arbitrarily due to rotational invariance, thus we fix $\varphi = 0$ and the fields simplify to

$$w = \frac{cr^2}{2}\cos^2\theta, \tag{3.9}$$

$$v = \frac{cr^2}{2}\sin 2\theta \cdot \dot{\varphi}. \tag{3.10}$$

From now on we fix $\dot{\varphi} = 1$, for simplicity. The flow problem can now be stated: solve the Stokes equations

$$\nabla p + \triangle \mathbf{u} = 0, \quad \nabla \cdot \mathbf{u} = 0, \tag{3.11}$$

with the following boundary conditions

$$\mathbf{u}\left(r, \theta, z = \frac{cr^2}{2}\cos^2\theta\right) = \frac{cr^2}{2}\sin 2\theta \cdot \mathbf{e}_z \qquad \text{for } r \leq 1, \tag{3.12}$$

$$\mathbf{u} = \mathbf{0} \qquad \text{for } r \to \infty. \tag{3.13}$$

Here, as in Taylor's case, the no-slip condition on the velocity at the surface of the shell results in a boundary condition on a moving, and deformed, boundary. Following Taylor's approach, we expand the solution in powers of the non-dimensional parameter (cR), where $R = 1$ is the radius of the disc:

$$u_z = (cR)u_z^{(1)} + (cR)^2 u_z^{(2)} + (cR)^3 u_z^{(3)} + \ldots, \tag{3.14}$$

$$u_\theta = (cR)u_\theta^{(1)} + (cR)^2 u_\theta^{(2)} + (cR)^3 u_\theta^{(3)} + \ldots, \tag{3.15}$$

$$u_r = (cR)u_r^{(1)} + (cR)^2 u_r^{(2)} + (cR)^3 u_r^{(3)} + \ldots. \tag{3.16}$$

Moreover, we expand the boundary condition (3.12) in c (the expansion is done for small values of the curvature, and therefore equivalently around $Z = 0$):

$$u_z = u_z(r,\theta,0) + \left.\frac{\partial u_z(r,\theta,z)}{\partial z}\right|_{z=0} \cdot \frac{cr^2}{2}\cos^2\theta + \cdots = \frac{cr^2}{2}\sin 2\theta \qquad (r \le 1), \tag{3.17}$$

$$u_\theta = u_\theta(r,\theta,0) + \left.\frac{\partial u_\theta(r,\theta,z)}{\partial z}\right|_{z=0} \cdot \frac{cr^2}{2}\cos^2\theta + \cdots = 0 \qquad (r \le 1), \tag{3.18}$$

$$u_r = u_r(r,\theta,0) + \left.\frac{\partial u_r(r,\theta,z)}{\partial z}\right|_{z=0} \cdot \frac{cr^2}{2}\cos^2\theta + \cdots = 0 \qquad (r \le 1). \tag{3.19}$$

From this system, matching the terms of equal power of (cR), we obtain two problems to solve (choosing to stop at second order), where the interior boundary condition is now defined on a flat disc about the origin, of unitary radius:
First order

$$u_z^{(1)} = \frac{cr^2}{2}\sin 2\theta, \qquad u_\theta^{(1)} = 0, \qquad u_r^{(1)} = 0. \qquad (r \le 1) \tag{3.20}$$

Second order

$$u_z^{(2)} + \left.\frac{\partial u_z^{(1)}(r,\theta,z)}{\partial z}\right|_{z=0} \cdot \frac{cr^2}{2}\cos^2\theta = 0 \qquad (r \le 1), \tag{3.21}$$

$$u_\theta^{(2)} + \left.\frac{\partial u_\theta^{(1)}(r,\theta,z)}{\partial z}\right|_{z=0} \cdot \frac{cr^2}{2}\cos^2\theta = 0 \qquad (r \le 1), \tag{3.22}$$

$$u_r^{(2)} + \left.\frac{\partial u_r^{(1)}(r,\theta,z)}{\partial z}\right|_{z=0} \cdot \frac{cr^2}{2}\cos^2\theta = 0 \qquad (r \le 1). \tag{3.23}$$

For both the systems the boundary equation for the far field remains the standard one from (3.13). The problem has been reformulated as the solution of a sequence of subproblems, for increasing powers of the dimensionless curvature, where each problem involves boundary conditions defined on a flat disc instead of the deformed shell surface. In Taylor's case, the setting was two-dimensional: expressing the velocity as the derivative of a potential, and knowing the general solution for the potential of a Stokes problem, the problem then simplified in determining the constants of the terms of the potential, by imposing the boundary conditions. Here the problem cannot be as easily reduced to a 2D one, and a method is needed to find a solution for the systems given the boundary conditions. Therefore, in the following we consider a technique that allows to obtain the solutions fields for this kind of subproblems.

3.3 Solution strategy

To solve the Stokes equations we start from the approach of Tanzosh and Stone [57], who solve the problem of a disc in an unbounded viscous fluid, undergoing a generic rigid motion. The idea is to use the same technique, but with the slightly more complex boundary conditions that arise from the problem at hand. We briefly recall the approach in [57]. The Stokes

equations in cylindrical coordinates are:

$$0 = -\frac{\partial p}{\partial r} + \mathcal{L}_{-1}u_r + \frac{1}{r^2}\frac{\partial^2 u_r}{\partial \theta^2} - \frac{2}{r^2}\frac{\partial u_\theta}{\partial \theta} + \frac{\partial^2 u_r}{\partial z^2}, \tag{3.24}$$

$$0 = -\frac{\partial p}{\partial \theta} + \mathcal{L}_{-1}u_\theta + \frac{1}{r^2}\frac{\partial^2 u_\theta}{\partial \theta^2} + \frac{2}{r^2}\frac{\partial u_r}{\partial \theta} + \frac{\partial^2 u_\theta}{\partial z^2}, \tag{3.25}$$

$$0 = -\frac{\partial p}{\partial z} + \mathcal{L}_{0}u_z + \frac{1}{r^2}\frac{\partial^2 u_z}{\partial \theta^2} + \frac{\partial^2 u_z}{\partial z^2}, \tag{3.26}$$

$$0 = -\frac{1}{r}\frac{\partial}{\partial r}(r u_r) + \frac{1}{r}\frac{\partial u_\theta}{\partial \theta} + \frac{\partial u_z}{\partial z}, \tag{3.27}$$

the last one being the continuity equation, and having introduced the operator

$$\mathcal{L}_{-n} = \frac{\partial}{\partial r^2} + \frac{1}{r}\frac{\partial}{\partial r} - \frac{n^2}{r^2}. \tag{3.28}$$

For convenience u_r and u_θ are taken together by summing equations (3.24) $\pm i$ (3.25):

$$0 = -\left(\frac{\partial}{\partial r} + \frac{i}{r}\frac{\partial}{\partial \theta}\right)p + \left(\mathcal{L}_{-1} + \frac{1}{r^2}\frac{\partial^2}{\partial \theta^2} + \frac{\partial^2}{\partial z^2} + \frac{2i}{r^2}\frac{\partial}{\partial \theta}\right)(u_r + i u_\theta), \tag{3.29}$$

$$0 = -\left(\frac{\partial}{\partial r} - \frac{i}{r}\frac{\partial}{\partial \theta}\right)p + \left(\mathcal{L}_{-1} + \frac{1}{r^2}\frac{\partial^2}{\partial \theta^2} + \frac{\partial^2}{\partial z^2} - \frac{2i}{r^2}\frac{\partial}{\partial \theta}\right)(u_r - i u_\theta), \tag{3.30}$$

where one resulting equation is the complex conjugate of the other. Since the boundary conditions involve trigonometric dependencies on the azimuthal coordinate θ, and since the governing equations are linear, the velocity and pressure fields can be represented as expansions in complex Fourier modes $e^{in\theta}$. The general expression for the solutions will therefore be:

$$(u_r + i u_\theta) = \sum_{n=0}^{\infty}\left[U_{-n}(r,z)e^{-in\theta} + U_n(r,z)e^{in\theta}\right], \tag{3.31}$$

$$p = \sum_{n=0}^{\infty}\left[\bar{P}_n(r,z)e^{-in\theta} + P_n(r,z)e^{in\theta}\right], \tag{3.32}$$

$$u_z = \sum_{n=0}^{\infty}\left[\bar{W}_n(r,z)e^{-in\theta} + W_n(r,z)e^{in\theta}\right], \tag{3.33}$$

where it is already taken into account that p and u_z have to be real functions. It is important to note that if the different expansion orders are not coupled in the governing equations, nor in the boundary conditions, then a single mode characterizes the solution, with all other modes being identically zero [57]. Substituting the expansions (3.31)-(3.33) into equations (3.24)-(3.27) we obtain:

$$0 = -r^{-n}\frac{\partial}{\partial r}(r^n \bar{P}_n) + \left(\mathcal{L}_{-(n-1)} + \frac{\partial^2}{\partial z^2}\right)U_{-n}, \tag{3.34}$$

$$0 = -r^{n}\frac{\partial}{\partial r}(r^{-n} P_n) + \left(\mathcal{L}_{-(n+1)} + \frac{\partial^2}{\partial z^2}\right)U_{n}, \tag{3.35}$$

$$0 = -\frac{\partial P_n}{\partial z} + \left(\mathcal{L}_{-n} + \frac{\partial^2}{\partial z^2}\right)W_n, \tag{3.36}$$

$$0 = r^{-(n+1)}\frac{\partial}{\partial r}(r^{n+1}U_n) + r^{(n-1)}\frac{\partial}{\partial r}(r^{-(n-1)}\bar{U}_{-n}) + 2\frac{\partial W_n}{\partial z}. \tag{3.37}$$

Next, the system of PDEs is to be reduced to a system of ODEs in the variable z, that can be solved in closed form. To this end the integral Hankel transform is employed. The definition of Hankel transform of order n and wave-number k, and related inverse transform

are, respectively:

$$\Phi(k) = \mathcal{H}_n[\phi(r);k] \equiv \int_0^\infty r\phi(r)J_n(kr)dr, \tag{3.38}$$
$$\phi(r) = \mathcal{H}_n^{-1}[\Phi(k);r] \equiv \int_0^\infty k\Phi(k)J_n(kr)dk, \tag{3.39}$$

where J_n indicates a Bessel function of first kind of order n. This transform is useful for the case at hand thanks to its property of converting the radial operator $\mathcal{L}_{-n}$ into an algebraic expression:

$$\mathcal{H}_n\left[\mathcal{L}_{-n}\phi\right] = -k^2\mathcal{H}_n(\phi). \tag{3.40}$$

Other properties of the Hankel transform, that will be needed in order to simplify the system of equations are:

$$\mathcal{H}_{n+1}\left[r^n\frac{\partial}{\partial r}(r^{-n}\phi)\right] = -k\mathcal{H}_n[\phi], \tag{3.41}$$
$$\mathcal{H}_{n-1}\left[r^{-n}\frac{\partial}{\partial r}(r^{n}\phi)\right] = k\mathcal{H}_n[\phi], \tag{3.42}$$
$$\mathcal{H}_n\left[\frac{n\phi}{r}\right] = \frac{k}{2}\left(\mathcal{H}_{n-1}[\phi] + \mathcal{H}_{n+1}[\phi]\right). \tag{3.43}$$

To take advantage of these properties the transformed variables will be defined accordingly:

$$\mathcal{U}_n(k,z) \equiv \mathcal{H}_{n+1}[U_n(r,z)], \tag{3.44}$$
$$\mathcal{P}_n(k,z), \mathcal{W}_n(k,z) \equiv \mathcal{H}_n[P_n(r,z), W_n(r,z)], \tag{3.45}$$
$$\bar{\mathcal{U}}_{-n}(k,z) \equiv \mathcal{H}_{n-1}[\bar{U}_{-n}(r,z)]. \tag{3.46}$$

Now to obtain some simplifications, the $\mathcal{H}_{n-1}$ transform is applied to equation (3.34), and the complex conjugate of the result is taken. Furthermore, the $\mathcal{H}_n$ transform is applied to equations (3.36) and (3.37), and the $\mathcal{H}_{n+1}$ transform to equations (3.35). Thanks to the properties of the Hankel transform (reported above) it follows:

$$0 = -k\mathcal{P}_n(k,z) + \left(\frac{d^2}{dz^2} - k^2\right)\bar{\mathcal{U}}_{-n}(k,z), \tag{3.47}$$
$$0 = k\mathcal{P}_n(k,z) + \left(\frac{d^2}{dz^2} - k^2\right)\mathcal{U}_n(k,z), \tag{3.48}$$
$$0 = -\frac{d}{dz}\mathcal{P}_n(k,z) + \left(\frac{d^2}{dz^2} - k^2\right)\mathcal{W}_n(k,z), \tag{3.49}$$
$$0 = 2\frac{d}{dz}\mathcal{W}_n(k,z) + k\mathcal{U}_n(k,z) - k\bar{\mathcal{U}}_{-n}(k,z). \tag{3.50}$$

Combining these gives

$$\left(\frac{d^2}{dz^2} - k^2\right)(k\mathcal{U}_n - k\bar{\mathcal{U}}_{-n}) = -2k^2\mathcal{P}_n \Rightarrow 2\left(\frac{d^2}{dz^2} - k^2\right)\mathcal{W}_n'' = \mathcal{P}_n', \tag{3.51}$$

which allows to obtain a fourth order ODE in terms of $\mathcal{W}_n$ alone:

$$0 = \left(\frac{d^2}{dz^2} - k^2\right)^2\mathcal{W}_n, \tag{3.52}$$

while the relations that give the other (transformed) expansion coefficients are:

$$\mathcal{P}_n = \frac{1}{2k^2}(\mathcal{W}_n''' - k^2\mathcal{W}_n'), \tag{3.53}$$

$$\mathcal{U}_n - \bar{\mathcal{U}}_{-n} = -\frac{2}{k}\mathcal{W}_n', \tag{3.54}$$

$$(\mathcal{U}_n + \bar{\mathcal{U}}_{-n})'' - k^2(\mathcal{U}_n + \bar{\mathcal{U}}_{-n}) = 0. \tag{3.55}$$

All derivatives ($'$) here are in the variable z. These ODEs can then be solved easily, and only the terms that don't diverge for $z \to \infty$ are retained (that is, terms of the kind e^{-kz}). The solutions will be defined up to three unknown functions $A_1(k)$, $A_2(k)$ and $A_3(k)$, that depend implicitly on the expansion order n. These functions will be determined by the boundary conditions, once the appropriate inverse Hankel transform, as in (3.39), is taken. The problem has thus been reduced to finding the appropriate functions that satisfy

$$W_n(r,z) = \int_0^\infty k\left[A_1(k) + zA_2(k)\right]e^{-kz}J_n(kr)dk, \tag{3.56}$$

$$P_n(r,z) = \int_0^\infty 2kA_2(k)e^{-kz}J_n(kr)dk, \tag{3.57}$$

$$U_n(r,z) = \int_0^\infty k\left[A_3(k) + A_1(k) - A_2(k)\frac{1-kz}{k}\right]e^{-kz}J_{n+1}(kr)dk, \tag{3.58}$$

$$U_{-n}(r,z) = \int_0^\infty k\left[\bar{A}_3(k) - \bar{A}_1(k) + \bar{A}_2(k)\frac{1-kz}{k}\right]e^{-kz}J_{n-1}(kr)dk, \tag{3.59}$$

where the functions W_n, P_n, U_n, U_{-n} have to satisfy the appropriate boundary condition related to the corresponding Fourier mode (on the circular disc). Therefore, the problem is modified to calculating (or approximating) the integrals involving Bessel functions in equations (3.56-3.59). These equations are divided in two contributions: on the domain $Z = 0$, $r < 1$ the functions will need to satisfy the given boundary conditions due to the so-slip condition on the surface of the shell. Outside this region, for $r > 1$, $Z = 0$, the solution will need to satisfy the continuity of normal stresses on both sides of the disk [18]. Therefore, the coefficients $A_1(k)$, $A_2(k)$ and $A_3(k)$ (where we recall a dependence on the Fourier mode n is implicit), will follow from the solution of a series of dual integral equations. Provided that a solution to these problems can be found (or again, approximated), the solution of the Stokes flow will then be known, and integration of the stresses acting on the surface of the structure will allow to determine the net force and torque acting on the swimmer, and therefore the possible swimming motions.

3.3.1 First order iteration

The boundary condition (3.20) has to be expressed in terms of the Fourier coefficients

$$\bar{W}_n e^{-in\theta} + W_n e^{in\theta} = 2W_{n,R}\cos n\theta - 2W_{n,C}\sin n\theta, \tag{3.60}$$

to solve for $n = 2$, we enforce the boundary condition (3.20):

$$-2W_{2C} = \frac{cr^2}{2} \Rightarrow W_{2C} = -\frac{cr^2}{4}, \qquad W_{2R} = 0. \tag{3.61}$$

This boundary condition will be imposed in the disc $r \leq 1$, $z = 0$. For the domain $r > 1$, the conditions, if the velocity is perpendicular to the plane of the disc, are $\mathbf{e}_z \cdot \mathbf{T} \cdot \mathbf{e}_z = 0$, which translates in terms of modes to $-P_2 + 2W_2' = 0$. From (3.20) instead we obtain $U_{-2} = U_2 = 0$ at $Z = 0$, and thus we can take advantage of the simplifications $A_3 = 0$, $A_2 = kA_1$. The problem to be solved then is to determine only the function $A_1(k)$ for the mode $n = 2$, and

is of the form:

$$W_2(r,0): \qquad -i\frac{cr^2}{4} = \int_0^\infty kA_1(k)J_2(kr)dk \qquad \text{for } r<1, \tag{3.62}$$

$$-P_2+2W_2': \qquad 0 = \int_0^\infty k^2A_1J_2(kr)dk \qquad \text{for } r>1. \tag{3.63}$$

This dual integral equations problems are well known (see [56]) and, in some particular cases, solution strategies are available to attempt finding a solution in closed form. In the particular case at hand, the problem can be reformulated in such a way that the method exposed by Tranter [60] applies (see also Appendix 3.5). The solution will be:

$$A_1(k) = -i\frac{2c}{3}k^{-\frac{3}{2}}J_{\frac{5}{2}}(k)\sqrt{\frac{2}{\pi}} \tag{3.64}$$

and therefore the coefficients for the velocities [55] are:

$$U_2(r,z) = \int_0^\infty k^2A_1(k)ze^{-kz}J_3(kr)dk, \tag{3.65}$$

$$U_{-2}(r,z) = -\int_0^\infty k^2\bar{A}_1ze^{-kz}J_1(kr)dk, \tag{3.66}$$

$$W_2(r,z) = \int_0^\infty kA_1(1+kz)e^{-kz}J_2(kr)dk, \tag{3.67}$$

$$P_2(r,z) = \int_0^\infty 2k^2A_1e^{-kz}J_2(kr)dk. \tag{3.68}$$

Knowing these coefficients for the Fourier modes, the velocity fields can be obtained, applying (3.31)-(3.33) and retaining only the non-zero terms:

$$u_r^{(1)} = -\sin 2\theta(U_{2C}-U_{-2C}) = -\sin 2\theta\int_0^\infty k^2A_1(k)ze^{-kz}[J_3(kr)-J_1(kr)]dk, \tag{3.69}$$

$$u_\theta^{(1)} = \cos 2\theta(U_{2C}+U_{-2C}) = \cos 2\theta\int_0^\infty k^2A_1(k)ze^{-kz}[J_3(kr)+J_1(kr)]dk, \tag{3.70}$$

$$u_z^{(1)} = -\sin 2\theta(2W_{2C}) = -2\sin 2\theta\int_0^\infty kA_1(1+kz)e^{-kz}J_2(kr)dk, \tag{3.71}$$

$$p^{(1)} = -\sin 2\theta(2P_{2C}) = -2\sin 2\theta\int_0^\infty 2k^2A_1e^{-kz}J_2(kr)dk. \tag{3.72}$$

We note that $A_1(k)$ is complex in this case.

3.3.2 Second order iteration

From the first section we see now that, to pass to a second order approximation for the problem, we have

$$u_z^{(2)} = -\left.\frac{\partial u_z^{(1)}(r,\theta,z)}{\partial z}\right|_{z=0}\cdot\frac{cr^2}{2}\cos^2\theta \qquad (r\le 1), \tag{3.73}$$

$$u_\theta^{(2)} = -\left.\frac{\partial u_\theta^{(1)}(r,\theta,z)}{\partial z}\right|_{z=0}\cdot\frac{cr^2}{2}\cos^2\theta \qquad (r\le 1), \tag{3.74}$$

$$u_r^{(2)} = -\left.\frac{\partial u_r^{(1)}(r,\theta,z)}{\partial z}\right|_{z=0}\cdot\frac{cr^2}{2}\cos^2\theta \qquad (r\le 1). \tag{3.75}$$

We see immediately that the fields will have a different dependence on the azimuthal variable θ: the velocities u_z and u_r will be of the form $\cos^2\theta\sin 2\theta$, while u_θ will be of the form $\cos^2\theta\cos 2\theta$, thus for this last component the average in θ will not be zero, since $\cos^2\theta\cos 2\theta = \frac{1}{4}+\frac{\cos 2\theta}{2}+\frac{\cos 4\theta}{4}$. This is similar to what happens in Taylor's case, where at second order,

the solution has a non-zero average, and that component is precisely the net swimming effect [11]. From equation (3.74) an integral has to be calculated after the partial derivative in z (evaluated at 0). By using the well known recurrence identity

$$J_{n-1}(kr) + J_{n+1}(kr) = \frac{2n}{kr} J_n(kr), \tag{3.76}$$

and using the already known solution (3.64), we can easily calculate the integral

$$\frac{\partial u_\theta^{(1)}}{\partial z} = \int_0^\infty k^2 A_1(k)[J_3(kr) + J_1(kr)]dk = \frac{4}{r}\int_0^\infty k A_1(k) J_2(kr) dk = r. \tag{3.77}$$

Taking now only the term with non-zero average over 2π for the θ variable:

$$< u_\theta^{(2)} >=< -\frac{\partial u_\theta^{(1)}(r,\theta,z)}{\partial z}\Big|_{z=0} \frac{cr^2}{2}\cos^2\theta\cos 2\theta >=< \frac{c^2 r^3}{2}\cos^2\theta\cos 2\theta >= \frac{c^2 r^3}{8}, \tag{3.78}$$

$$< u_z^{(2)} >=< u_r^{(2)} >= 0. \tag{3.79}$$

The average problem, together with appropriate boundary conditions, yields another dual integral problem, which is similar to that of an in-plane rotation of the disk [57]. The conditions enforced can be obtained as in the previous iteration and, in terms of Fourier modes, will be $U_0 = i\frac{c^2 r^3}{8}$, $W_0 = 0$, for $r < 1$, and $U_0' = 0$, for $r > 1$. Based on these constraints it follows that now $A_1 = A_2 = 0$, and the problem reduces to the dual integral equations with the unknown $A_3(k)$:

$$U_0(r,0): \quad i\frac{c^2 r^3}{8} = \int_0^\infty k A_3(k) J_1(kr) dk \quad for\ r < 1, \tag{3.80}$$

$$U_0'(r,0): \quad 0 = \int_0^\infty k^2 A_3(k) J_1(kr) dk \quad for\ r > 1. \tag{3.81}$$

The method presented by Copson [16] (see also appendix 3.5) can be employed here to obtain:

$$A_3(k) = \frac{2}{\pi}\frac{-k(-6+k^2)\cos k + 3(-2+k^2)\sin k}{3k^5} = \frac{1}{2}\sqrt{\frac{2}{\pi}}k^{\frac{1}{2}}\left(-\frac{2}{3}J_{\frac{7}{2}}(k) + \frac{2}{k}J_{\frac{5}{2}}(k)\right). \tag{3.82}$$

Now following Sherwood [55], if we use the notation $A_3(k) = iB_3(k)$, then the velocity will be

$$u_\theta = \int_0^\infty k B_3(k) e^{-kz} J_1(kr) dk, \tag{3.83}$$

then the stress component of interest will be given by

$$\sigma_{\theta z} = \frac{\partial u_\theta}{\partial z} = \int_0^\infty k^2 B_3(k) e^{-kz} J_1(kr) dk. \tag{3.84}$$

If, introduce another approximation, we integrate this stress field over the flat disc $r < 1$, $z = 0$, then, exchanging integrals and using the relation

$$\int_0^1 J_1(kr) r^2 dr = \frac{J_2(k)}{k}, \tag{3.85}$$

we obtain the dependence of the torque on the value of the curvature:

$$L_z = 4\pi\int_{r=0}^1 \sigma_{\theta z} r^2 dr = 4\pi\int_0^1\int_0^\infty k^2 B_3(k) J_1(kr) dk r^2 dr = \frac{16}{15}c^2. \tag{3.86}$$

3.3.3 Results and discussion

The problem has recently been studied numerically in [17]: the Stokes problem was solved with a finite element discretization using the standard *P2/P1* elements for velocity and pressure. The system was solved monolithically with the *FEniCS* [2] finite element library and forces and torques were determined for a wide range of curvatures. It was expected by means of dimensional analysis that the torque acting on the solid would scale quadratically with the curvature, similarly to what happens in Taylor's case. Since the motion generated is of interest, an important result to calculate is the ratio between the rotational rate induced, denoted in the following as $\dot{\alpha}$, and the precession motion $\dot{\varphi}$. To obtain this value, one needs to know the rotation rate induced by a given torque. For a flat disc this value is known [34] to be $\frac{32}{3}$. Therefore, for small curvature values, we can use this value without introducing new approximations: given an actuation generating a precession $\dot{\varphi}$, the resulting net torque acting on the surface of the shell will be given by equation (3.86): $L_z = \frac{16}{15}c^2\dot{\varphi}$. Then, divinding this torque by the rotational resistance coefficient $\frac{32}{3}$ yields the induced rotational rate, that is:

$$\dot{\alpha} = \frac{1}{10}c^2\dot{\varphi}. \tag{3.87}$$

This value can then be compared with the numerical data, and to this end, in figure (3.5) we report the comparison between the analytic prediction and the numerical data from [17], showing a good agreement when the curvature is reasonably small. Several interesting points can be taken from the analysis above: the problem is similar to that of the Taylor sheet, in that the expansion of the boundary condition at first order, results in no motion. At second order instead, the result is a term with non-zero average in one component of the velocity, specifically the direction in which the wave of displacement travels (u_θ here). This results in a rotation or equivalently, in our setting, in a net torque with z axis. It is also confirmed that the other components of the velocity are zero, at least to this order of approximation: the main effect of the precession of the curvature axis thus is to generate a rotation. The analysis also confirms that, as expected by the dimensional argument, the dependence of the induced torque on the curvature is quadratic, at least for small values. From the comparison in figure 3.5 it is evident that the agreement of analytical and numerical data decreases of for higher values of curvature. This is expected since in the numerical study curvatures up to the geometrical limit, when the shell closes on itself and becomes a cylinder, were considered. For such cases the small curvature approximation clearly doesn't hold any more. Nonetheless, an interesting conclusion from the analysis above is that a neutrally stable shell, when actuated in such a way that a precession deformation occurs, can be a good candidate for a real-life realization of a circular Taylor's sheet.

3.4 Conclusions

We have shown that an asymptotic approach similar to that proposed by Taylor [59] can be applied to the case of a disc. The expansion in powers of the curvature results in a rotational motion, with amplitude depending quadratically on the curvature. The analytic result shows good agreement with the numerical data for small values of the curvature, supporting the predictions in [17]. As expected, the analytic prediction loses accuracy at higher values of curvature. The range of validity of the analysis could be widened by considering further terms in the power expansion, as in [52]. As directions of further investigation, we point out that different shapes of the shell could be considered, in particular the elliptic shape would be the rational extension to more general shapes while simple enough that an analytical approach might still be reasonably feasible. Furthermore, simulations for an elliptical shape in [17] show a richer behaviour than circular one. In addition, the effects of oscillatory motions

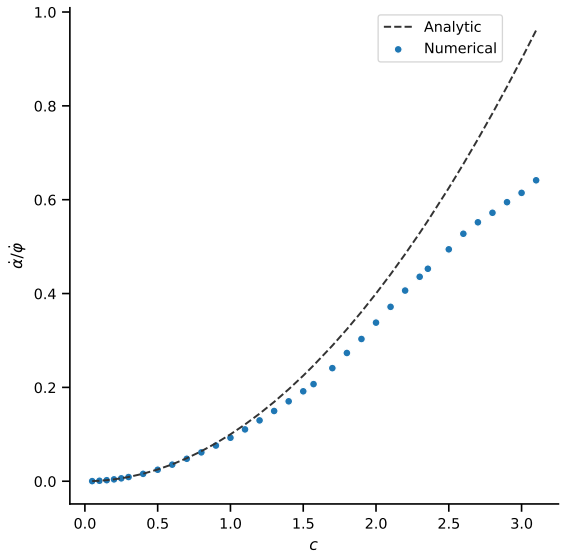

FIGURE 3.5: Rotational rate induced by the precession motion for a given value of the curvature (adimensional, the disk has $R = 1$). Dashed line: analytical estimate. Scatter plot: data from numerical simulations from [17]

.

and unsteadiness would be a natural extension of the model considered so far, as is done for example in [64], with methods involving dual integral equations.

3.5 Appendix - Solution methods for dual integral equations

The solution methods of Tranter and Copson [60, 16] are an example of strategies that allow to solve dual integral problems, when the conditions imposed on the integrals are simple enough that closed form solutions can be calculated. The idea is to express the solution in an alternate form involving integration with Bessel functions, such that the outer condition part of the dual integral equation is automatically satisfied. To better fix ideas, if we consider the generic problem of the form

$$\int_0^\infty \xi^{2\alpha}\psi(\xi)J_\nu(\xi r)\mathrm{d}\xi = f(r) \qquad 0 < r < 1, \tag{3.88}$$

$$\int_0^\infty \psi(\xi)J_\nu(\xi r)\mathrm{d}\xi = 0 \qquad r > 1, \tag{3.89}$$

then a good solution candidate would be given by introducing a further unknown function ϕ to have a solution ψ of the form:

$$\psi(\xi) = \xi^{1-\alpha}\int_0^1 \phi(t)J_{\nu+\alpha}(\xi t)dt. \tag{3.90}$$

This solution automatically satisfies condition (3.89). To see this, we need a simple lemma regarding properties of Bessel functions from [62]:
If $\lambda > \mu > -1$,

$$\int_0^\infty J_\lambda(at)J_\mu(bt)t^{1+\mu-\lambda}dt = \begin{cases} 0, & (0 < a < b) \\ \dfrac{b^\mu(a^2-b^2)^{\lambda-\mu-1}}{2^{\lambda-\mu-1}a^\lambda\Gamma(\lambda-\mu)}, & (0 < b < a) \end{cases} \tag{3.91}$$

The next step of the method is substituting the solution candidate in the inner problem, that is the first of the two integral equations, and obtain after manipulations an integral problem of which the closed form solution is known. In particual Tranter and Copson reduce the problem, after algebraic manipulations, to an integral Abel problem which is solvable for certain combinations of exponents of the special functions and the outer data. In more generality [18], integral equations of the kind

$$\int_0^r g(t)(r^2-t^2)^{-\alpha}\mathrm{d}t = h(r) \qquad 0 < r < R, \quad 0 < \alpha < 1, \tag{3.92}$$

arise. The solution to this problem is of the form

$$g(r) = \frac{2}{\pi}\sin(\alpha\pi)\frac{\mathrm{d}}{\mathrm{d}r}\int_0^r h(t)(r^2-t^2)^{\alpha-1}t\mathrm{d}t. \tag{3.93}$$

Once this solution has been calculated, going back all of the substitutions yields the originally function searched for. Clearly, it is assumed that all of the functions in the computations have sufficient regularity, and decay properties, for the manipulations to be justified.

Chapter 4

Study of a robotic swimmer inspired by Purcell

4.1 Introduction

Micro swimmers attract a lot of interest in research, both for their relation with the biological realm of microscopic organisms and for their importance as model problems for fundamental research. In a pioneering paper [50], Purcell proposed a framework for tackling such problems, as well as some notatational conventions which are still standard today. In the article, he considered a simple micro swimmer composed of a spherical head and a propeller, which serves as a simplified model of a flagellated micro-organism. Starting from the basics of Stokes flow theory and exploiting the properties of such flows, Purcell developed a simple theory to predict the functioning and efficiency of such a swimmer. He conceived the experiments needed to fully characterize the physical quantities needed to predict the behaviour of any real swimmer with the same features, namely, resulting from the assembly of a cargo and a chiral propeller. Such an elegant theory relied on some simplifications, that the author readily acknowledged, namely neglecting the hydrodynamic interaction between the two different components of the swimmer. Furthermore, the general approach will yield results close to the experiments only on the condition that the flow be realistically modelled by the Stokes equations. This of course is valid only when the size of the swimmer or the characteristics or the flow are such that the viscosity prevails and is the only contribution (or the largely dominant one) to the stresses that act on the immersed body. Translated in terms of non-dimensional parameters, the Reynolds number has to be zero or, in practice, very close to zero. Once the conditions deviate from this requirement, inertia contributions to the stresses are no longer negligible: a so-called *pressure drag* will also act on the swimmer. This drag is due to the different values of pressure in the front of the body (with respect to the swimming direction) and the rear, where instead a wake forms, resulting in a lower pressure recovery, and therefore in a net resistive force on the body not due to viscosity. This contribution will become more dominant with increasing Reynolds numbers and at the same time the wake will be more extended. Here, we intend to revisit the problem of swimming at low, but possibly finite, Reynolds numbers and put the framework of Purcell in this broader perspective, aided also by a numerical investigation. Our final goal is also, just as in [50], the comparison with an experimental study of a prototypical micro swimmer. This chapter is organized as follows: in section 4.2 we introduce the equations that govern the problem and consider the possible simplifications. In section 4.3 the details of the numerical tools employed are given, while in section 4.5 we report the numerical results. In section 4.4 we describe the protocol of the experimental investigation. Finally, based on the three points of view, theoretical, numerical and experimental, a discussion and conclusions on the results follow in section 4.6.

4.2 Qualitative analysis of the problem

We study self-propulsion under gravity, governed by the fact that the total torque $\mathbf{T}$ acting on the swimmer vanishes, and that the total force is that due to gravity. Including the latter in the total force $\mathbf{F}$ we can write the governing equations for the motion of the swimmer in the most general form possible as:

$$\mathbf{F} = \mathbf{F}(\mathbf{U}, \boldsymbol{\Omega}, \boldsymbol{\omega}) = \mathbf{0}, \tag{4.1}$$

$$\mathbf{T} = \mathbf{T}(\mathbf{U}, \boldsymbol{\Omega}, \boldsymbol{\omega}) = \mathbf{0}. \tag{4.2}$$

The total force and torque acting on the body, $\mathbf{F}$ and $\mathbf{T}$, are non-linear and depend on the translational velocity of the body, rotation of the head and rotation of the helicoidal propeller (relative to the head), respectively $\mathbf{U}$, $\boldsymbol{\Omega}$ and $\boldsymbol{\omega}$. These two terms in general can also contain contributions due to the inertia of the swimmer. We assume that the head has an axis of rotational symmetry. From this starting point, numerous simplifications can be obtained, yielding different models with different approximations introduced. One such model we wish to obtain is the one of Purcell [50].

4.2.1 The case of the rigid body

For sake of simplicity we first focus on the case of rigid swimmer ($\boldsymbol{\omega} = \mathbf{0}$), with two degrees of freedom: rotation about the symmetry axis of the head ($\boldsymbol{\Omega}$) and translation along the same axis ($\mathbf{U}$). To make equations above more explicit, we consider all the possible contributions: inertial terms, pressure drag, drag due to viscosity (*skin-friction*) and, if present, external gravity force. The equations that govern the motion of the body will be in general a system of non-linear ODEs coupled with a model for the flow, in the most general case the Navier-Stokes equations. Since the equations are non-linear, one might wonder whether the distinction among different force contributions still makes sense. For example, it would be desirable to write the pressure terms in the elegant (and easier to treat) form of the *added mass*, as is usually done in potential flow theory. Indeed, it has been shown (see for example [46] and references therein) that for the parameters of the present investigation (low but finite Reynolds numbers) the concept of *added mass* is still valid, even if the flow is no longer irrotational. Therefore, equations (4.1) and (4.2) can be rewritten in the form [46]:

$$(m\mathbb{I} + \mathbb{A})\frac{d\mathbf{U}}{dt} + \boldsymbol{\Omega} \times ((m\mathbb{I} + \mathbb{A})\mathbf{U}) = \mathbf{F}_\omega + (m - \rho\mathcal{V})\mathbf{g}, \tag{4.3}$$

$$(\mathbb{J} + \mathbb{D})\frac{d\boldsymbol{\Omega}}{dt} + \boldsymbol{\Omega} \times ((\mathbb{J} + \mathbb{D})\boldsymbol{\Omega}) + \mathbf{U} \times (\mathbb{A}\mathbf{U}) = \boldsymbol{\Gamma}_\omega, \tag{4.4}$$

where $m\mathbb{I}$ and $\mathbb{J}$ are the tensors of mass and moments of inertia, while $\mathbb{A}$ and $\mathbb{D}$ are the added mass contributions for translation and rotation, respectively. The force $\mathbf{F}_\omega$ and torque $\boldsymbol{\Gamma}_\omega$ are due to presence of vorticity in the flow and are derived by solving the PDEs that govern the motion of the fluid. We note that if we only allow the swimmer to have one translational and one rotational degrees of freedom, with the same axes, the equations above simplify, as some terms are identically zero:

$$(m\mathbb{I} + \mathbb{A})\frac{d\mathbf{U}}{dt} = \mathbf{F}_\omega + (m - \rho\mathcal{V})\mathbf{g}, \tag{4.5}$$

$$(\mathbb{J} + \mathbb{D})\frac{d\boldsymbol{\Omega}}{dt} = \boldsymbol{\Gamma}_\omega, \tag{4.6}$$

4.2.2 Derivation of the generalized ODEs for the body motion

We now report a derivation of the equations (4.3,4.4) above, starting first from the assumption of potential flow, which will then be removed. In this case all six degrees of freedom for the rigid body motion are allowed: later on we will restrict to one rotational and one translational degree of freedom as it's done in Purcell's work. Following the approach of [38, 44] for an irrotational unbounded fluid, initially at rest and whose motion is due solely to that of the solid, we introduce a problem for the velocity potential:

$$\Delta\phi = 0, \qquad \nabla\phi = 0 \text{ for } |\mathbf{r}| \to \infty, \tag{4.7}$$

which, if the solid is undergoing a rigid motion with velocity $\mathbf{U} + \boldsymbol{\Omega} \times \mathbf{r}$, will satisfy the boundary conditions

$$\frac{\partial\phi}{\partial n} = \mathbf{n} \cdot (\mathbf{U} + \boldsymbol{\Omega} \times \mathbf{r}) = \mathbf{n} \cdot \mathbf{U} + \boldsymbol{\Omega} \cdot (\mathbf{r} \times \mathbf{n}) \,. \tag{4.8}$$

We can write

$$\phi = \mathbf{U} \cdot \boldsymbol{\varphi} + \boldsymbol{\Omega} \cdot \boldsymbol{\chi}, \tag{4.9}$$

where the components of $\boldsymbol{\varphi}$, $\boldsymbol{\chi}$ both satisfy a Laplace equation with a gradient vanishing at infinity, and with the boundary conditions

$$-\frac{\partial\boldsymbol{\varphi}}{\partial n} = \mathbf{n}, \qquad -\frac{\partial\boldsymbol{\Omega}}{\partial n} = (\mathbf{r} \times \mathbf{n}) \,. \tag{4.10}$$

This implies that the two vector functions $\boldsymbol{\varphi}, \boldsymbol{\chi}$ depend only on the shape of the solid and not on the motion. Now, focusing on the fluid, the kinetic energy will be:

$$T_F = -\frac{1}{2}\rho \int_S \phi \frac{\partial\phi}{\partial n} dS = \frac{1}{2}\rho \int_S (\mathbf{U} \cdot \boldsymbol{\varphi} + \boldsymbol{\Omega} \cdot \boldsymbol{\chi}) \, (\mathbf{n} \cdot [\mathbf{U} + \boldsymbol{\Omega} \times \mathbf{r}]) \, dS, \tag{4.11}$$

where the integral is taken over the boundary of the solid. Therefore, we see that the kinetic energy is a homogeneous quadratic function of the components of the velocity of the solid, and therefore, by Euler's theorem on homogeneous functions [44], it follows that:

$$\mathbf{U} \cdot \frac{\partial T_F}{\partial \mathbf{U}} + \boldsymbol{\Omega} \cdot \frac{\partial T_F}{\partial \boldsymbol{\Omega}} = 2T_F. \tag{4.12}$$

Applying boundary conditions

$$\frac{\partial}{\partial \mathbf{U}} \left(\phi \frac{\partial\phi}{\partial n} \right) = -\mathbf{n}\phi + \boldsymbol{\varphi} \frac{\partial\phi}{\partial n} \Rightarrow \frac{\partial T_F}{\partial \mathbf{U}} = \frac{1}{2}\rho \int_S \mathbf{n}\phi dS - \frac{1}{2}\rho \int_S \boldsymbol{\varphi} \frac{\partial\phi}{\partial n} dS, \tag{4.13}$$

and using Green's theorem

$$\int_S \boldsymbol{\varphi} \frac{\partial\phi}{\partial n} dS = \int_S \phi \frac{\partial\boldsymbol{\varphi}}{\partial n} dS = -\int_S \mathbf{n}\phi dS. \tag{4.14}$$

It follows that:

$$\frac{\partial T_F}{\partial \mathbf{U}} = \rho \int_S \mathbf{n}\phi dS, \qquad \frac{\partial T_F}{\partial \boldsymbol{\Omega}} = \rho \int_S (\mathbf{r} \times \mathbf{n}) \, \phi dS, \tag{4.15}$$

where the second identity follows by a similar argument. As expected, the partial derivatives of the kinetic energy of the fluid are linear homogeneous functions of the components of the velocity of the solid. Turning to the solid, the expression for the kinetic energy reads:

$$T_S = \frac{1}{2} \int_V \sigma \, [\mathbf{U} + \boldsymbol{\Omega} \times \mathbf{r}]^2 \, dV, \tag{4.16}$$

where the integral is on the volume of the solid, whose density is denoted by σ. Applying again Euler's theorem:

$$\mathbf{U} \cdot \frac{\partial T_S}{\partial \mathbf{U}} + \boldsymbol{\Omega} \cdot \frac{\partial T_S}{\partial \boldsymbol{\Omega}} = 2T_S, \tag{4.17}$$

from which, substituting, we obtain:

$$\frac{\partial T_S}{\partial \mathbf{U}} = \sigma \int_V (\mathbf{U} + \boldsymbol{\Omega} \times \mathbf{r})\, dV = \mathbf{M}_S, \qquad \frac{\partial T_S}{\partial \boldsymbol{\Omega}} = \sigma \int_V \mathbf{r} \times (\mathbf{U} + \boldsymbol{\Omega} \times \mathbf{r})\, dV = \mathbf{H}_S, \tag{4.18}$$

which are the linear and angular momentum of the solid, respectively.

Now, for any given motion of the solid, we define as *impulse* the force and couple which would generate such motion instantaneously when applied to the body from rest. That is, the impulse produces instantaneously in the solid the momentum which it possesses at the given time for the given motion, and also overcomes the resistive impulsive pressures exerted by the liquid, due to the sudden variation of velocity. Calling $\boldsymbol{\xi}$, $\boldsymbol{\lambda}$ the force and couple of the impulse, it holds that, in an inertial frame of reference [44]:

$$\frac{\partial \boldsymbol{\xi}}{\partial t} = \mathbf{F}, \qquad \frac{\partial \boldsymbol{\lambda}}{\partial t} = \mathbf{M}, \tag{4.19}$$

where $\mathbf{F}$ and $\mathbf{M}$ are the external force and couple acting on the solid. This is a straightforward application of Newton's second law, and clarifies that the impulse is in fact an incremental momentum variation. The impulse $\boldsymbol{\lambda}$ and the external torque $\mathbf{M}$ here have to be referred to the same base point. Projecting these equations on a system of axes that rotates with the body yields:

$$\frac{\partial \boldsymbol{\xi}}{\partial t} + \boldsymbol{\Omega} \times \boldsymbol{\xi} = \mathbf{F}, \tag{4.20}$$

$$\frac{\partial \boldsymbol{\lambda}}{\partial t} + \boldsymbol{\Omega} \times \boldsymbol{\lambda} + \mathbf{u} \times \boldsymbol{\xi} = \mathbf{L}. \tag{4.21}$$

Now the work done by the impulse will result in an increase of the total kinetic energy of the system, $T = T_F + T_S$. Indeed it holds [44]:

$$\boldsymbol{\xi} = \frac{\partial T}{\partial \mathbf{u}}, \qquad \boldsymbol{\lambda} = \frac{\partial T}{\partial \boldsymbol{\Omega}}, \tag{4.22}$$

so that we finally obtain Kirchhoff's equations of motion in vector form

$$\frac{d}{dt}\left(\frac{\partial T}{\partial \mathbf{U}}\right) + \boldsymbol{\Omega} \times \frac{\partial T}{\partial \mathbf{U}} = \mathbf{F}, \tag{4.23}$$

$$\frac{d}{dt}\left(\frac{\partial T}{\partial \boldsymbol{\Omega}}\right) + \boldsymbol{\Omega} \times \frac{\partial T}{\partial \boldsymbol{\Omega}} + \mathbf{U} \times \frac{\partial T}{\partial \mathbf{U}} = \mathbf{L}. \tag{4.24}$$

Separating again the contribution of fluid and solid, $T = T_F + T_S$

$$\frac{d}{dt}\left(\frac{\partial T_S}{\partial \mathbf{U}}\right) + \boldsymbol{\Omega} \times \frac{\partial T_S}{\partial \mathbf{U}} = \mathbf{F} - \frac{d}{dt}\left(\frac{\partial T_F}{\partial \mathbf{U}}\right) - \boldsymbol{\Omega} \times \frac{\partial T_F}{\partial \mathbf{U}}, \tag{4.25}$$

$$\frac{d}{dt}\left(\frac{\partial T_S}{\partial \boldsymbol{\Omega}}\right) + \boldsymbol{\Omega} \times \frac{\partial T_S}{\partial \boldsymbol{\Omega}} + \mathbf{U} \times \frac{\partial T_S}{\partial \mathbf{U}} = \mathbf{L} - \frac{d}{dt}\left(\frac{\partial T_F}{\partial \boldsymbol{\Omega}}\right) - \boldsymbol{\Omega} \times \frac{\partial T_F}{\partial \boldsymbol{\Omega}} - \mathbf{U} \times \frac{\partial T_F}{\partial \mathbf{U}}. \tag{4.26}$$

If now we introduce the *added mass* matrix, such that

$$\frac{\partial T_F}{\partial \mathbf{U}} = \mathbb{A}, \qquad \frac{\partial T_F}{\partial \boldsymbol{\Omega}} = \mathbb{D}, \tag{4.27}$$

we can write equations (4.26) in the form

$$(m\mathbb{I} + \mathbb{A})\,\frac{d\mathbf{U}}{dt} + \boldsymbol{\Omega} \times ((m\mathbb{I} + \mathbb{A})\,\mathbf{U}) = \mathbf{F}_\omega + (m - \rho\mathcal{V})\,\mathbf{g}, \tag{4.28}$$

$$(\mathbb{J} + \mathbb{D})\,\frac{d\boldsymbol{\Omega}}{dt} + \boldsymbol{\Omega} \times ((\mathbb{J} + \mathbb{D})\,\boldsymbol{\Omega}) + \mathbf{U} \times (\mathbb{A}\mathbf{U}) = \boldsymbol{\Gamma}_\omega, \tag{4.29}$$

which is the same form reported above. Now the forces acting on the body may contain also those that were not modelled by the potential flow assumption, namely the viscous forces and the buoyancy forces. This simple addition of the viscous stresses, keeping the added mass contribution separate, is an acceptable approximation for the range of low Reynolds numbers considered [46]. The added mass terms model the response of the surrounding fluid to a sudden change in the motion of the body. Therefore, it takes the response resulting in pressure changes into account. One might also consider what is the influence of the viscous stresses in these short time scales, a contribution that can be seen as some kind of *history* force [6]. However, at very short time scales the pressure contribution is dominant and the viscous history forces only become relevant if the body has a density much lower than that of the surrounding fluid (see [6] for details).

Mass matrix

The values of the entries of the mass matrix $\mathbb{A}$ can be easily obtained for a body of any shape, surrounded by an unbounded fluid, considering irrotational flow theory. For a potential flow, which is linear, one can define the functions

$$u_i(\mathbf{x}) = u_{ij}(\mathbf{x})U_j \tag{4.30}$$

where U_j are the body velocities (summation is implicit for repeated indexes), and $u_{ij}(\mathbf{x})$ are the fluid velocities (at point $\mathbf{x}$ of the fluid domain) induced by a unit velocity of the solid in the *j-th* component, considering both translational and rotational degrees of freedom (here $i, j = 1, \ldots, 6$). The total kinetic energy can then be written as

$$T_F = \frac{1}{2}\mathbb{A}\mathbf{V} \cdot \mathbf{V}, \tag{4.31}$$

where the matrix $\mathbb{A}$ is now given by

$$\mathbb{A}_{jk} = \rho \int_V u_{ij} u_{ik} dV, \tag{4.32}$$

with integration over the whole fluid domain. Since the flow is potential, if ϕ_j denotes the velocity potential relative to the steady motion of the fluid due to a unitary velocity of the solid in the *j-th* component. It holds:

$$u_{ij} = \frac{\partial \phi_j}{\partial x_i}. \tag{4.33}$$

Substitution in (4.32) and application of Green's theorem results in the formula

$$\mathbb{A}_{jk} = -\rho \int_S \phi_j \frac{\partial \phi_k}{\partial n} dS, \tag{4.34}$$

where now the integration is carried over the surface of the body. These relations show that, in practice, the values of the mass matrix can be calculated as follows: a unitary value for one of the degrees of freedom is imposed on the surface of the body, for a system of fluid and body initially at rest. The linear potential flow equations are then solved to obtain the resulting

pressure exerted by the fluid on the body due to this sudden change in velocity. Integration of these pressure stresses over the surface of the moving body yields the components of the force and torque due to the resistance of the fluid. After a change of signs, these six components represent a column of the mass matrix corresponding to the degree of freedom of the motion that was imposed.

4.2.3 Qualitative analysis

Starting from the final form of the system of equations (4.28,4.29), one can derive a series of problems of decreasing complexity, introducing further assumptions:

- **General Case** - in the most general case the system (4.28,4.29) has to be solved, that is, a system of non-linear ODEs in the unknowns $\mathbf{U}(t), \mathbf{\Omega}(t)$, with initial conditions $\mathbf{U}(0) = \mathbf{U}_0, \mathbf{\Omega}(0) = \mathbf{\Omega}_0$. The ODE structure of the system is only formal, since the viscous contributions to the forces on the RHS depend on the flow model, usually a system of PDEs.

- **Steady state** - the system becomes

$$\mathbf{\Omega} \times ((m\mathbb{I} + \mathbb{A})\,\mathbf{U}) = \mathbf{F}_\omega + (m - \rho\mathcal{V})\,\mathbf{g}, \tag{4.35}$$
$$\mathbf{\Omega} \times ((\mathbb{J} + \mathbb{D})\,\mathbf{\Omega}) + \mathbf{U} \times (\mathbb{A}\mathbf{U}) = \mathbf{\Gamma}_\omega, \tag{4.36}$$

  where now a system which is formally algebraic in the unknowns is to be solved for (with the implicit coupling with the fluid model through the viscous forcing).

- **Symmetry** - special solutions can be found if the body possesses an axis of symmetry: denoting $\boldsymbol{\xi}$ the axis of symmetry, it follows that $\mathbb{A}\boldsymbol{\xi} \parallel \boldsymbol{\xi}$, $\mathbb{D}\boldsymbol{\xi} \parallel \boldsymbol{\xi}$, and $\mathbb{J}\boldsymbol{\xi} \parallel \boldsymbol{\xi}$. Therefore, looking for solutions of the form $\mathbf{U} = U\boldsymbol{\xi}$, $\mathbf{\Omega} = \Omega\boldsymbol{\xi}$ we obtain after substitution in the (steady state) equations above:

$$\mathbf{0} = \Omega U\,(\boldsymbol{\xi} \times (m\mathbb{I} + \mathbb{A})\,\boldsymbol{\xi}) = \mathbf{F}_\omega\,(U\boldsymbol{\xi}, \Omega\boldsymbol{\xi}) + (m - \rho\mathcal{V})\,\mathbf{g}, \tag{4.37}$$
$$\mathbf{0} = \Omega^2\,(\boldsymbol{\xi} \times (\mathbb{J} + \mathbb{D})\,\boldsymbol{\xi}) + U^2\boldsymbol{\xi} \times (\mathbb{A}\boldsymbol{\xi}) = \mathbf{\Gamma}_\omega\,(U\boldsymbol{\xi}, \Omega\boldsymbol{\xi})\,, \tag{4.38}$$

  that is,

$$\mathbf{F}_\omega\,(U\boldsymbol{\xi}, \Omega\boldsymbol{\xi}) + (m - \rho\mathcal{V})\,\mathbf{g} = \mathbf{0}, \tag{4.39}$$
$$\mathbf{\Gamma}_\omega\,(U\boldsymbol{\xi}, \Omega\boldsymbol{\xi}) = \mathbf{0}. \tag{4.40}$$

- **Stokes flow** - the viscous forces and torques exerted by the fluid on the body will have a linear dependence on its rigid motion in the case of creeping flow (pressure contributions cancel out in this case). The fluid behaviour will be fully described by the coefficients of the resistance matrix

$$\begin{pmatrix} \mathbf{F}_\omega\,(\mathbf{U}, \mathbf{\Omega}) \\ \mathbf{\Gamma}_\omega\,(\mathbf{U}, \mathbf{\Omega}) \end{pmatrix} = \begin{pmatrix} \mathbb{K}_{UU} & \mathbb{K}_{U\Omega} \\ \mathbb{K}_{\Omega U} & \mathbb{K}_{\Omega\Omega} \end{pmatrix} \begin{pmatrix} \mathbf{U} \\ \mathbf{\Omega} \end{pmatrix}. \tag{4.41}$$

  Substituting $\mathbf{F}_\omega = -\,(m - \rho\mathcal{V})\,\mathbf{g}$ and $\mathbf{\Gamma}_\omega = \mathbf{0}$, one gets the inverse problem for the case of self-propulsion under gravity

$$\begin{pmatrix} \mathbf{U} \\ \mathbf{\Omega} \end{pmatrix} = \mathbb{K}^{-1} \begin{pmatrix} (m - \rho\mathcal{V})\,\mathbf{g} \\ \mathbf{0} \end{pmatrix}. \tag{4.42}$$

  If the body has no chirality, that is if the matrix $\mathbb{K}$ is block diagonal, then since the two sub matrices $\mathbb{K}_{UU}$ and $\mathbb{K}_{\Omega\Omega}$ are symmetric and negative definite one readily obtains the

explicit solution

$$\mathbf{U} = \mathbb{K}_{UU}^{-1} (m - \rho\mathcal{V})\, \mathbf{g}, \qquad \boldsymbol{\Omega} = \mathbf{0}. \tag{4.43}$$

- **Stokes flow - Purcell's framework** The resistance matrix $\mathbb{K}$ above depends on the geometry of the body. The swimmer is composed of a head and a helical propeller, which have very different resistance characteristics. Furthermore, the helix will have a non-diagonal resistance matrix because of its chirality. In the notation of Purcell, given that there are only two degrees of freedom allowed for the rigid body motion, we can denote the coefficients of the resistance matrix describing the translational resistance, the off-diagonal coupling term and the rotational resistance, respectively, as A, B, and D. We only define one off-diagonal coefficient given that the resistance matrix must be symmetrical. Purcell then introduces a further simplification, namely that of considering the contributions of head and helix resistances as perfectly additive. Therefore, the resistance matrix of the swimmer is simply the sum of those of the head and helix when considered separately. This is an approximation, as Purcell acknowledges, that is only valid if the hydrodynamic interactions between head and tail can be neglected. These interactions may be significant [27]. When valid, this approximation leads to a simple and elegant prediction of the behaviour of the swimmer, that will be easily extended to the case when the helix is actuated by a motor. With this additive approximation we have:

$$\mathbb{K} = \begin{pmatrix} A & B \\ B & D \end{pmatrix} = \mathbb{K}_{(1)} + \mathbb{K}_{(2)}, \tag{4.44}$$

where 1 and 2 indicate the head and the helix, respectively. In terms of coefficients, in Purcell's notation:

$$A = A_{(1)} + A_{(2)}, \qquad B = B_{(2)}, \qquad D = D_{(1)} + D_{(2)}. \tag{4.45}$$

4.2.4 Generalization to the deformable case

We will consider a further case when the body is "deformable". By "deformable" here we mean that the helix and the head will no longer rotate with the same rate. We will assume that the motor that connects head and propeller, when actuated, is able to perfectly enforce a relative rotation rate between the two components of the swimmer. This introduces an additional degree of freedom, even though the velocity will be specified and constant. Due to the addition of this relative rotation, some modifications to the above equations are in order. For the general case of motion in a non-linear flow, the motion will now be dictated by the balance of the resistive torques on the head and helix, with the addition of the rotational inertia of the swimmer:

$$(\mathbb{J} + \mathbb{D}) \frac{d\boldsymbol{\Omega}}{dt} = \mathbf{M}_{\text{HEAD}} + \mathbf{M}_{\text{HELIX}}. \tag{4.46}$$

In the framework of Purcell this balance can be solved directly, and the swimming velocity for a given relative rotation Ω_m imposed by the motor is readily obtained as a function of the resistance coefficients:

$$v_z = -\frac{B_{(2)} D_{(1)}}{(A_{(1)} + A_{(2)})(D_{(1)} + D_{(2)}) - B_{(2)}^2} \Omega_m. \tag{4.47}$$

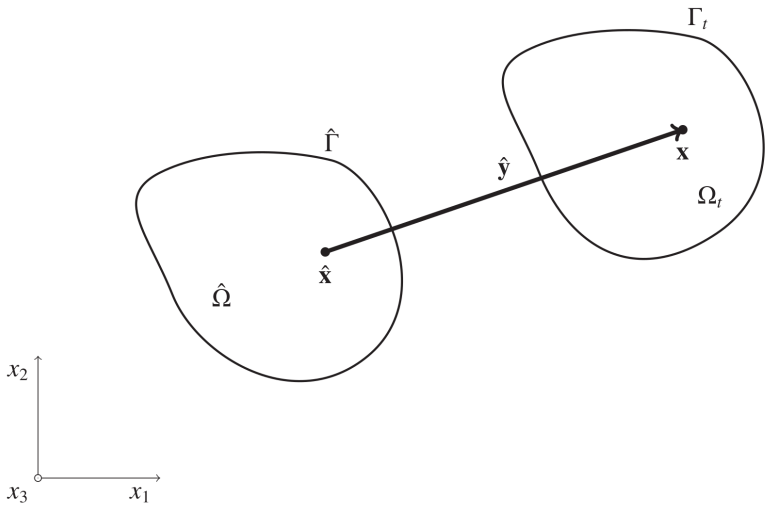

FIGURE 4.1: Reference domain in the ALE framework (from [8]).

4.3 Numerical methods and validation

4.3.1 Equations for the fluid

Taking [46] as reference, we study a body undergoing a time dependent rigid motion, with velocity $\mathbf{W}(t) = \mathbf{U}(t) + \mathbf{\Omega}(t) \times \mathbf{r}$. A control volume moving with the body is considered. Each time the fluid equations are solved, in order to advance for one time-step, the two vectors, $\mathbf{U}$, $\mathbf{\Omega}$ are temporarily frozen: they are subsequently updated when the solid equations are advanced in time. The mesh will thus be body fitted and follow the rigid motion. To take this into account, the flow equations will be cast in the *Arbitrary Lagrangian Eulerian* (ALE) framework. Following [8], one defines a reference configuration for the fluid domain, as in figure 4.1: this reference domain can be arbitrary, since there is no physical meaning attached to it, but for convenience at $t = 0$ it will be surrounding the solid domain, which will in turn be identified with the solid reference configuration. The fluid spatial domain is defined as:

$$\Omega_t = \{x \big| x = \phi(\hat{x}, t) \quad \forall \hat{x} \in \hat{\Omega}, t \in (0, T)\}, \tag{4.48}$$

where ϕ is the mapping from the referential fluid domain into the current spatial one. It takes the form

$$\phi(\hat{x}, t) = \hat{x} + \hat{y}(\hat{x}, t), \tag{4.49}$$

where $\hat{y}$ is the displacement of the fluid domain. One can then define the velocity of the fluid domain (or, equivalently, of the mesh points) as:

$$\hat{\mathbf{u}} = \left.\frac{\partial \hat{y}}{\partial t}\right|_{\hat{x}}, \tag{4.50}$$

and also an associated deformation gradient

$$\hat{\mathbf{F}} = \frac{\partial x}{\partial \hat{x}} = \mathbf{I} + \frac{\partial \hat{y}}{\partial x}, \tag{4.51}$$

and a Jacobian $\hat{J} = \det\hat{\mathbf{F}}$. A vector field can then be pulled back from the spatial domain to the reference one by the Piola transform

$$\hat{\boldsymbol{\gamma}} = \hat{J}\hat{\mathbf{F}}^{-1}\boldsymbol{\gamma}, \tag{4.52}$$

which has the property of preserving the conservation structure of the governing equations [8]:

$$\int_{\Omega_t} \nabla \cdot \boldsymbol{\gamma} d\Omega = \int_{\hat{\Omega}} \nabla_{\hat{x}} \cdot \hat{\boldsymbol{\gamma}} d\hat{\Omega}. \tag{4.53}$$

Now, one defines the space-time referential configuration by extruding $\hat{\Omega}$ in time

$$\hat{Q} = \hat{\Omega} \times (0, T) = \{(\hat{x}, t) \big| \forall \hat{x} \in \hat{\Omega}, t \in (0, T)\}, \tag{4.54}$$

while the current space-time domain will be given by

$$Q_t = \{(x, t) \big| \begin{pmatrix} t \\ x \end{pmatrix} = \begin{pmatrix} t \\ \phi(\hat{x}, t) \end{pmatrix} \forall (\hat{x}, t) \in \hat{Q}\}. \tag{4.55}$$

The gradient of the transformation from $\hat{\Omega}$ to Q_t will be

$$\hat{\mathbf{F}}_t = \begin{pmatrix} 1 & \mathbf{0}^T \\ \hat{\mathbf{u}} & \hat{\mathbf{F}} \end{pmatrix}, \tag{4.56}$$

and its determinant will be, again, equal to $\hat{J}$. The expressions are simplified because time is the same for the two frames. For this case, a (space-time) Piola transformation can be defined as well [8]: given a field $(\gamma_0, \boldsymbol{\gamma})^T$ defined on Q_t, the transformed vector field $(\hat{\gamma}_0, \hat{\boldsymbol{\gamma}})$ will be

$$\begin{pmatrix} \hat{\gamma}_0 \\ \hat{\boldsymbol{\gamma}} \end{pmatrix} = \hat{J} \begin{pmatrix} 1 & \mathbf{0}^T \\ \hat{\mathbf{u}} & \hat{\mathbf{F}} \end{pmatrix} \begin{pmatrix} \hat{\gamma}_0 \\ \boldsymbol{\gamma} \end{pmatrix} = \begin{pmatrix} \hat{J}\hat{\gamma}_0 \\ \hat{J}\hat{\mathbf{F}}^{-1}(\boldsymbol{\gamma} - \gamma_0 \hat{\mathbf{u}}) \end{pmatrix}. \tag{4.57}$$

This transformation also preserves the conservation property of a space-time vector field

$$\int_{Q_t} \left(\frac{\partial \gamma_0}{\partial t} + \nabla \cdot \boldsymbol{\gamma} \right) dQ = \int_{\hat{Q}} \left(\frac{\partial \hat{\gamma}_0}{\partial t} \bigg|_{\hat{x}} + \nabla_{\hat{x}} \cdot \hat{\boldsymbol{\gamma}} \right) d\hat{Q}, \tag{4.58}$$

where on the left-hand side the time derivative is intended for a constant mesh point $\hat{x}$. This general structure can then be applied to the incompressible Navier-Stokes equations, written at the beginning in the classical Eulerian (or spatial) form:

$$\frac{\partial \mathbf{u}}{\partial t} + \nabla \cdot (\mathbf{u} \otimes \mathbf{u} - \boldsymbol{\sigma}) - \mathbf{f} = \mathbf{0}, \tag{4.59}$$

subject to the usual constraint $\nabla \cdot \mathbf{u} = 0$. The classical approach for the discretization of equation (4.59), which will be followed here, is the semi-discrete one, that is a finite difference discretization for the time derivatives and then a spatial discretization (in this case with finite elements) of the resulting problem. Integrating (first in space and then in time) yields:

$$\int_{Q_t} \left(\frac{\partial \mathbf{u}}{\partial t} + \nabla \cdot (\mathbf{u} \otimes \mathbf{u} - \boldsymbol{\sigma}) - \mathbf{f} \right) dQ = \mathbf{0}, \tag{4.60}$$

or, in index notation

$$\int_{Q_t} \left(\left(\hat{J} u_i \right)_{,t} \bigg|_{\hat{x}} + \left(\hat{J} \left(u_i (u_j - \hat{u}_j) - \sigma_{ij} \right) \hat{F}^{-1}_{Jj} \right)_{,J} - \hat{J} f_i \right) d\hat{Q} = 0, \tag{4.61}$$

where the pull-back from Q_t to $\hat{Q}$, as shown in equations (4.57-4.58), has been applied. Here, upper case indices are used for the components in the referential domain, while lower case indices are used in the spatial domain. Now, since the reference domain is constant and

independent on time, this last equation can be localized in time to obtain

$$\int_{\hat{\Omega}} \left(\left(\hat{J} u_i \right)_{,t} \Big|_{\hat{x}} + \left(\hat{J} \left(u_i (u_j - \hat{u}_j) - \sigma_{ij} \right) \hat{F}^{-1}_{Jj} \right)_{,J} - \hat{J} f_i \right) d\hat{\Omega} = 0. \tag{4.62}$$

Then, equation (4.62) can be pushed forward again to the spatial domain Ω_t, using this time the Piola transform for space only, equation (4.52):

$$\int_{\Omega_t} \left(\frac{1}{\hat{J}} \left(\hat{J} u_i \right)_{,t} \Big|_{\hat{x}} + \left(u_i (u_j - \hat{u}_j) - \sigma_{ij} \right)_{,j} - f_i \right) d\Omega = 0. \tag{4.63}$$

When localized and expressed in vector notation, the last equations leads to

$$\frac{1}{\hat{J}} \frac{\partial \hat{J} \mathbf{u}}{\partial t} \Big|_{\hat{x}} + \nabla \cdot (\mathbf{u} \otimes (\mathbf{u} - \hat{\mathbf{u}}) - \boldsymbol{\sigma}) - \mathbf{f} = \mathbf{0}, \tag{4.64}$$

where the mesh velocity $\hat{\mathbf{u}}$ now appears. Equation (4.64) is the *conservative form* of the flow equations in the ALE framework [8]. It can be further simplified to the usual formulation, for the incompressible case, by expanding derivatives and applying the identity

$$\frac{\partial \hat{J}}{\partial t} \Big|_{\hat{x}} = \hat{J} \nabla \cdot \hat{\mathbf{u}}, \tag{4.65}$$

resulting in the final *convective form* of the linear momentum balance equations for incompressible flows in the ALE framework, namely:

$$\frac{\partial \mathbf{u}}{\partial t} \Big|_{\hat{x}} + (\nabla \mathbf{u}) (\mathbf{u} - \hat{\mathbf{u}}) - \nabla \cdot \boldsymbol{\sigma} - \mathbf{f} = \mathbf{0}. \tag{4.66}$$

This is the starting point that will be used for the description of the flow on a moving grid that follows the rigid motion of a solid. It is important to ensure that the identity (4.65) be satisfied also at the discrete level, which usually depends on the time discretization scheme [8]. So far, it has been implied that the coordinate frame be the same for all domains (only the domains of definition of the different functions were affected by the above manipulations). The advantage of ALE methods applied to fluid flow equations is that the numerical discretization is simplified as follows [8]: given the time-dependent solution defined on the reference domain $\hat{\Omega}$

$$\hat{u}(\hat{x}, t) = \sum_A u_A(t) \hat{N}_A(\hat{x}), \tag{4.67}$$

where $\hat{N}_A$ are fixed basis functions of a standard finite element discretization, associated to the mesh nodes A. In this domain, the referential time derivative can be immediately computed

$$\frac{\partial \hat{u}(\hat{x}, t)}{\partial t} \Big|_{\hat{x}} = \sum \frac{du_A(t)}{dt} \hat{N}_A(\hat{x}). \tag{4.68}$$

The basis functions can then be pushed forward to the spatial domain

$$N_A(x, t) = \hat{N}_A(\phi^{-1}(x, t)), \tag{4.69}$$

where ϕ now is the discrete ALE mapping

$$\phi(\hat{x}, t) = \sum_A (\hat{x}_A + \hat{y}_A(t)) \hat{N}_A(\hat{x}), \tag{4.70}$$

with $\hat{y}_A(t)$ the displacement of the nodes over time. The discrete solution on the spatial domain is defined as

$$u(x,t) = \hat{u}(\phi^{-1}(x,t),t) = \sum_A u_A(t)\hat{N}_A(\phi^{-1}(x,t)) = \sum_A u_A(t)N_A(x,t). \tag{4.71}$$

Then the spatial and temporal derivative will be given by

$$\frac{\partial u(x,t)}{\partial x} = \sum_A u_A(t)\frac{\partial N_A(x,t)}{\partial x}, \tag{4.72}$$

$$\left.\frac{\partial u(x,t)}{\partial t}\right|_{\hat{x}} = \left.\frac{\partial \hat{u}}{\partial t}\right|_{\hat{x}} (\phi^{-1}(x,t),t) = \sum_A \frac{du_A(t)}{dt}\hat{N}_A(\phi^{-1}(x,t)) = \sum_A \frac{du_A(t)}{dt}N_A(x,t). \tag{4.73}$$

From these equations it can be seen that the spatial derivatives only affect the basis functions while the time derivative acts only on the solution coefficients. Therefore, in this ALE formulation the referential time derivative of the solution defined in the spatial domain is calculated by simply taking the time derivative of the coefficients. This makes it straightforward to implement a semi-discrete discretization approach for problems defined on moving domains. Now we can write the conservation law in integral form [23]:

$$\left.\frac{\partial}{\partial t}\right|_\chi \int_{V_t} \mathbf{u} dV + \int_{S_t} \mathbf{u}\hat{\mathbf{u}}\cdot\mathbf{n} dS = \int_{V_t} (\nu\Delta\mathbf{u} - \nabla p)\, dV, \tag{4.74}$$

where the time derivative on the left is taken at a fixed grid point. These equations are written in the laboratory frame, or spatial domain, that is, the grid points of the mesh are seen as moving and a suitable mesh motion technique should be employed. In order to write the equations in ALE form, the map ϕ must map the arbitrary fluid reference domain to the current spatial configuration at all times with sufficient smoothness, so that all manipulations are justified. In FSI applications, the motion of the fluid domain is given by the condition that the motion of the interface with a solid be followed exactly over time. Therefore, if e.g. $\mathbf{y}$ is the solid displacement field, and, as it's customary, the referential fluid domain fits the solid one, at the interface Γ_{FSI} the ALE map will respect the boundary condition

$$\hat{\mathbf{d}} = \mathbf{y} \qquad \text{on} \qquad \Gamma_{FSI}, \tag{4.75}$$

where in this case the mesh displacement $\hat{\mathbf{u}}$ is given, which is equivalent to specifying the mesh velocity up to an initial condition. The behaviour of the mapping on the rest of the fluid domain can be arbitrary, provided it satisfies the smoothness conditions. A common choice is solving a problem of linear elasticity where the unknowns are the displacements of the nodes of the mesh, in weak form:

$$\int_{\Omega_{\tilde{t}}} \boldsymbol{\epsilon}(\mathbf{w})\cdot\mathbf{D}\boldsymbol{\epsilon}\left(\hat{\mathbf{d}}(t) - \hat{\mathbf{d}}(\tilde{t})\right) d\Omega = 0, \tag{4.76}$$

where a test function from a suitable space $\mathbf{w}$ appears, $\boldsymbol{\epsilon}$ is the strain associated with $\mathbf{w}$ and $\mathbf{D}$ is the elasticity tensor. Here, the boundary value problem is discretized on $\Omega_{\tilde{t}}$, which is the fluid domain at the previous time step. In this case, however, the motion of the solid is already known to be rigid, therefore if one wishes to have a body fitted mesh for an unbounded domain, the fluid domain will need to follow a rigid rotation. At the beginning of each fluid time step, the actual rotation vector $\boldsymbol{\Omega}$ is given, thus the required mesh motion is already known and there is no need to solve an additional problem of the kind in equation (4.76). Indeed, the mesh does not need to be actually moved: if the rotation is known, instead of moving the points one can rotate the axes of the coordinate frame, achieving the same change of the

coordinates of each point. This also yields the advantage that if the wake region is restricted in a certain zone of space (for example if the motion is non-vertical but periodic around a certain axis), then the mesh can be refined only around this region. Another advantage is that the equations for the fluid will be solved in the same rotating system of coordinates of the solid, since usually for rigid body motion the ODEs of the solid are solved in a system of coordinates that follow the body rotations, so that the components of the added mass and moment of inertia tensors stay constant over time. In the ALE equations however the partial time derivative of the velocity is intended for a fixed mesh point. Once discretized, the difference between the velocities at the same mesh point in two consecutive time steps. These velocity vectors will be referred to two different coordinate frames (rotated with respect to each other) and thus an additional correction term appears. More specifically, if the frame is rotated by an orthogonal, time-dependent rotation matrix $Q(t)$, to write the difference between two vectors in components, these can be referred to the same fixed reference by counter-rotating:

$$\frac{\partial \mathbf{u}}{\partial t} \simeq \frac{Q(t+\Delta t)^T \mathbf{u}(t+\Delta t) - Q(t)^T \mathbf{u}(t)}{\Delta t} \to \dot{Q}^T \mathbf{u} - Q^T \dot{\mathbf{u}} \tag{4.77}$$

which leads, going back to the current rotated coordinate frame, to the expression

$$\dot{\mathbf{u}} + Q\dot{Q}^T \mathbf{u}. \tag{4.78}$$

If the rotation matrix is of the form

$$Q(t) = \begin{pmatrix} \cos(\Omega t) & \sin(\Omega t) & 0 \\ -\sin(\Omega t) & \cos(\Omega t) & 0 \\ 0 & 0 & 1 \end{pmatrix}, \tag{4.79}$$

which is a rotation about the z axis, then

$$Q\dot{Q}^T(t) = \begin{pmatrix} 0 & -\Omega & 0 \\ \Omega & 0 & 0 \\ 0 & 0 & 0 \end{pmatrix}, \tag{4.80}$$

which corresponds to the axial vector

$$\mathbf{\Omega} = \begin{pmatrix} 0 \\ 0 \\ \Omega \end{pmatrix}. \tag{4.81}$$

If we call the velocity in the inertial frame of reference with fixed coordinate axes $\tilde{\mathbf{u}}$, and the velocity with respect to the rotating coordinate axes $\mathbf{u}$, then the components of the two vectors are related by a rotation

$$\mathbf{u} = Q(t)\tilde{\mathbf{u}} \tag{4.82}$$

but the vector itself will of course be the same. In local form, the final set of equations to be solved will then be:

$$\frac{\partial \mathbf{u}}{\partial t} + \mathbf{\Omega} \times \mathbf{u} + (\nabla \mathbf{u})(\mathbf{u} - \hat{\mathbf{u}}) = \nu \Delta \mathbf{u} - \nabla p, \tag{4.83}$$

$$\nabla \cdot \mathbf{u} = 0, \tag{4.84}$$

with $\hat{\mathbf{u}} = \mathbf{U} + \boldsymbol{\Omega} \times \mathbf{r}$ the rigid motion of the solid, and with the boundary conditions

$$\mathbf{u} = \mathbf{U} + \boldsymbol{\Omega} \times \mathbf{r}, \qquad \text{on solid surface,} \tag{4.85}$$

$$\mathbf{u} \to \mathbf{0}, \qquad \text{for } \|\mathbf{r}\| \to \infty \tag{4.86}$$

where the coordinate frame is the rotating one. Now since $\mathbf{U}$ and $\boldsymbol{\Omega}$ are kept constant over each time-step of the fluid when solving the Navier-Stokes equations, it is necessary to identify which added mass contributions are missing when integrating the pressure resulting from the solution of equations (4.83,4.84). In [46], the authors consider the example of a sphere rotating and translating at the same time, with velocity and rotation rate vectors, $\mathbf{U}$ and $\boldsymbol{\Omega}$, that are not parallel. The corresponding irrotational flow solution is known to be:

$$\mathbf{u} = -\frac{1}{2}\left(\frac{R^3}{r^3}\right)\mathbf{U} \cdot \left(\mathbb{I} - 3\frac{\mathbf{rr}}{r^2}\right). \tag{4.87}$$

Substituting into equations (4.83,4.84) and integrating the pressure field due to the advective contribution over the surface of the sphere yields

$$\mathbf{F} = -\rho\left(\frac{\mathcal{V}}{2}\right)\boldsymbol{\Omega} \times \mathbf{U}, \tag{4.88}$$

where $\mathcal{V}$ is the volume of the sphere. Now, noticing that for the sphere the added mass tensor is $\mathbb{A} = \rho\,(\mathcal{V}/2)\,\mathbb{I}$, it can be concluded that the added-mass contributions which are not obtained by solving equations (4.83,4.84) are solely those generated by the time derivatives $\frac{d\mathbf{U}}{dt}$ and $\frac{d\boldsymbol{\Omega}}{dt}$ of the body motion, since the two quantities are kept constant over the time step when solving the flow system. All other added mass contribution are reproduced by the solution of the Navier-Stokes equations in this manner. This missing term will need to be accounted for when solving the equations of the evolution of the rigid body motion, while the terms already accounted for cancel out. The equations for the solid will thus become:

$$(m\mathbb{I} + \mathbb{A})\,\frac{d\mathbf{U}}{dt} + m\boldsymbol{\Omega} \times \mathbf{U} = \mathbf{F}_{QS}(t) + (m - \rho\mathcal{V})\,\mathbf{g}, \tag{4.89}$$

$$(\mathbb{J} + \mathbb{D})\,\frac{d\boldsymbol{\Omega}}{dt} + \boldsymbol{\Omega} \times (\mathbb{J}\boldsymbol{\Omega}) = \boldsymbol{\Gamma}_{QS}(t), \tag{4.90}$$

where the contribution of gravity has been included, and $\mathbf{F}_{QS}(t)$, $\boldsymbol{\Gamma}_{QS}(t)$ are respectively the *quasi-steady* force and torque acting on the body due to the fluid. Here, *quasi-steady* indicates that they do not include the reaction of the fluid due to sudden variations in time of the velocity of the body, since they are calculated for a solid motion frozen in time, as discussed above. It does not mean, however, that their values are constant or almost constant over time. The tensors $\mathbb{A}$ and $\mathbb{D}$ account for the added mass effects and coincide with those determined by means of irrotational flow theory.

4.3.2 Navier-Stokes system solution strategy - Rotational Pressure Correction scheme

The Navier-Stokes equations can be solved with a variety of approaches: here we choose the popular splitting approach, which is suitable for simulations of flows with a high number of degrees of freedom, as the matrices resulting from discretization are such that very fast, scalable and efficient solvers and preconditioners are available. We follow the method outlined by Guermond et al. [28], which we briefly recall, for the case when a BDF2 scheme is used

for discretization of the time derivative. First, a velocity problem is solved:

$$\frac{3\tilde{\mathbf{u}}^{n+1} - 4\mathbf{u}^n + \mathbf{u}^{n-1}}{2\Delta t} + \nu\Delta\tilde{\mathbf{u}}^n + \left(2\mathbf{u}^{n-1} - \mathbf{u}^{n-2}\right)\cdot\nabla\tilde{\mathbf{u}}^{n+1} + \nabla p^n = \mathbf{0}, \tag{4.91}$$

$$\tilde{\mathbf{u}}^{n+1}\cdot\mathbf{n} = \overline{\mathbf{u}}^{n+1} \quad on\ \Gamma_D, \qquad \left(p^n - \nu\frac{\partial\tilde{\mathbf{u}}^{n+1}}{\partial n}\right) = 0 \quad on\ \Gamma_N, \tag{4.92}$$

where $\tilde{\mathbf{u}}^{n+1}$ is the tentative velocity solution, which is not divergence free. The pressure value used in this step is the one at the previous time-step, thus we employ an incremental scheme. The convective term is also linearized by using an extrapolated value for the convective velocity. The solution of the first step is then corrected to account for the incompressibility constraint, by solving a problem for the pressure value at the new time-step:

$$\frac{3\mathbf{u}^{n+1} - 3\tilde{\mathbf{u}}^{n+1}}{2\Delta t} + \nabla\phi^{n+1} = \mathbf{0}, \tag{4.93}$$

$$\nabla\cdot\mathbf{u}^{n+1} = 0, \tag{4.94}$$

$$\mathbf{u}^{n+1}\cdot\mathbf{n} = \overline{\mathbf{u}}^{n+1}\cdot\mathbf{n}, \quad on\ \Gamma_D, \qquad \phi^{n+1} = 0 \quad on\ \Gamma_N, \tag{4.95}$$

where the unknown here is a modified pressure variation

$$\phi^{n+1} = p^{n+1} - p^n + \chi\nu\nabla\cdot\tilde{\mathbf{u}}^n, \tag{4.96}$$

and the constant χ depends on the dimension of the problem [28]. More specifically, $\chi < \frac{2}{d}$, and d is either 2 or 3. The factor is simply 1 if there are no open boundaries. For values $\chi \neq 0$ the scheme is known as rotational pressure correction scheme. It is known that this formulation has better accuracy for the pressure with respect to the classical splitting approach, particularly regarding the pressure behaviour at the boundaries. To see this, and considering for simplicity a situation where all boundaries of the domain are fixed, one then takes equation (4.93) at a fixed boundary for $\chi = 0$, from which it follows that:

$$\nabla p^{n+1}\cdot\mathbf{n}_\Gamma = \nabla p^n\cdot\mathbf{n}_\Gamma = \cdots = \nabla p^0\cdot\mathbf{n}_\Gamma. \tag{4.97}$$

Therefore, we note the presence of a numerical boundary layer that deteriorates the accuracy of the solution [29]. If instead we take $\chi = 1$ (again, assuming for simplicity that there are no open or moving boundaries), taking the sum of equations (4.91) and (4.93) (noticing also that, from equation 4.93 it also follows that $\nabla\times\nabla\times\tilde{\mathbf{u}}^{n+1} = \nabla\times\nabla\times\mathbf{u}^{n+1}$) now yields:

$$\frac{3\mathbf{u}^{n+1} - 4\mathbf{u}^n + \mathbf{u}^{n-1}}{2\Delta t} + \nu\nabla\times\nabla\times\mathbf{u}^{n+1} + \nabla p^n = \mathbf{0}, \tag{4.98}$$

$$\mathbf{u}^{n+1}\cdot\mathbf{n} = 0 \quad on\ \Gamma, \qquad \nabla\cdot\mathbf{u}^{n+1} = 0, \tag{4.99}$$

where for simplicity the convective term was dropped. This formulation is the reason why the method is denoted as rotational pressure correction. We see now that, at the boundaries it holds:

$$\nabla p^{n+1}\cdot\mathbf{n}_\Gamma = -\nu\nabla\times\nabla\times\mathbf{u}^{n+1}\cdot\mathbf{n}_\Gamma, \tag{4.100}$$

which, unlike (4.97), is now a consistent pressure boundary condition.

A weak formulation for the pressure can then be obtained. Multiplying with a test function and integrating by parts yields the following pressure problem:

$$\left(\nabla\phi^{n+1}, \nabla q\right) = -\left(\nabla\cdot\frac{3\tilde{\mathbf{u}}^{n+1}}{2\Delta t}, q\right) + \int_{\Gamma_D}\frac{\partial\phi^{n+1}}{\partial n}, \tag{4.101}$$

where the test function q is in the space H^1, and has to satisfy a zero Neumann boundary

condition involving accelerations at the boundaries where a Dirichlet condition is specified for the velocity:

$$\left.\frac{\partial \phi^{n+1}}{\partial n}\right|_{\Gamma_D} = 0, \qquad \phi^{n+1} = 0 \quad on\ \Gamma_N. \tag{4.102}$$

All of these problems involve a second order differencing scheme. At the first time step, when only the information at time $n = 0$ is available, the backward Euler finite difference is used instead. In addition to the standard time stepping procedure, it can be useful to sub-iterate the solution at each time-step to ensure incompressibility, thus reducing the error due to the splitting. For iterations after the first one, the scheme is slightly modified, the pressure problem being now

$$\left(\nabla \phi^{i+1}, \nabla q\right) = \left(\frac{3\tilde{\mathbf{u}}^i}{2\Delta t}, \nabla q\right), \tag{4.103}$$

where the modified pressure variation now is

$$\phi^{i+1} = p^{i+1} - p^i + \chi \nu \nabla \cdot \tilde{\mathbf{u}}^i, \tag{4.104}$$

and has to satisfy the following boundary conditions at the boundary:

$$\frac{\partial \phi^{i+1}}{\partial n} \quad on\ \Gamma_D = 0, \qquad \phi^{i+1} = 0 \quad on\ \Gamma_N. \tag{4.105}$$

4.3.3 Fluid-rigid body system solution strategy

The flow equations are coupled with the system of ODEs of the rigid body motion:

$$\rho_r V \left(\frac{d\mathbf{U}}{dt} + \boldsymbol{\Omega} \times \mathbf{U}\right) = \mathbf{F}_{fl} + (\rho_r - 1) V \mathbf{g}, \tag{4.106}$$

$$\mathbf{I}\frac{d\boldsymbol{\Omega}}{dt} + \boldsymbol{\Omega} \times (\mathbf{I}\boldsymbol{\Omega}) = \mathbf{M}_{fl}, \tag{4.107}$$

where equations are normalized by the density of the fluid, and thus the density ρ_r is the ratio $\frac{\rho_s}{\rho_f}$, and the same dimensionless density is used in the calculation of the components of the inertia tensor $\mathbf{I}$. The coupling algorithm is made following the approach presented by [36] and used in [14]: the equations (4.83,4.84) are discretized with a classic splitting approach, then the resulting linearized system is coupled with the solid motion implicitly. The non-linear convection term in the Navier-Stokes equations is linearized with a second order Adams–Bashforth discretization, yielding an unsteady Stokes linear problem:

$$\frac{1}{2\Delta t}\begin{bmatrix} 3\mathbf{u}_0^{n+1} - 4\mathbf{u}^n - \mathbf{u}^{n-1} \\ 0 \end{bmatrix} = \begin{bmatrix} \mathbf{V} & \mathbf{D} \\ \mathbf{D}^T & \mathbf{0} \end{bmatrix} \begin{bmatrix} \mathbf{u}_0^{n+1} \\ \mathbf{p}_0^{n+1} \end{bmatrix} + \begin{bmatrix} \mathbf{H}\mathbf{Z}^n \\ \mathbf{0} \end{bmatrix}, \tag{4.108}$$

where the unknowns are velocity and pressure at the new time step $n + 1$, but with old time-step boundary conditions $\mathbf{Z}^n$, that correspond to the velocities of the solid body already known (hence the subscript $_0$ for the velocity). The flow equations are thus solved assuming at first that the body motion doesn't change over the time-step. The term $\mathbf{H}$ therefore represents the action of boundary conditions, while $\mathbf{V} = \mathbf{L} + \mathbf{N}$ is the result from the linearization of the non-linear term, and the discretization of the viscous term. The remaining terms are obtained as usual from discretization of the incompressibility constraint. Once the solution is calculated, it has to be corrected in order to take into account the effect of the change in boundary conditions, that is, the change of the velocities of the solid during the time-step.

Namely, we are implicitly decomposing the velocity and pressure at the new time-step as

$$\mathbf{u}^{n+1} = \mathbf{u}_0^{n+1} + \Delta\mathbf{u}^{n+1}, \tag{4.109}$$

$$p^{n+1} = p_0^{n+1} + \Delta p^{n+1}, \tag{4.110}$$

thanks to the linearity of the dependence of the solution of problem (4.108) on the boundary conditions. The correction for the flow, Δu^{n+1} and Δp^{n+1}, depends on the evolution of the solid motion over the time step:

$$\mathbf{X} = \begin{pmatrix} \mathbf{U}^{n+1} - \mathbf{U}^n \\ \boldsymbol{\Omega}^{n+1} - \boldsymbol{\Omega}^n \end{pmatrix}, \tag{4.111}$$

which in turn is determined by the equations for the solid motion, that is from the resistance of the fluid to instantaneous velocity variations of the body. Thus, a system of coupled ODEs has to be solved:

$$\frac{1}{2\Delta t}\begin{bmatrix} 3\Delta\mathbf{u}^{n+1} \\ 0 \end{bmatrix} = \begin{bmatrix} \mathbf{V} & \mathbf{D} \\ \mathbf{D}^T & \mathbf{0} \end{bmatrix}\begin{bmatrix} \Delta\mathbf{u}^{n+1} \\ \Delta p^{n+1} \end{bmatrix} + \begin{bmatrix} \mathbf{HX} \\ \mathbf{0} \end{bmatrix}, \tag{4.112}$$

$$\mathbb{M}\left(\dot{\mathbf{X}} + \mathbb{N}\left(\mathbf{Z}^n + \mathbf{X}\right)\right) = \mathbb{B}\Delta\mathbf{U}^{n+1} + \mathbb{C}\Delta\mathbf{P}^{n+1} + \mathbf{R}, \tag{4.113}$$

where the matrices $\mathbb{B}$ and $\mathbb{C}$ represent the response of the fluid to velocity variations of the solid, $\mathbf{R}$ can be interpreted as a residual and is given by gravity and the forces and torques acting on the body, calculated by integrating the fluid stresses for the intermediate flow solution, obtained from solving system (4.108). The matrix $\mathbb{M}$ and $\mathbb{N}$ instead are a compact representation of the inertia coefficients and of the other terms of the equations in (4.106), respectively.

$$\mathbb{M} = \begin{bmatrix} \begin{bmatrix} \rho_r V & 0 & 0 \\ 0 & \rho_r V & 0 \\ 0 & 0 & \rho_r V \end{bmatrix} & \begin{bmatrix} \mathbf{0} \end{bmatrix} \\ \begin{bmatrix} \mathbf{0} \end{bmatrix} & \begin{bmatrix} \mathbf{I}_x & 0 & 0 \\ 0 & \mathbf{I}_y & 0 \\ 0 & 0 & \mathbf{I}_z \end{bmatrix} \end{bmatrix}, \tag{4.114}$$

$$\mathbb{N} = \begin{bmatrix} \begin{bmatrix} 0 & -\omega_z & \omega_y \\ \omega_z & 0 & -\omega_x \\ -\omega_y & \omega_x & 0 \end{bmatrix} & \begin{bmatrix} \mathbf{0} \end{bmatrix} \\ \begin{bmatrix} \mathbf{0} \end{bmatrix} & \begin{bmatrix} 0 & -\mathbf{I}_y\omega_z & \mathbf{I}_z\omega_y \\ \mathbf{I}_x\omega_z & 0 & -\mathbf{I}_z\omega_x \\ -\mathbf{I}_x\omega_y & \mathbf{I}_y\omega_x & 0 \end{bmatrix} \end{bmatrix} \tag{4.115}$$

The subsystem (4.112) gives a linear dependence of the corrections of the flow on $\mathbf{X}$, and, by equations (4.113), the body motion has a linear dependence on these corrections. Therefore, we can substitute in equation (4.113) $\Delta\mathbf{U}^{n+1} = \mathbb{S}\mathbf{X}$ and $\Delta P^{n+1} = \mathbb{T}\mathbf{X}$, and denoting by $\mathbb{A}$ the 6 by 6 matrix $\mathbb{B}\mathbb{S} + \mathbb{C}\mathbb{T}$, the following problem for $\mathbf{X}$ can be formulated:

$$\dot{\mathbf{X}} = \mathbb{M}^{-1}\left[-\mathbb{N}\left(\mathbf{Z}^n + \mathbf{X}\right) + \mathbb{A}\mathbf{X} + \mathbf{R}\right]. \tag{4.116}$$

Again, thanks to the linear dependence on the boundary conditions, a good approximation of the matrix $\mathbb{A}$ can be calculated just once before the start of the actual simulation, provided that the time-step and mesh do not change (in which case the matrix needs to be calculated again). Its six columns are the components of forces and torques that the fluid exerts on the solid in response to an unitary instantaneous variation of translational or rotational velocity

in one of the six degrees of freedom, with a surrounding fluid initially at rest. It therefore represents an approximation (given that the time-step is finite) of the added mass response of the fluid, enhanced by viscous contributions. As expected, it depends only on the geometry of the body. Once the variation of the body motion $\mathbf{X}$ has been calculated, the unsteady Stokes system (4.112) can be solved to obtain the correction to the flow conditions. This information of course is also known by combining linearly the fields of the solutions to the 6 problems solved to determine the columns of $\mathbb{A}$, therefore it's not necessary to actually solve the PDEs of the unsteady Stokes problem (4.112).

As the system of coordinates is rotating, the gravity vector becomes time dependent and has to be updated at every time step. When the values of rotational velocities of the body are known at the new time step, the update can be performed by advancing the following ODE in time:

$$\dot{\mathbf{g}} = -\boldsymbol{\omega}^{n+1} \times \mathbf{g} \tag{4.117}$$

The time derivatives in the ODEs have not been specified as finite differences so far. The ODEs are automatically advanced in time using high order integration tools provided by standard numerical libraries. These tools usually employ an adaptive time stepping and can also change the discretization method based on the stiffness of the particular problem at hand.

4.3.4 Finite element implementation

The solver is implemented within the framework of the open source Navier-Stokes solver *Oasis* [45], which in turn is based on the *FEniCS* finite element library. The Navier-Stokes equations are solved with a fractional step algorithm described above, starting with problem (4.91). The equations are solved with a segregated approach, each component separately, in order to lower the computational effort. The viscous term is treated implicitly in time, to ensure stability, while for the non-linear convection term a second order extrapolation is used for the convecting velocity, $\mathbf{u}_{\text{conv}} = 2\mathbf{u}^{n-1} - \mathbf{u}^{n-2}$ (from which the ALE velocity due to rigid body motion is subtracted), while the convected velocity is treated again implicitly to avoid too strict time step limitations due to the CFL number condition. Discretization in space is done with standard $\mathbb{P}2/\mathbb{P}1$ finite elements, stable for the approximation of incompressible flow problems. Once integration by parts and finite element assembly is done, the resulting algebraic system of equations for the generic *k-th* component of equations (4.91) reads:

$$\left(\frac{3M_{F,ij}}{2\Delta t} + C_{F,ij} + \nu K_{F,ij}\right) \tilde{U}_{F,j}^{k,n+1} = \mathcal{R}_i^{k,n+1/2}, \tag{4.118}$$

where $\tilde{U}_F$ is the vector of coefficients of the velocity of the fluid, the matrices M, C, K result from the discretization of the mass, convection and diffusion terms, respectively, and the right-hand side vector results from discretization of the source terms and the terms related to pressure and open boundaries, where a Neumann condition is specified. More in detail, we introduce with φ_j a set of functions forming a discrete basis, that have the properties which hold for standard Lagrange finite elements, and such that the discrete vector space that they span is H^1 conformal [25]. For each *k-th* component of the velocity it holds:

$$u_k = \sum_{j=1}^{N_u} U_j^k \varphi_j, \tag{4.119}$$

then the matrices are obtained by the assembly operations

$$M_{ij} = \int_\Omega \varphi_j \varphi_i dx, \qquad K_{ij} = \int_\Omega \nabla\varphi_j \cdot \nabla\varphi_i dx, \qquad C_{ij} = \int_\Omega \left(2\mathbf{u}^{n-1} - \mathbf{u}^{n-2}\right) \cdot \nabla\varphi_j \varphi_i dx. \tag{4.120}$$

The right-hand side vector instead is obtained by

$$\mathcal{R}_i^{n+1/2} = \frac{4M_{ij}}{2\Delta t} U_j^{n-1} - \frac{M_{ij}}{2\Delta t} U_j^{n-2} - d\mathcal{P}_{ij}^k P_j^n + N^{k,n}, \tag{4.121}$$

where the last two terms are the pressure gradient at old time n, projected [45] on the velocity discrete space (having denoted the pressure space basis functions as $\hat{\varphi}_j$):

$$d\mathcal{P}_{ij}^k = \int_\Omega \nabla_k p^n \varphi_i dx = \sum_{j=1}^{Np} \left(\int_\Omega \nabla_k \hat{\varphi}_j \varphi_i dx \right), \tag{4.122}$$

and $N^{k,n}$ is the vector resulting from the discretization of Neumann boundary conditions. It is calculated according to (4.92):

$$N_j^{k,n} = \nu \int_{\Gamma_N} \frac{\partial u_k}{\partial n} \varphi_j = \int_{\Gamma_N} p^n n_k \varphi_j. \tag{4.123}$$

In the Navier-Stokes equations in the form (4.83,4.84), an additional term due to rotation $\boldsymbol{\Omega} \times \mathbf{u}$ is present. It is linear, since the vector $\boldsymbol{\Omega}$ is constant during the Navier-Stokes time-step advancement. However, treating this term implicitly would result in the coupling of the three components of the Navier-Stokes equations, leading to less efficient matrix reuse and higher computational costs, due to the worse conditioning of the algebraic systems to be solved. To preserve the efficiency of the code, the term is treated explicitly and updated at each sub-iteration of the Navier-Stokes solution process. Once the velocity tentative solution $\tilde{\mathbf{u}}^{n+1}$ has been calculated, the pressure problem is solved. In the discrete version the Laplace problem reads

$$\hat{K}_{ij} \Phi_j^{n+1} = -\frac{3}{2\Delta t} \int_\Omega \nabla \cdot \tilde{\mathbf{u}}^{n+1} \hat{\varphi}_i dx \tag{4.124}$$

where $\hat{K}$ is the stiffness matrix for the pressure space, and the solution vector holds the values of the pressure correction with respect to the previous presssure extrapolation. The right-hand side involving the divergence can be further developed in terms of assembly operations [45], where again basis functions from both the velocity and pressure spaces appear:

$$\int_\Omega \frac{3\nabla \cdot \tilde{\mathbf{u}}^{n+1}}{2\Delta t} \hat{\varphi}_i dx = \frac{3}{2\Delta t} \sum_{k=1}^{d} \left(\sum_{j=1}^{N_u} \int_\Omega \nabla_k \varphi_j \hat{\varphi}_i \mathrm{d}x \, \tilde{U}_j^{k,n+1} \right) = \frac{3}{2\Delta t} \sum_{k=1}^{d} d\mathcal{U}_{ij}^k \tilde{U}^{k,n+1}. \tag{4.125}$$

The solution of this second algebraic system yields the modified pressure variation. To complete the time step (or the iteration, if the solution scheme is sub-iterated to ensure that the incompressibility constraint is respected with higher precision), the pressure itself is updated for the next time step, and the velocity is corrected to account for the incompressibility:

$$\frac{3M_{ij}}{2\Delta t} U_j^{n+1} = \frac{3M_{ij}}{2\Delta t} \tilde{U}_j^{n+1} - d\mathcal{P}_{ij}^k \Phi_j^{n+1}, \tag{4.126}$$

$$\hat{M}_{ij} P_j^{n+1} = \hat{M}_{ij} \Phi_j^{n+1} + \hat{M}_{ij} P_j^n - \chi \nu \mathcal{D}_i^{n+1}, \tag{4.127}$$

where we recall the definition of the matrices $d\mathcal{P}^k_{ij}$ and $d\mathcal{U}^k_{ij}$ from above, and the term at the right-hand side of the last equation is obtained from the operation:

$$\mathcal{D}^{n+1}_i = \sum_{k=1}^{d} d\mathcal{U}^k_{ij} \tilde{U}^{n+1}_j. \tag{4.128}$$

At the first time step of the simulation, the second order formulas cannot be used. The time discretization is simply substituted with Euler Backward finite differences, and from the following time step the second order scheme is employed. The systems that are modified as a result are briefly reported here

$$\mathcal{R}^{k,1/2}_i = \left(\frac{M_{F,ij}}{\Delta t} + C_{F,ij} + \nu K_{F,ij} \right) \tilde{U}^{k,1}_{F,j}, \tag{4.129}$$

$$\mathcal{R}^{1/2}_i = \frac{M_{ij}}{\Delta t} U^0_j - d\mathcal{P}^k_{ij} P^0_j + N^{k,0}, \tag{4.130}$$

$$\hat{K}_{ij} \Phi^1_j = -\frac{1}{\Delta t} \int_\Omega \nabla \cdot \tilde{\mathbf{u}}^1 \hat{\varphi}_i dx, \tag{4.131}$$

$$\frac{M_{ij}}{\Delta t} U^1_j = \frac{M_{ij}}{\Delta t} \tilde{U}^1_j - d\mathcal{P}^k_{ij} \Phi^1_j. \tag{4.132}$$

$$\tag{4.133}$$

It's important to note that, if the domain is fixed, the matrices are assembled once at the beginning of the simulation, except for the convective term, which has to be reassembled at the beginning of each time step. If, on the other hand, the domain is moving, all the matrices become time dependent and in general will need to be reassembled at each time step. In the numerical studies in the following chapters, this will be avoided since a rotation of the coordinate axes will suffice (see the derivation of the equations above), since the mesh motions will always be rigid. A standard fractional scheme for Navier-Stokes equations is already implemented in an optimized way in the *Oasis* library. The solver is modified by adding the ALE convection terms and implementing the steps above for the splitting scheme, including the correction provided by the scheme being of the more accurate rotational variant. Furthermore, the presence of the coupling with a solid requires introducing further modifications. In particular, the solutions of the solid equations, as well as the unsteady Stokes correction step, equations (4.112,4.113), need to be modified. At the start of simulation, before the first time step, six unsteady Stokes problems are solved, with initial conditions of a fluid at rest, as already described in the previous section. The discrete problem reads:

$$\left(\frac{M_{F,ij}}{\Delta t} + \nu K_{F,ij} \right) \tilde{U}^{k,1}_{F,j} = 0, \tag{4.134}$$

while the pressure step remains the standard one. The boundary condition for velocity on the body is either that of unitary translational velocity in one of the three spatial components, or that of unitary rotational velocity about the same axes. Then, the total forces and torques are integrated on the surface of the body and the result for each of the six problems (after a change of sign) is one of the columns of the matrix $\mathbb{A}$ from equations (4.116). This matrix is then stored and the simulation started: at each time step, the Navier-Stokes equations are solved with the splitting scheme described above. Then, the forces and torques acting on the body due to the fluid are integrated, yielding the residual $\mathbf{R}$ in equation (4.116). This system of ODEs can then be advanced in time for one time step. This is done with the *SciPy* ODE integration routine *solve_ivp*. The ODE system is integrated starting from the solution of the body motion at the previous time, for a total interval of time equal to one time step. The system is integrated at some intermediate times automatically by the adaptive time

stepping of the routine. The integration method selected is a standard high order implicit one. The solution of the ODE system yields the variation of the rigid body motion for the time step $\mathbf{X}$. Once this is known, first the gravity vector is updated integrating the ODE (4.117) for one time-step with the new velocity values. Then, the fluid velocity and pressure are updated to account for the variation in boundary condition, due to the updated body motion. The unsteady Stokes problem (4.112) have therefore to be solved with the increment $\mathbf{X}$ as boundary conditions, yielding the velocity and pressure corrections. Apart from the different boundary conditions, the discretized system is the same as in equation (4.134). This system, however, does not need to actually be solved a second time to calculate the correction of the flow, since this will be given by a linear combination of the fields already obtained when solving for the six columns of the matrix $\mathbb{A}$, thanks to the linearity of the problem. These are stored and reused each time-step. The sum of these corrections with the intermediate velocity and pressure are the starting solution at the following time step. Standard iterative Krylov solvers, from the linear algebra library *PETSc*, are used for solution of the steps of the fractional algorithm for the Navier-Stokes system.

4.3.5 Validation: Falling sphere benchmarks

We now study a falling sphere in an unbounded viscous fluid, with the whole system initially at rest, with the goal of reproducing results of Uhlmann et al. [61], that we use as a benchmark to validate our approach. In this case, the flow is entirely determined by two control parameters: the ratio of solid to fluid density $\frac{\rho_s}{\rho}$ and the Galileo number, which is defined as

$$G = \frac{\sqrt{\left|\frac{\rho_s}{\rho} - 1\right| g d^3}}{\nu}, \tag{4.135}$$

where g is the magnitude of the gravity vector and d the diameter of the sphere. This number substitutes the common Reynolds number since it takes into account the effect of gravity. Furthermore, the final velocity is not known a priori, making a definition of a Reynolds number more involved. Once the flow has been solved for, an average value of the falling velocity can be used to define an average Reynolds number. In general, for lower values of Galileo number this Reynolds number will also be lower and the flow *less unsteady*. Increasing the Galileo number results in a stronger interaction of the object with its wake and possible unsteadiness and/or loss of symmetry. The aim is to reproduce the three cases which are considered by the authors in [61]: a steady vertical fall, for $G = 144$, a steady oblique trajectory, for $G = 178.46$ and a more complex case with a periodic motion over time, with Galileo number $G = 190$. The ratio of densities is fixed at $\frac{\rho_s}{\rho} = 1.5$ in all cases. The simulations are therefore run, from an initial rest condition, until a steady state is reached, or until the periodic pattern is fully developed. Then, velocities of translation and rotation are measured and compared with those reported in the benchmark, non-dimensionalized with the reference scales $u_{ref} = \sqrt{\left|\frac{\rho_s}{\rho} - 1\right| gd}$ and $t_{ref} = \frac{l_{ref}}{u_{ref}} = \frac{d}{u_{ref}}$. The vertical velocity of descent, denoted u_{pV} by Uhlmann et al., is compared with the benchmark data, as well as the horizontal velocities of translation and rotation, defined as, respectively:

$$u_{pH} = \sqrt{u_x^2 + u_y^2}, \tag{4.136}$$

$$\omega_{pH} = \sqrt{\omega_x^2 + \omega_y^2}, \tag{4.137}$$

where the z axis is that aligned with the direction of gravity. For the case $G = 144$, the only relevant quantity, that is vertical velocity over time, is reported in figure 4.2. When

the relative variation in magnitude of the velocity over a time step falls below the specified threshold of 10^{-5} (at which point the simulation is stopped), the result differs by less than 1% from that reported in [61] for the case of a large domain. For Galileo number $G = 178.46$, vertical velocity over time is reported in figure 4.3, while horizontal velocities (translational and rotational, as defined above) are reported in figure 4.4. Again in this case, a steady state is eventually reached, even though the trajectory of the falling sphere will be oblique, due to the interaction with the wake, and the agreement with benchmark results is satisfactory. Instead, when the value of Galileo number is $G = 190$, a periodic state is reached after the initial transient, as expected. In figures 4.5 and 4.6, vertical and horizontal velocities (translational and rotational) are reported, respectively, showing again a satisfactory agreement with the benchmark data. The falling velocity is only marginally affected by the unsteadiness, as usually happens in these conditions, when the unsteadiness is seen by the occurrence of oscillations in the values of the horizontal velocities and rotational rates.

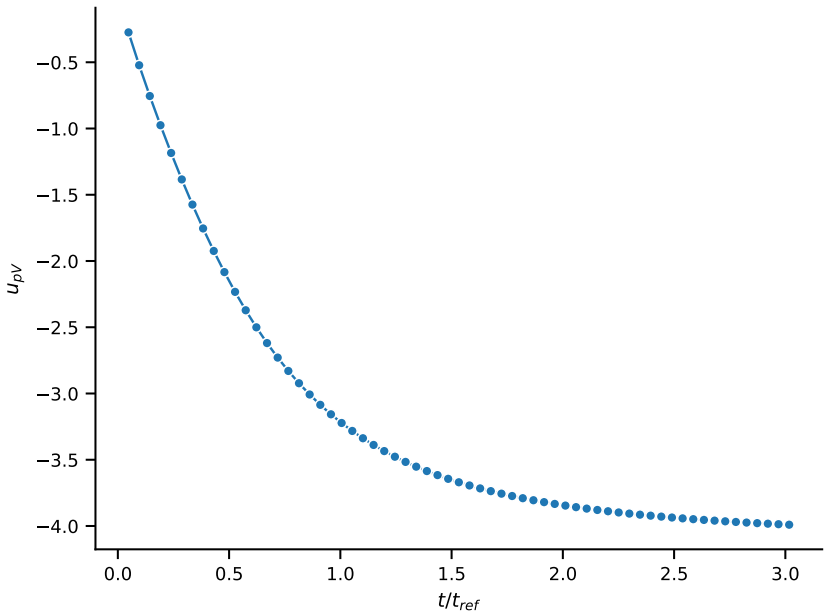

FIGURE 4.2: Vertical velocity over time (both normalized) for the free-falling sphere in the case $G = 144$.

4.4 Experiments

At the end of Purcell's article, experimental data are reported for the free-falling behaviour of the propeller of the swimmer. By letting the tail fall in a very viscous fluid, the resistance coefficients can be easily obtained by measuring the falling velocity, provided that the conditions of the experiments (such as viscosity of the fluid and size of the propeller) are such that the Stokes flow approximation is appropriate. Following the same approach, we perform the experiments to fully determine the behaviour of a prototypical low Reynolds swimmer, which represents the geometry we will use in the numerical study as well. The swimmer will thus consist of a cargo, which we'll denote as head, and a propeller, which we will also denote as tail or helix. The tail has a helical shape, and therefore a certain chirality, while the head has an axi-symmetric shape. Different helices were considered during the study of the swimmer. The two swimmer components were 3D-printed in VisiJet M3 Black material using a Project 3510 HD printer from 3D Systems. The head is hollow, and contains a small motor

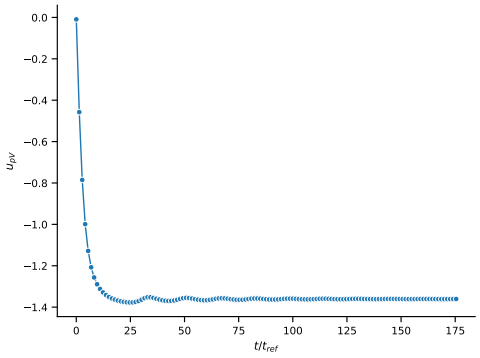

FIGURE 4.3: Vertical velocity over time (both normalized) for the free-falling sphere in the case $G = 178.46$.

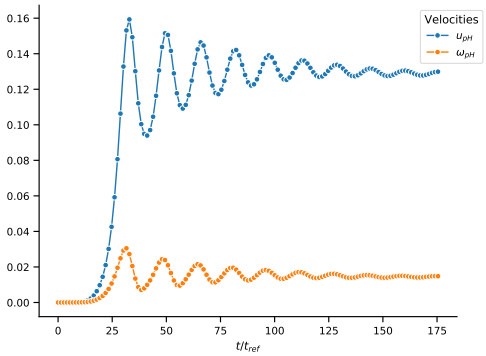

FIGURE 4.4: Horizontal velocity and rotational velocity over time (all normalized) for the free-falling sphere in the case $G = 178.46$.

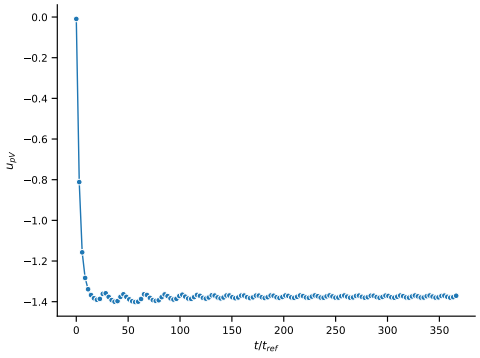

FIGURE 4.5: Vertical velocity over time (both normalized) for the free-falling sphere in the case $G = 190$.

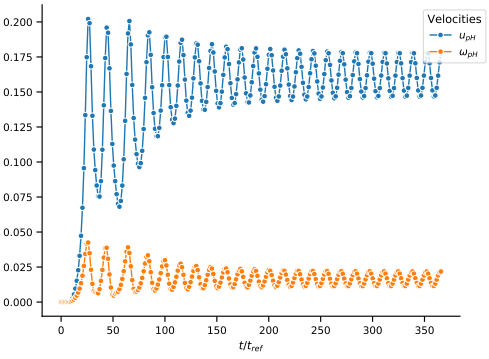

FIGURE 4.6: Horizontal velocity and rotational velocity over time (all normalized) for the free-falling sphere in the case $G = 190$.

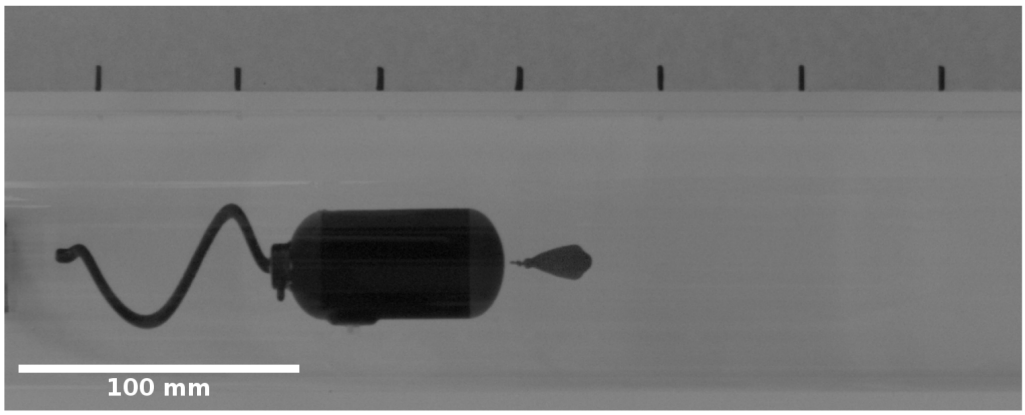

FIGURE 4.7: Single frame acquired by the camera of the swimmer during a fall experiment. Notice the weight added to the head, and the screw at the basis of the propeller. The propeller in this case is a single helix.

that imposes a relative rotation between head and tail when actuated. The motor is a 6 V DC gearmotor from Pololu, model 2366, with a 75:1 gearbox, powered by means of 4 LR44 batteries in series. The remote control of the robot was achieved by means of a custom-made electronic circuit and firmware based on an ATtiny85 8-bit AVR microcontroller (Microchip Technology), reading the serial output of an IR receiver (model TSOP38238 Vishay). The motor could be actuated in order to achieve a rotation of the shaft both in clockwise and counterclockwise direction. Therefore, both head first or tail first swimming velocities could be obtained. In order to reproduce conditions that are close to the Stokes flow approximation, the swimmer and/or the two components separately have to move in a very viscous fluid: in our case, we use glycerol, which has a viscosity about three orders of magnitude greater than that of water. The density value of the fluid was measured directly, resulting in a value of $1.25 g/cm^3$ that will be used for all the following calculations. The precise value of the viscosity was determined by letting some small steel spheres ($2mm$ diameter) fall in the fluid, and measuring their terminal velocity. The result was a dynamic viscosity of $8.2 \cdot 10^{-4} Pa \cdot s$. A cylindrical PMMA tube with inner radius of $48mm$ and height of $100cm$ was filled with the glycerol and all experiments were performed by letting the swimmer or its components swim or fall along the axis of this cylinder. Images of the experiments were acquired at a frame rate of 20 fps by means of a CMOS digital camera (model acA4024-29uc from Basler), equipped with a C-MOUNT objective (model m0824-mpw2 from Computar). The recorded images were then processed with the *ImageJ* software, stacking them in order to generate the relative kymographs, from which velocities, both translational and rotational, could be measured accurately. A snapshot of the swimmer (head+propeller) when inside the PMMA tube is given in figure 4.7.

4.4.1 Free-fall experiments

The material with which the components of the swimmer are 3D-printed is a plastic that is slightly lighter than the surrounding fluid. When needed, before each experiment, the weight of the robot parts was adjusted in order to make them neutrally buoyant in glycerol. Then, an additional weight, the mass and volume of which are known to be $4.8g$ and $0.73cm^3$, respectively, is added and the terminal falling velocity is measured for three different configurations: head and tail separately, and assembled swimmer (motor switched off). This experiment is similar to that of Purcell, and allows to determine the resistance coefficients of the components of the swimmer when the Stokes approximation holds, and hydrodynamic interactions

TABLE 4.1: Results for the fall experiments. The applied force is due to a weight linked to the object (minus the Archimedes force due to the displaced volume of fluid.)

Shape	**Falling velocity [mm/s]**	**Rotation rate [rad/s]**	**Applied force [mN]**
Head	29.6	-	38.187
Helix	51.5	0.931	38.187
Swimmer	21.5	0.125	38.187

between head and tail are neglected. Velocities can be measured accurately from the kymographs generated by stacking the images at each frame acquired by the camera. The rotation rate, when the propeller is present, is measured by choosing a reference feature that can be used to track the revolutions. For example, one such reference feature is a screw at the base of the helix. Results from these experiments are reported in table 4.1.

4.4.2 Motor actuation

When switched on, the motor imposes a relative rotation between head and tail. In this work we will assume, when doing measurements or calculations, that the effect of the actuation is that of imposing a constant relative rotation, thus neglecting the internal dynamics of the motor. Again, before switching on the motor, it is checked that the swimmer be neutrally buoyant when immersed in the fluid. The swimming velocity is measured both when the robot swims head first and tail first along the axis of the tube. Measurements are taken from Kymographs, an example of which is reported in figure 4.8. The two bands represent the descent and the following rise of the actuated swimmer. Results of the measurements are reported in tables 4.2 and 4.3.

TABLE 4.2: Results for the swimming experiments (motor of the robot switched on). The propeller in this case is composed of a single helix.)

Observation	**Direction**	**Swimming velocity [mm/s]**
Measurement 1	Head first	12.5
	Tail first	11.8
Measurement 2	Head first	12.2
	Tail first	10.5

TABLE 4.3: Results for the swimming (motor of the robot switched on) experiments. The propeller in this case is composed of a single helix.)

Observation	**Direction**	**Rot. tail [rad/s]**	**Rot. head [rad/s]**	**Rot. motor [rad/s]**
Measurement 1	Head first	16.3	-7.2	23.5
	Tail first	-15.7	6.8	22.5
Measurement 2	Head first	15.4	-6.7	22.1
	Tail first	-14.6	6.3	20.9

4.4.3 Observations and the double helix propeller

During the experiments, we observe that the swimmer, when actuated by the motor, does not move exactly along a straight line, but has a trajectory that is the superposition of a

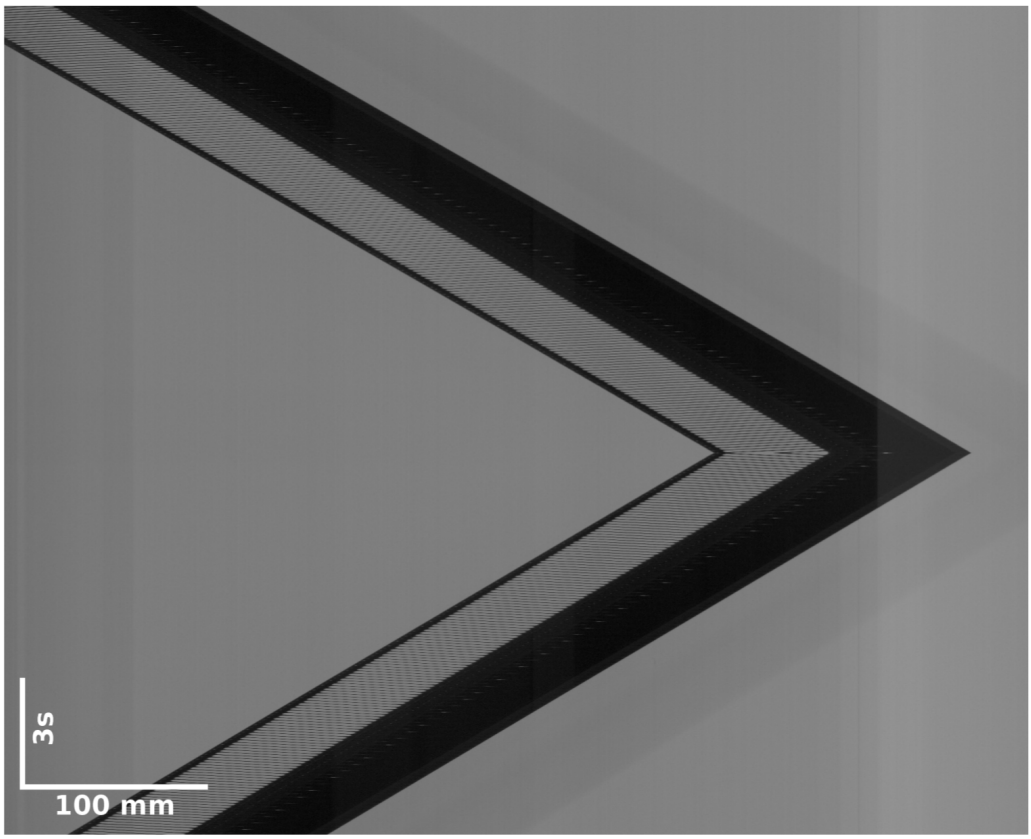

FIGURE 4.8: Kymograph generated by stacking the frames acquired by the camera for the swimming, head-first and tail-first, of the robot when the motor is actuated (double helix).

translation along the vertical and a helical rotation about the axis of the cylinder. This is a small, but visible, effect that we attribute to the finiteness of the tail. Given that the helix does not extend indefinitely, it generates also lateral forces which are not perfectly balanced. This helical deviation from the axis appears different in the two directions of swimming, that is when the robot swims either head first or head first. This is probably the main reason why the velocity is not the same when the swimmer moves in the two directions. In the second measurement dataset in table 4.2, this fore-aft swimming difference is of the order of 15%. To further clarify the causes of this asymmetry, we also introduce a different shape of the propeller: the shape of the helix used will be the same, but a second one is added, rotated by π with respect to the first one. This should intuitively balance the additional lateral thrust derived from the finiteness of the helices. A snapshot of the swimmer when using this second kind of tail is given in figure 4.9. Therefore, measurements are repeated for this different shape of the propeller, and results are reported in tables 4.4 and 4.5. It can be noted that the differences between head-first or tail-first swimming are clearly reduced with respect to the previous case.

4.5 Numerical results

We can now study numerically a prototypical swimmer at low (but possibly finite) Reynolds numbers. The geometry consists of a cargo, an axisymmetric body, connected with a helix. Propulsion of the body can be generated by relative rotation of the helix with respect to the cargo. The same geometry has been used for 3D printing the object so that the predicted behaviour could be tested experimentally. It is of interest to study the behaviour of such an

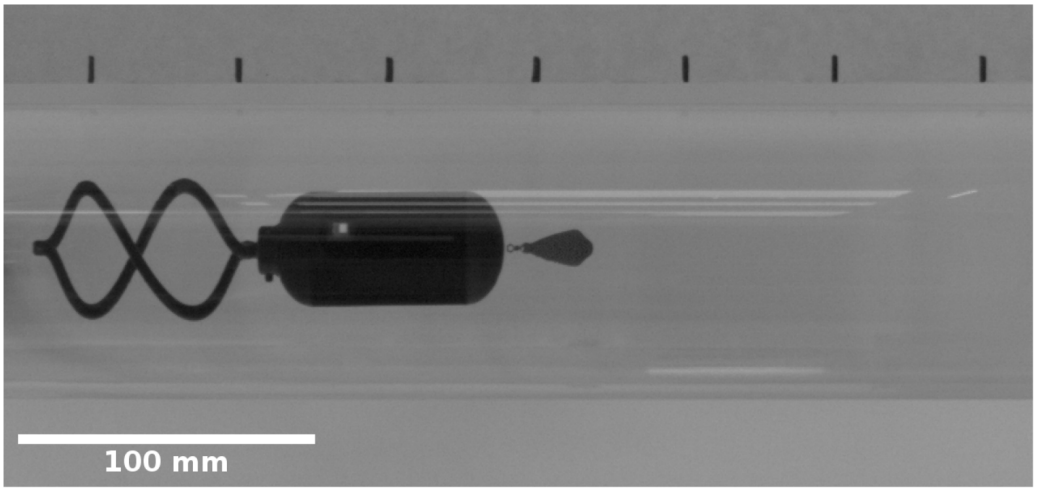

FIGURE 4.9: Single frame acquired by the camera of the swimmer falling due to an added weight. The propeller in this case is a double helix.

TABLE 4.4: Results for the swimming (motor of the robot switched on) experiments. The propeller in this case is composed of two helices.)

Observation	**Direction**	**Swimming velocity [mm/s]**
Measurement 1	Head first	10.1
	Tail first	9.4
Measurement 2	Head first	9.4
	Tail first	9.2

TABLE 4.5: Results for the swimming (motor of the robot switched on) experiments. The propeller in this case is composed of two helices.)

Observation	**Direction**	**Rot. tail [rad/s]**	**Rot. head [rad/s]**	**Rot. motor [rad/s]**
Measurement 1	Head first	12.4	-9.4	21.8
	Tail first	-12.0	9.1	21.1
Measurement 2	Head first	11.7	-9.1	20.8
	Tail first	-11.4	8.6	20.1

object in a very viscous fluid, both when falling and when the engine is switched on: since the object is not microscopic, it is possible that the flow regime will not be linear, and described by the Stokes equations, unless velocity is very low. The numerical study proceeds as follows: first, the falling behaviour under applied force, of the two components, cargo and helix, and that of the entire swimmer (treated as rigid), is studied at increasing Reynolds numbers, that is, for increasing values of applied force. This falls within the range of problems studied in the numerical benchmark above, for spherical geometries, with the difference that the chirality of the helix can generate rotations while translating. For the non-symmetric geometries, the free fall is simulated in both directions of translation (i.e., for the swimmer, cargo ahead or helix ahead), to check whether linearity of the problem, typical of Stokes flows, is lost upon increasing the velocity, resulting in asymmetries between the two different swimming directions. The simulations are performed with the Navier-Stokes solution procedure described in the previous sections. Simulations with a Stokes flow solver are performed as well, and results are compared to highlight the effect, if any, of non-linearities. Furthermore, the Stokes

calculations will yield all the necessary data needed for the calculations in the approach by Purcell, which assumes that the flow is Stokesian, as well as data to investigate the effect of confinement by a container. In fact, in order to compare numerical simulations with experimental measurements, we consider flows inside a cylindrical container with vertical axis aligned with the direction of gravity, and vary the radius of the container from $r = 48mm$ (for which we have experimental data, discussed in section 4.4), to large r to simulate the case of unconfined flow. In the following, for simplicity, we will consider the swimmer or the components to be constrained in such a way that only vertical (aligned with gravity) translation is allowed, together with rotation about the same vertical axis.

4.5.1 Results for Stokes flow

Here we calculate the resistance coefficients for the components of the swimmer and the assembled swimmer, when moving in a viscous fluid such that the Stokes flow approximation holds. The equations will therefore be linear, and so will the relation between forces or torques and swimming velocities. Following [50], we denote the resistance coefficients of the propeller (that is, the helix) by A, B, and D, such that the force and torque acting on the body, when the motion is given by a velocity v and a rotation rate ω, are:

$$F = Av + B\omega, \tag{4.138}$$
$$T = Bv + D\omega, \tag{4.139}$$

where A and D are positive coefficients and we have used the fact that the resistance matrix is symmetric. These properties can be proved, for example, with arguments regarding the energy of the system and the dissipation properties of Stokes flow. We take the Stokes equations in non-dimensional form

$$\frac{1}{Re}\Delta\mathbf{u} + \nabla p = 0, \tag{4.140}$$

where we take as reference length the diameter of the cargo, $L = D$, while the reference velocity is unitary. The three resistance coefficients will be considered in non-dimensional form as well. They scale according to the following relations [50]:

$$A \sim \nu L, \qquad B \sim \nu L^2, \qquad D \sim \nu L^3. \tag{4.141}$$

The cargo itself will also be characterized by two resistance coefficients, since the resistance matrix is presumed to be diagonal (no chirality), A_0 and D_0 for translation and rotation, respectively. If an object (e.g. the propeller discussed in equations (4.138,4.139)) falls under an applied force P (for instance, its own weight) and zero torque, it will translate with velocity v_1, and rotate at rate Ω_1, given by

$$v_1 = \frac{PD}{AD - B^2}, \qquad \Omega_1 = -\frac{PB}{AD - B^2}. \tag{4.142}$$

These relation are obtained by setting $F = P$ and $T = 0$ in (4.138,4.139)) and solving for v_1 and Ω_1. Of course, if instead either rotation or translation are blocked by a constraint, we have

$$v_3 = \frac{P}{A}, \qquad \Omega_3 = \frac{M}{D}. \tag{4.143}$$

The Stokes problem was solved with a finite element discretization using the standard *P2/P1* elements for velocity and pressure. The system is solved monolithically with the *FEniCS* finite element library and forces and torques are integrated over the surface of the body. The domain boundaries consist of the outer surface of the body in the middle of a cylindrical domain, aligned with its axis. Possible boundary conditions on the surface of the body are

either unitary translation or unitary rotation rate. Again, only one translational and one rotational degrees of freedom are allowed. Therefore, the forces and torques represent directly the resistance coefficients due to linearity. On the outer surface of the cylinder a no-slip condition is imposed. The flow domain is cylindrical and of sufficient length so that the effect of its finiteness along the axis can be considered negligible. The radius of the cylinder instead has to be taken in account since the resistance coefficients are known to be affected by nearby walls. Therefore, for each case, when the head, helix or the entire swimmer are considered, the simulation is repeated for different radii, of the outer domain. For each geometry (that is, the combination of body geometry and outer domain radius), two simulations have to be performed: one to determine the rotational resistance coefficient D, with boundary conditions on the body of unitary rotation rate and blocked translation, and another to determine A and B by imposing unitary translational velocity and blocked rotation. It follows then, by (4.138, 4.139):

$$T_{v=0,\omega=1} = D, \tag{4.144}$$

$$F_{v=1,\omega=0} = A, \tag{4.145}$$

$$T_{v=1,\omega=0} = F_{v=0,\omega=1} = B. \tag{4.146}$$

In the following the coefficients calculated by solving numerically the Stokes equations are reported. The range of radii for the outer cylinder starts from a large value, approximating the case of an unbounded domain, and is gradually decreased to reach a value comparable to that of the diameter of the swimmer. The smallest radius considered coincides with the one of the PMMA cylinder used in the experiments, that is $48mm$. When the coefficients of the resistance matrix are known, its inverse can be readily calculated, yielding the mobility matrix, which will satisfy:

$$\begin{pmatrix} U \\ \Omega \end{pmatrix} = \begin{pmatrix} A_I & B_I \\ B_I & D_I \end{pmatrix} \begin{pmatrix} F \\ N \end{pmatrix}. \tag{4.147}$$

Therefore, if a unitary force is applied, we have $U = A_I$, $\Omega = B_I$. These relations will allow us to compare easily experiments and the Stokes flow predictions, since they can be applied directly to the case when an object falls due to an applied load, and velocity and rotation rate are measured. Results for the Stokes coefficients are reported in the following figures: in figure (4.10) and (4.11) the resistance coefficient for translation and the corresponding coefficient in the inverse matrix are reported, respectively. In these results the three cases of head, helix isolated and full swimmer are considered, and all coefficient are in non-dimensional form. In figure (4.12) the resistance coefficient for rotations is represented while in figure (4.13) the same is done for the off-diagonal coupling term of the resistance matrix. Since we have the coefficients for the swimmer as well as for the two components separately, a direct comparison can show the effect of hydrodynamic interactions, as discussed in [27]. In figure (4.14) we plot the resistance coefficient for translation in two cases, first simply calculating the sum of the coefficients for head and tail (which is the common additive approximation done in the low Reynolds regime), then this is compared with the actual hydrodynamic coefficient of the swimmer. The comparison shows clearly that neglecting the interactions, or equivalently, using the approximation of additivity of the resistance coefficients, leads to overestimating the resistance coefficients. This is expected: because of the presence of the first component, which had already deformed the fluid particles surrounding it, it becomes easier for the second component to move in the "wake" of the first, as compared to the case where the second component moves alone. The same simulations can be made for the case when the tail is a double helix, introduced in section 4.4 to prevent excessive wobbling of the swimmer. In figure 4.15 and 4.16 we report the resistance coefficients to translation and the comparision of results when additivity is either used or not, respectively.

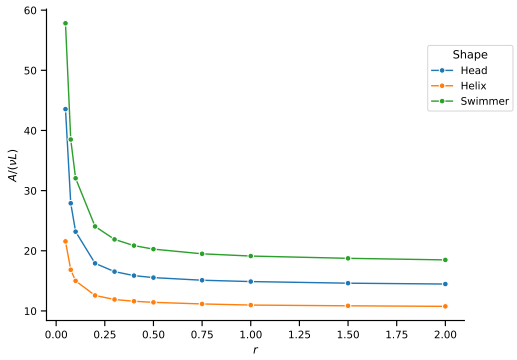

FIGURE 4.10: Resistance coefficients for translation in Stokes flow.

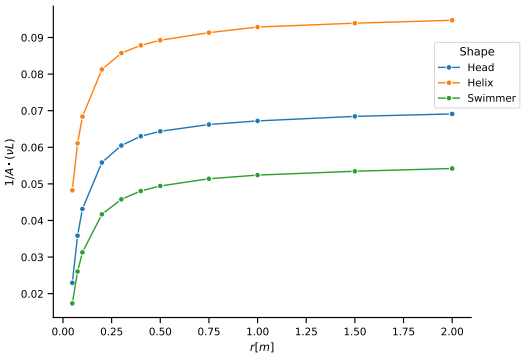

FIGURE 4.11: Translation coefficient of the inverse resistance matrix.

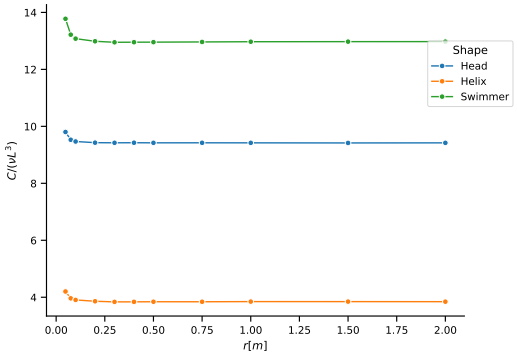

FIGURE 4.12: Resistance coefficients for rotation in Stokes flow.

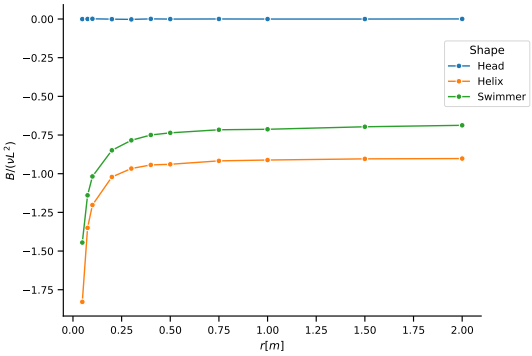

FIGURE 4.13: Resistance coefficients, off-diagonal, in Stokes flow.

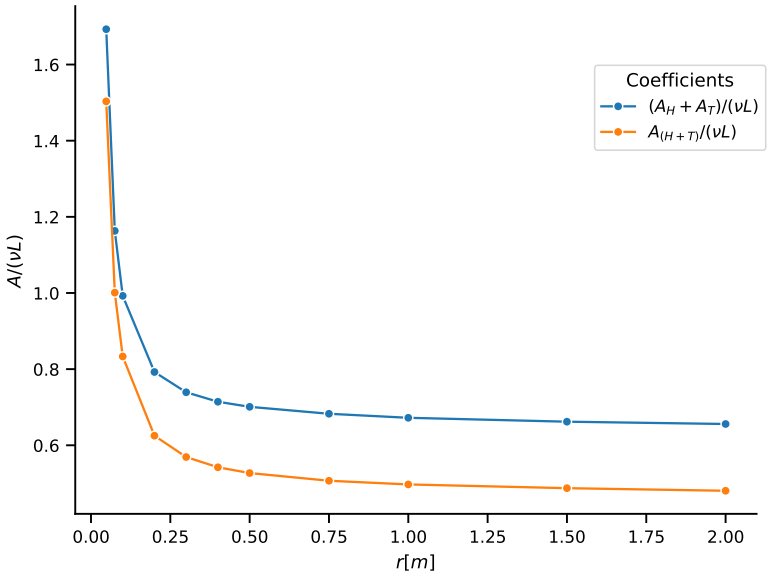

FIGURE 4.14: Comparison of resistance coefficients for translation in the two cases when interactions of the flows around head and helix are either considered $(A_{(H+T)})$ or neglected $(A_H + A_T)$.

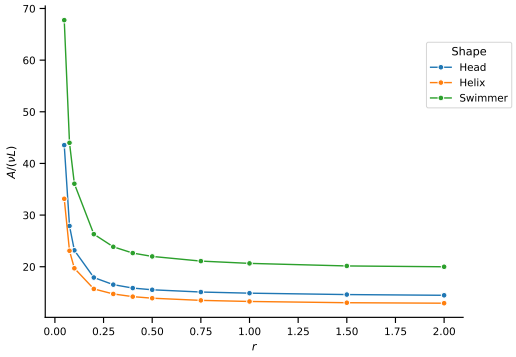

FIGURE 4.15: Resistance coefficients for translation in Stokes flow: case of tail as a double helix.

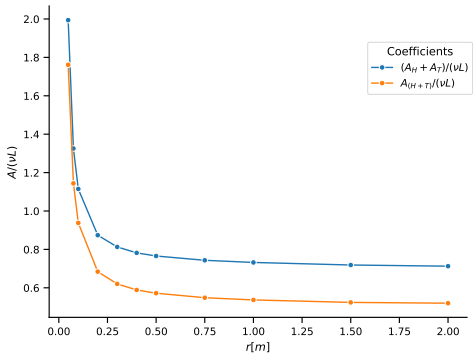

FIGURE 4.16: Comparison of resistance coefficients for translation in the two cases when interactions of the flows around head and helix are either considered $(A_{(H+T)})$ or neglected $(A_H + A_T)$: case of tail as a double helix.

4.5.2 Free falling behaviour of helix, cargo and full swimmer in the finite Reynolds regime

The full Navier-Stokes equations, in the form (4.84), are then solved with the numerical techniques exposed previously. The fluid flow domain here is cylindrical and has the same dimensions of the tube used in the experiments, that is a radius of $48mm$ and $1m$ height. This will allow us to compare experimental and numerical results. In all cases, the boundary conditions are no-slip on the lateral surface of the cylinder and on the base which faces the direction of swimming, in order to have a situation similar to the experiments. In all cases the simulations start from a condition of rest. All meshes are unstructured and consist of tetrahedra, generated with the open source *gmsh* mesh generator. The geometry is given by the outer surface of the bodies, that is imported directly from the CAD models that were used for the 3D printing of the swimmer. First, the falling behaviour of the components of the swimmer is simulated. More precisely we measure numerically the terminal velocity when the body, initially at rest, is dragged down by a vertical force due to an added weight. The body is almost buoyant and thus the motion can be attributed entirely to the action of the additional weight. Increasing weights are applied and the simulations are carried on until a certain stopping criterion is met, that is, until the magnitude of the increment in velocities vector in one time step is below a certain user-specified threshold (usually a relative variation of $1e^{-5}$ over one time-step). The results help to clarify the effect of the increasing Reynolds number, and therefore of the fluid non-linearities, on the swimming problem. If an external vertical force is applied on the body, the ODEs (4.106) governing the rigid motion of the swimmer or of any of its components are:

$$\rho_r V \left(\frac{d\mathbf{U}}{dt} + \mathbf{\Omega} \times \mathbf{U} \right) = \mathbf{F}_{fl} + \frac{1}{\rho_f} \mathbf{F}_V, \tag{4.148}$$

$$\mathbf{I} \frac{d\mathbf{\Omega}}{dt} + \mathbf{\Omega} \times (\mathbf{I}\mathbf{\Omega}) = \mathbf{M}_{fl}, \tag{4.149}$$

where the vertical force $\mathbf{F}_V$ applied has to be normalized by the density of the fluid, since all other quantities already are. The results from this procedure for the helix and head of the swimmer separately are reported in figures 4.18 and 4.17, respectively. It can be seen, particularly from the results of the freely falling cargo, that after a certain velocity the linearity of the flow is lost, as the drag is no longer due to viscosity alone but inertial terms start to play a role.

The process is then applied to the entire body of the swimmer. For each force, the terminal speed is calculated when it is applied in such a way that the swimmer falls either head first or tail first. Such a distinction would not make sense in the Stokesian realm, but it does if the Reynolds number becomes finite. However, in the experiments the force applied is low, and thus, looking the numerical data reported so far, it can be expected that the regime of flow in the experiments be close to linear. Indeed, the differences in the swimming velocities, seen from figure (4.19) when the body moves head-first or tail-first, appear to be small.

4.5.3 Motion for the case of helix actuation

The second case studied is that of an internal actuation of the motor inside the head of the swimmer, that produces a relative rotation between head and helix. As a first approximation, we assume that the motor is able to impose a constant relative rotation of the helix with respect to the head irrespective of the resistance of the fluid. Therefore, the dynamics of the motor are neglected for simplicity, and for a specified rotation rate of the motor, it will hold

$$\Omega_{z,\mathrm{HEAD}} = \Omega_{z,\mathrm{HELIX}} - \Omega_{z,\mathrm{MOTOR}}, \tag{4.150}$$

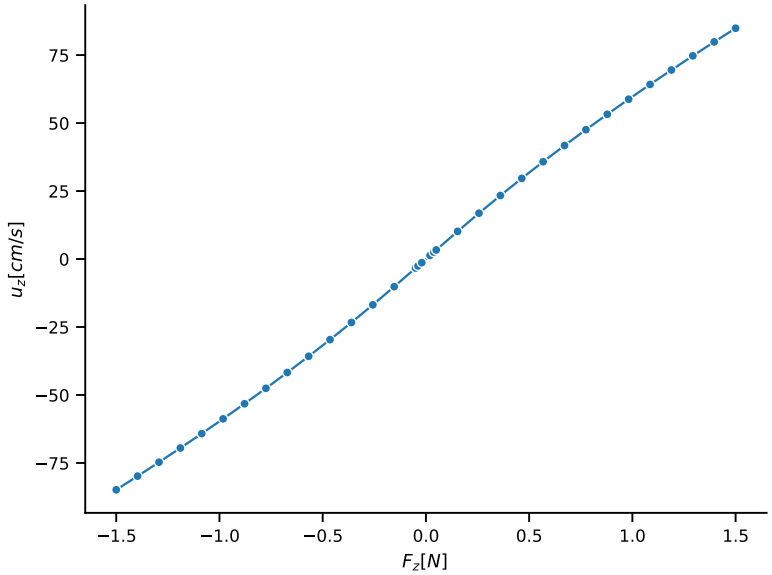

FIGURE 4.17: Terminal velocity for the free-falling head of the swimmer, Navier-Stokes case.

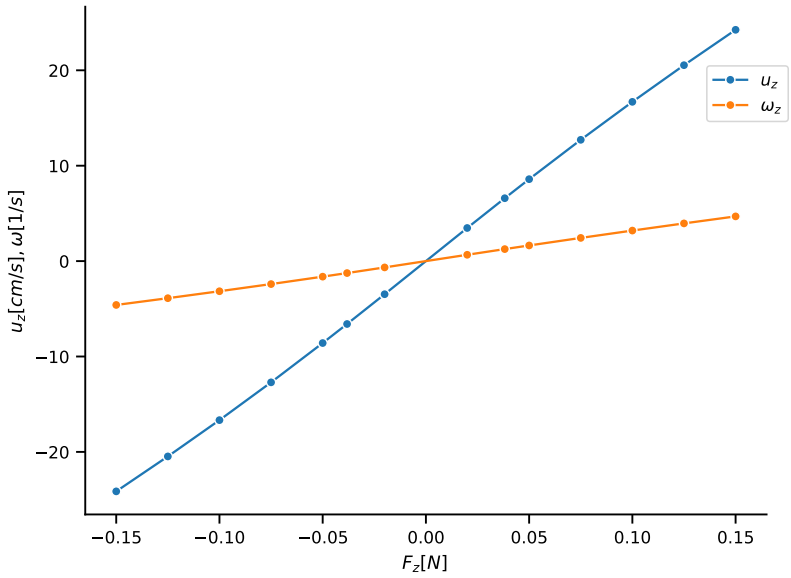

FIGURE 4.18: Terminal velocity for the free-falling tail of the swimmer, Navier-Stokes case. Tail as a single helix.

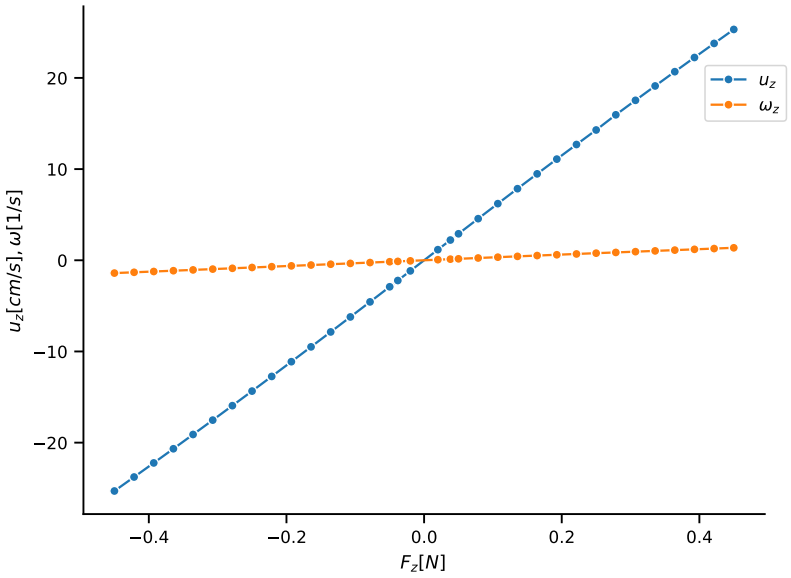

FIGURE 4.19: Terminal velocity for the free-falling swimmer, no relative rotation between head and tail ($\boldsymbol{\omega} = \mathbf{0}$), Navier-Stokes case. Tail as a single helix.

at any time. The technique adopted so far entails the rotation of the control volume around the body in order to have a body-fitted mesh that is seen as fixed in the solution process. Here, the domain would deform and be time-dependent if the rotation of the helix would not be followed, since a finite helix is not axi-symmetric. This implies that the rotation of the system where the equations of fluid and solid are solved is that of the helix. The rotation rate of the head, which is given by (4.150), will be different, but since only rotations around its axis of symmetry are allowed, the shape of the boundaries is left unaltered by this relative rotation between the two components of the swimmer. Therefore, the technique applied so far for the solution of the motion of rigid bodies applies to the present case as well, even though the body is deformable (with one degree of freedom). The motor, in this simplified model, will apply a torque in order to satisfy relation (4.150). This torque is internal, since it is applied both to the helix and to the head, with opposite signs. Since there are no external torques applied on the swimmer, the ODEs for the rotational degrees of freedom of the body are obtained by imposing that the (resistive) torques acting on the helix and on the head balance the inertial rotational term (which could be zero if steady state is reached):

$$I_z \dot{\Omega}_z = M_{z,\mathrm{HEAD}} + M_{z,\mathrm{HELIX}} \tag{4.151}$$

Simulations are run for a range of relative rotational rates imposed by the motor, until a steady state is reached. Results are reported in figure 4.20, where velocities are scaled in order to make the trend easier to appreciate. The efficiency of the swimmer in terms of net velocity produced is low, as is common for swimmers at low Reynolds numbers [50]. As expected intuitively, the rotations of head and helix are opposite in sign, since no external torque is acting on the system, and the rotation rates of the head, which has a higher rotational resistance, are smaller in magnitude than those of the helix.

4.5.4 The double helix

It has been observed in the experiments that the swimmer (with a single helical propeller),

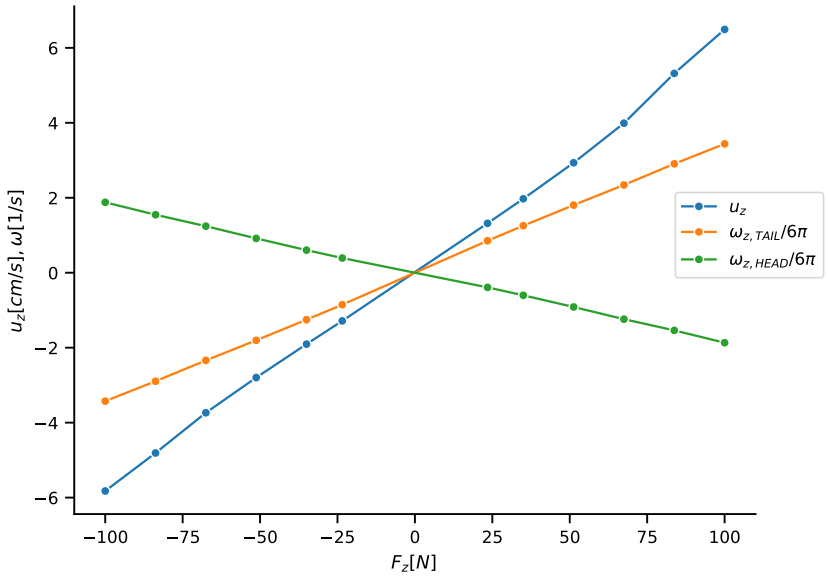

FIGURE 4.20: Vertical (z direction) velocity and rotation rate (about z axis) of the swimmer for a range imposed relative rotation between tail and head: case of tail as a single helix. Rotation rates are expressed in revolutions per second.

when actuated, tends to move in a helical trajectory that can be attributed to the finite length of the helix. This behaviour is different when the swimmer moves head first or tail first, and therefore we hypothesize that this might be the cause of the different velocities observed in the experiments when the swimmer is actuated with either positive or negative rotation rates of the motor. We perform the same simulations for the different geometry of the propeller, with two helices as seen in figure 4.9. The results for the swimming speeds are reported in figure 4.21.

4.6 Discussion and conclusions

We can now compare the results from different predictions: the numerical coefficients obtained by solving the Stokes flow can be employed to predict the swimming velocity (actuated robot). This result can then be compared with the numerical results for swimming, obtained by solving the Navier-Stokes equations. Finally, all predictions are compared with the actual experimental results reported in section 4.4. Starting with the case of the single helix, Stokes coefficients are reported in table 4.6. We note again that the resistance coefficients are not additive, since the resistance coefficient of the swimmer are lower in magnitude than those obtained by summing the coefficients of head and tail. Thus, making the assumption of additivity introduces a further approximation. With these coefficients one can estimate the swimming speed (when the motor is activated) with Purcell's formula, which we recall here:

$$v = -\frac{BD_0}{(A_0 + A)(D_0 + D) - B^2}\Omega_{\text{ENG}} \approx 0.46 = 11.96mm/s, \tag{4.152}$$

where the length scale is the diameter of the head and is equal to $26mm$. In tables 4.7 and 4.8 we report the comparison between numerics and experiments. In table 4.9 we compare Purcell's prediction, experiments and numerics. The prediction with Purcell's formula in this case is very close to the experimental value. We do the same comparison for the case of

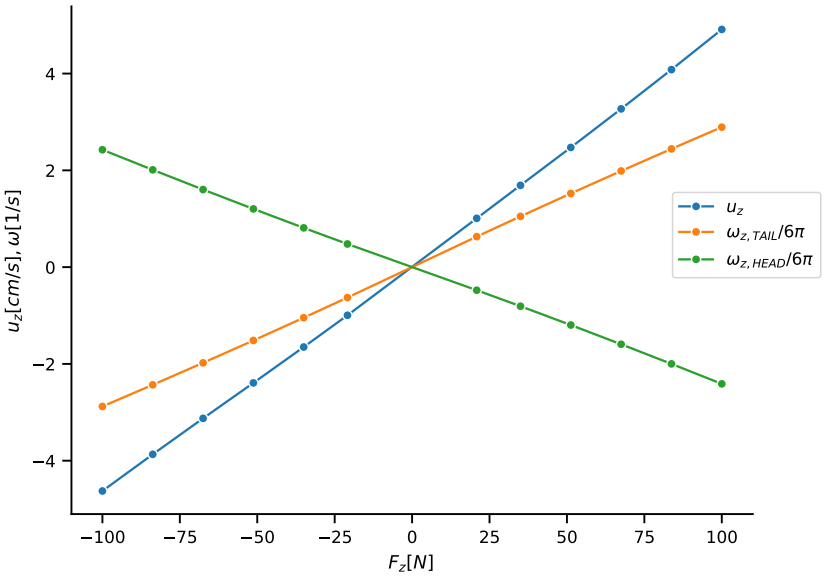

FIGURE 4.21: Vertical (z direction) velocity and rotation rate (about z axis) of the swimmer for a range of imposed relative rotation between the *double* tail and head: case of tail as a double helix. Rotation rates are expressed in revolutions per second.

the double tail, which exhibited a more regular trajectory along the axis of the tube. The resistance coefficients for Stokes flow are reported in table 4.10, while the predicted values are compared in table 4.11. In this case the prediction with Purcell formula is less accurate.

TABLE 4.6: Numerical results for the non-dimensional resistance coefficients in Stokes flow. The tail in this case is composed of a single helix.

Shape	**A**	**B**	**D**
Head	43.544	-	9.8023
Propeller	21.564	-1.8286	4.2021
Swimmer (head + propeller)	57.817	-1.4451	13.776

TABLE 4.7: Comparison of numerical and experimental results. The tail in this case is composed of a single helix.

Shape	**Fall velocity, Num. [mm/s]**	**Fall velocity, Exp. [mm/s]**	**Error**
Head	30.3	29.7	2.1%
Propeller	48.9	51.5	5.0%
Swimmer (head + propeller)	22.2	21.5	3.3%

Still, we can conclude that the prediction obtained with Purcell's formula works remarkably well in this setup, a result which is in contrast with other observations in literature [27], when the predictions using eq. (4.152) were found to be very rough with respect to numerics. In [27] however the flow was in an unbounded domain, while in the experiments the domain

TABLE 4.8: Comparison of numerical and experimental results. The propeller in this case is composed of a single helix.

Shape	**Rot. rate, Num. [rad/s]**	**Rot. rate, Exp. [rad/s]**	**Error**
Propeller	0.940	0.931	0.9%
Swimmer (head + propeller)	0.122	0.125	2.2%

TABLE 4.9: Comparison of numerical, experimental results and the analytic prediction. The tail in this case is composed of a single helix.

	Swimming velocity [mm/s]	**Error w.r.t. exp.**
Numerics, Navier-Stokes	13.2	5.5%
Prediction with eq. (4.152)	12.0	4.3%
Experiments	12.5	-

TABLE 4.10: Numerical results for the non-dimensional resistance coefficients in Stokes flow. The tail in this case is composed two helices.

Shape	**A**	**B**	**D**
Head	43.544	-	9.8023
Propeller	33.151	-2.0661	7.3404
Swimmer (head + propeller)	67.746	-1.6087	16.839

TABLE 4.11: Comparison of numerical, experimental results and the analytic prediction. The tail in this case is composed two helices.

	Swimming velocity [mm/s]	**Error w.r.t. exp.**
Numerics, Navier-Stokes	10.1	7.4%
Prediction with eq. (4.152)	8.3	13.3%
Experiments	9.4	-

is obviously limited. The radius of the cylindrical domain is small enough that the results are strongly affected, as can be seen by the results for the Stokes flow simulations, where a range of radii is considered. Some kind of approximation is usually expected from the results of formula (4.152), since this relies on the hypothesis of additivity, while it's been shown that the resistance coefficients of more components assembled together in general is lower than the sum of the coefficients of the same components when taken separately. In this case, however, it is likely that the high amount of drag due to the presence of the outer walls at such a close distance results in a decreased impact on the estimates of the approximation due to additivity. It should be noted, however, that if one wanted to reproduce the procedure proposed by Purcell, the resistance coefficients used in calculations should be obtained from experiments, while so far, direct Stokes flow simulations were performed. Formula (4.152) would then be used to determine an estimate of the swimming velocity starting only from experimental observations. In particular, Purcell proposes a free-fall experiment of a system made of two helices, one the mirror reflection of the other, falling together without rotating. This would yield directly the resistance coefficient to translation of the helices. Then, the free fall of a single helix, which would also rotate in this case, is the other experiment needed to have enough equations to determine all the resistive coefficients of the propeller, while it

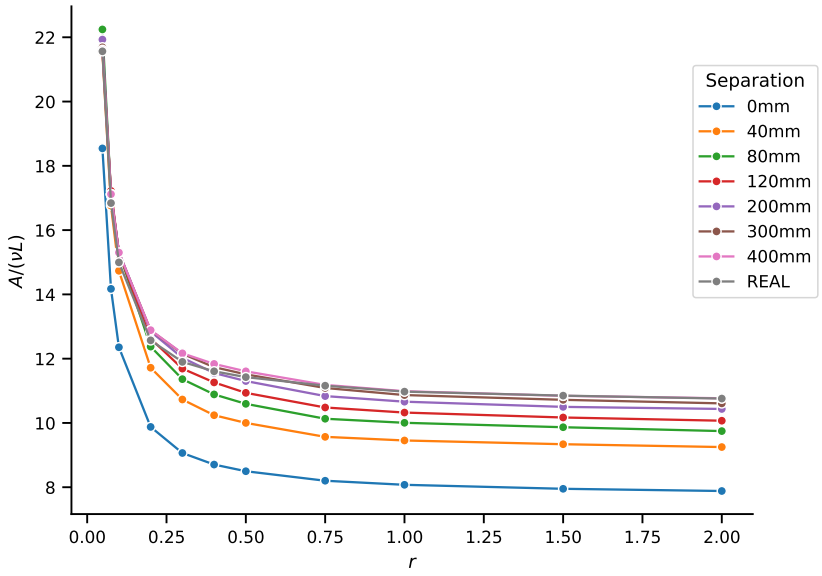

FIGURE 4.22: Resistive coefficient A for a pair of tails, one the mirror image of the other, falling along the axis a cylindrical tube, for increasing values of separation between them. Case of tails as single helices.

is assumed that those of the head are known (the head is spherical in Purcell's article). We report here the three equations for the coefficients of the helix: from the fall of one single helix due to the applied force F it follows

$$v_1 = \frac{FD}{AD - B^2}, \qquad \Omega_1 = -\frac{FB}{AD - B^2}, \tag{4.153}$$

while from the fall of the two mirrored helices one obtains:

$$v_2 = \frac{F}{2A}. \tag{4.154}$$

Measuring the translational and rotational velocities from the two experiments yields the resistance coefficients. This experiments of course also relies on the hypothesis of additivity. Additivity therefore has to be applied twice: once, to solve the inverse problem of determining the coefficients of the propeller (and of the head if, needed) from measured velocities of free-fall experiments, and a second time to apply formula (4.152). The approximation introduced by additivity seems to greatly affect the results of the first step, that is the determination of coefficients from the experiments: calculation of the coefficients starting from the experimental data reported above yields wrong results, even violating conditions on the sign of A and D (see below). On the other hand, it's been noted already that the estimation of the swimming speed seems to be less affected. To analyse this, we reproduce numerically the experiment proposed of Purcell, with two helices (with the same geometry studied so far) mirrored and falling jointly (in a rigid body motion) along the axis of the tube, but separated by an increasing distance. The effect of the radius of the outer domain will also be taken into account. The translation resistive coefficient is measured by solving the Stokes flow for each couple of helices and using eq. (4.154). To emulate a falling experiment of the helix alone, knowing already the resistance matrix from the previous Stokes flow simulations, we calculate its inverse like in eq. (4.147). Then for any value of applied force F one obtains the velocities v_1 and Ω_1 needed to solve equation (4.153). In this way one can examine which results would be given

by Purcell's procedure, only with measurements replaced by numerical solution of a Stokes problem, therefore accurate up to the numerical errors. The next step would be to calculate the coefficients D, of resistance to rotation, and the off-diagonal coupling term B:

$$D = \left(A - \frac{F}{v_1}\right)\left(\frac{v_1}{\Omega_1}\right)^2, \qquad B = -\frac{\Omega_1}{v_1}D. \tag{4.155}$$

In figure 4.22 we report the calculated resistive coefficient for the pair of helices, starting from the case of a standard helix, while the double helix introduced to avoid excessive wobbling will be studied next. It is clear that the distance between the two mirrored propellers greatly affects the value of the resistive coefficient, and this value is close to twice the resistance of an isolated helix (indicated as real in figure) only for a great separation, which amounts to several times the length of the helix. Therefore, using the hypothesis of additivity, that is taking the resistance of the pair and dividing by two, clearly leads to underestimating the real value. Having calculated A in this way, one can proceed with equations (4.155). The results for the coefficients D, and then B are given in figures 4.23 and 4.24, respectively. The most striking consequence of the approximation introduced with additivity is that non-physical (negative) values result for the coefficient D when the separation between the helices of a pair is not wide enough. Furthermore, one can notice how the value of the D coefficient clearly depends on the radius of the outer wall. The real coefficient instead, also reported in figure, is not as affected by the outer boundary. This is the expected correct behaviour, which can be inferred by the following rationale [27]: in Stokes flow, a translating sphere can be modelled as a *Stokeslet*, which causes a disturbance in the flow that decays linearly with distance. On the other hand, a rotating sphere can be described as a *rotlet*, whose decay is instead cubic with distance. Since the resistive coefficient D is related to rotations, it can be expected to be much less affected by the outer boundaries than the translational coefficient A. However, since the experimental determination of coefficients proposed by Purcell entails calculating the other coefficients starting from A, we see that another clear source of error will be introduced by this procedure. Formula (4.152) can finally be used to obtain an estimate of how well Purcell's prediction would perform if one were to use this procedure, applying the additivity hypothesis twice. These results are calculated only for the values that yield physical results for all radii of the external tube, and are given in figure 4.25. In this figure we also report the prediction obtained previously, with the additivity hypothesis applied only once. Furthermore, another prediction can used for comparison, that of Giuliani et al. [27], who propose an estimate that doesn't rely on additivity. Their formula for the swimming speed is:

$$v = \frac{(B_1 + B_2)\left((D_1 + D_2)\frac{\hat{B}_2}{B_1 + B_2} - D_2\right)}{(D_1 + D_2)(A_1 + A_2) - (B_1 + B_2)^2}\Omega_{\mathrm{ENG}}, \tag{4.156}$$

where the following coefficients appear: starting from the geometry of the assembled swimmer, A_1 and A_2 are calculated by measuring the resistance acting on the whole body when unitary velocity is assigned as boundary condition on the head or on the propeller, respectively, while it is set to zero on the rest of the body. The same is done to calculate D_1 and D_2, with a rotational velocity. For the coupling terms instead, one needs to introduce four more coefficients, namely $\overline{B}_1$ and $\overline{B}_2$, which are given by the measure of the torques on the body when a translational velocity is assigned on either the head or the propeller, and $\hat{B}_1$ and $\hat{B}_2$, given by the forces acting on the body for rotational velocities. Since the resistance matrix of the whole swimmer has to be symmetric, it holds $\overline{B}_1 + \overline{B}_2 = \hat{B}_1 + \hat{B}_2$ and the value of either sum can be denoted with $B_1 + B_2$. Going back to figure 4.25, it is clear that the prediction using coefficients obtained with the additive procedure can be very rough, but all predictions give reasonable estimates for the smaller value of radius, which is $48mm$ and coincides with the radius of the tube in the experimental setup. This can be seen as another

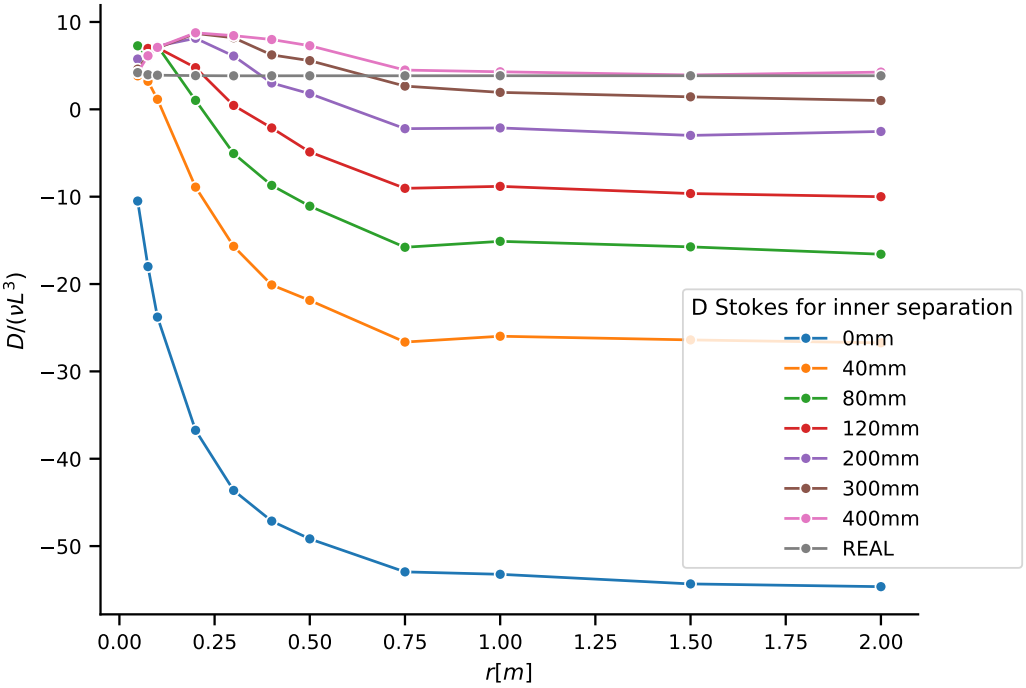

FIGURE 4.23: Resistive coefficient D of the tail, when it is calculated with the additive procedure, for increasing values of separation between the two mirrored tails when data was measured: case of tails as single helices.

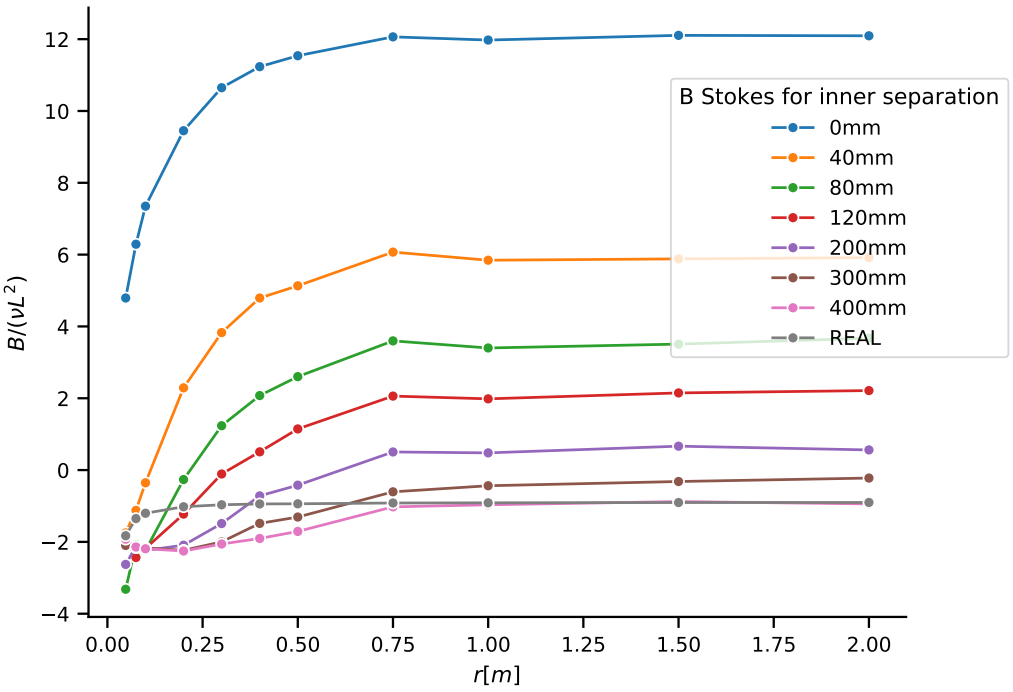

FIGURE 4.24: Resistive coefficient B of the tail, when it is calculated with the additive procedure, for increasing values of separation between the two mirrored tails when data was measured: case of tails as single helices.

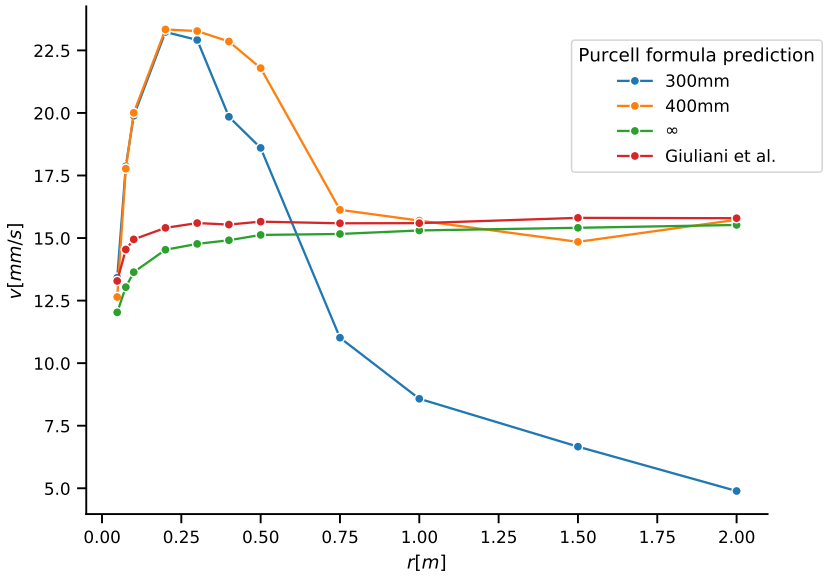

FIGURE 4.25: Predictions of the swimming velocity: case of tail as single helix.

confirmation that the effect of the domain has the final result of improving the performance of these predictions.

The same analysis is now repeated for the case when the propeller used is the double helix that reduces wobbling effects, as shown in figure 4.9. Measurements of the resistance coefficients are given in figure 4.26, 4.27 and 4.28 for translation, rotataion and coupling, respectively. Comparison of predictions from all the calculations that involve additivity are given in figure 4.29. Again, it can be concluded that additivity leads to rough approximations of the real coefficients of the resistance matrix if one starts from the experiments, while all the predictions that involve additivity only once perform reasonably well, especially when the radius of the cylindrical domain is small, that is comparable with the diameter of the head of the swimmer.

4.6.1 Ongoing and future work

The numerical results indicate that the experimental conditions were indeed close to the Stokes flow model. In the future an additional campaign of experiments and simulations will be carried out to study conditions where non-linearity is present, and the Stokes approximation in no longer acceptable. Furthermore, experiments with a cylindrical domain of larger radius will be done, in order to analyse the performance of Purcell's prediction when the drag induced by outer walls is lower, and determine if it is still yields acceptable estimates of the swimming velocity.

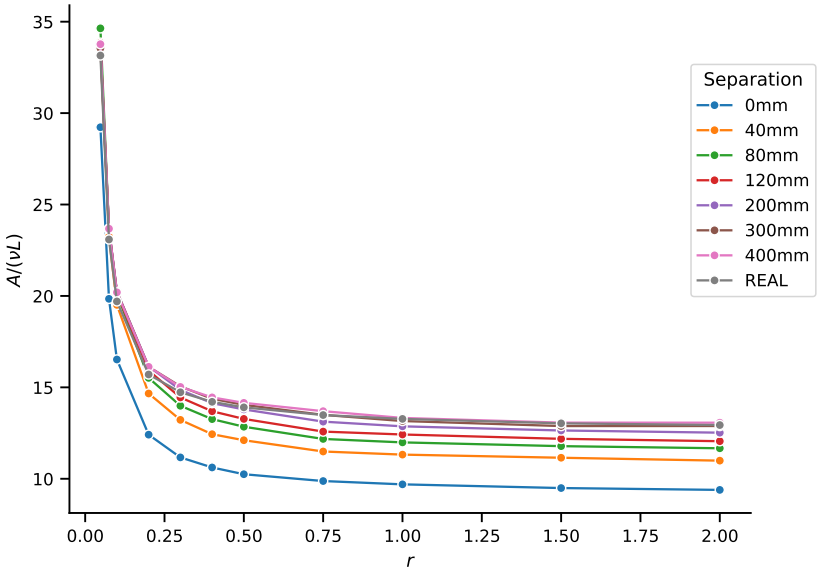

FIGURE 4.26: Resistive coefficient A for a pair of propellers, each consisting of two helices, and one the mirror image of the other, falling along the axis a cylindrical tube, for increasing values of separation between them. Case of tail as double helix.

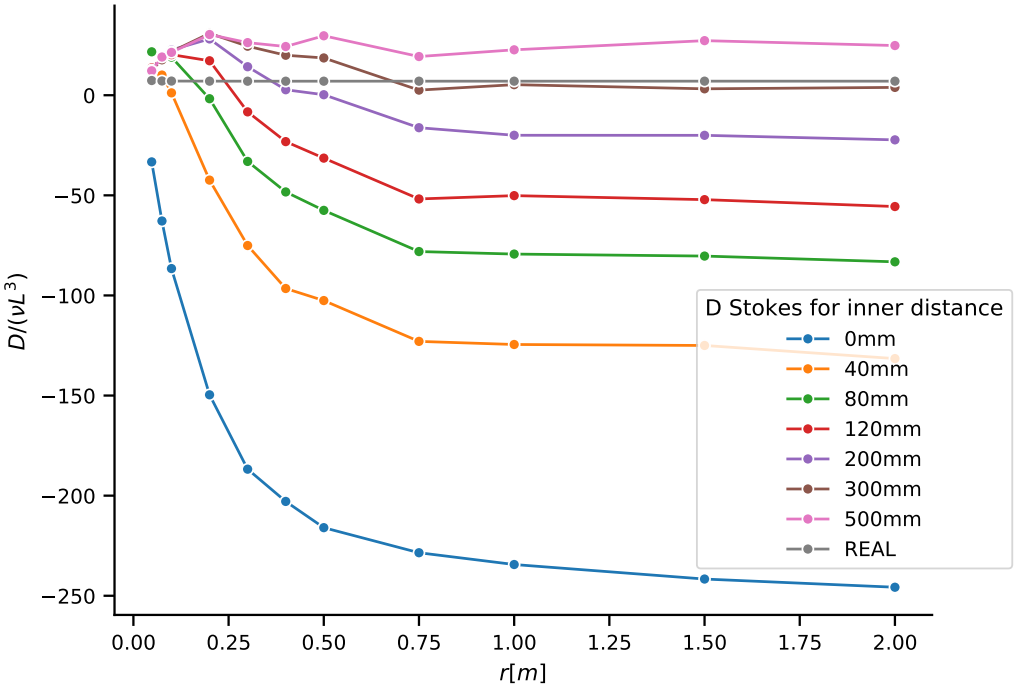

FIGURE 4.27: Resistive coefficient D of the tail, when it is calculated with the additive procedure, for increasing values of separation between the two mirrored tails when data was measured: case of tails as double helices.

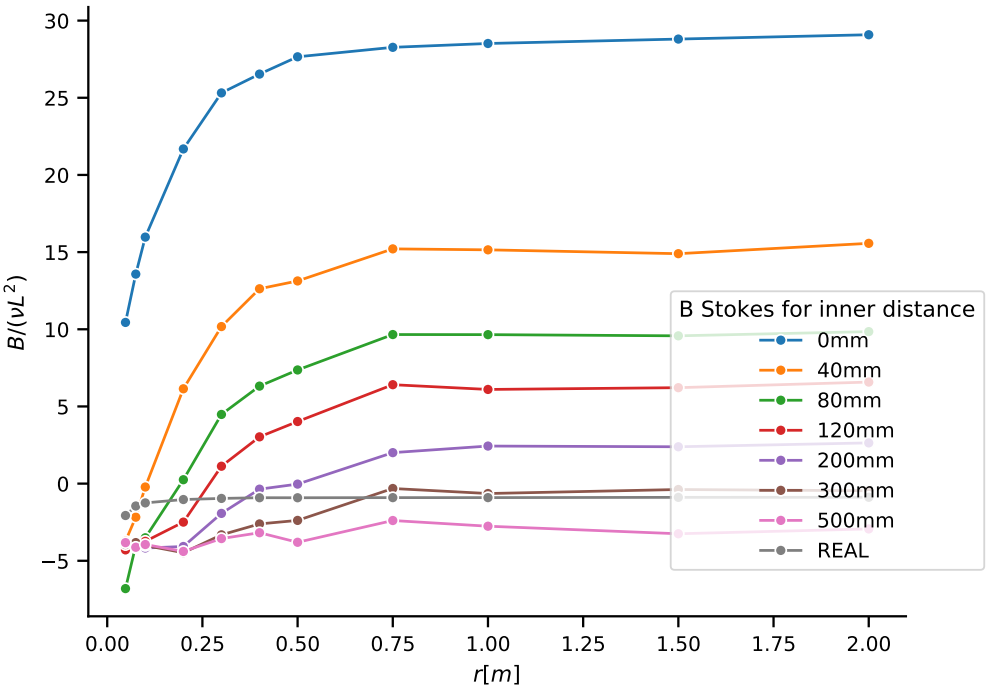

FIGURE 4.28: Resistive coefficient B of the tail, when it is calculated with the additive procedure, for increasing values of separation between the two mirrored tails when data was measured: case of tails as double helices.

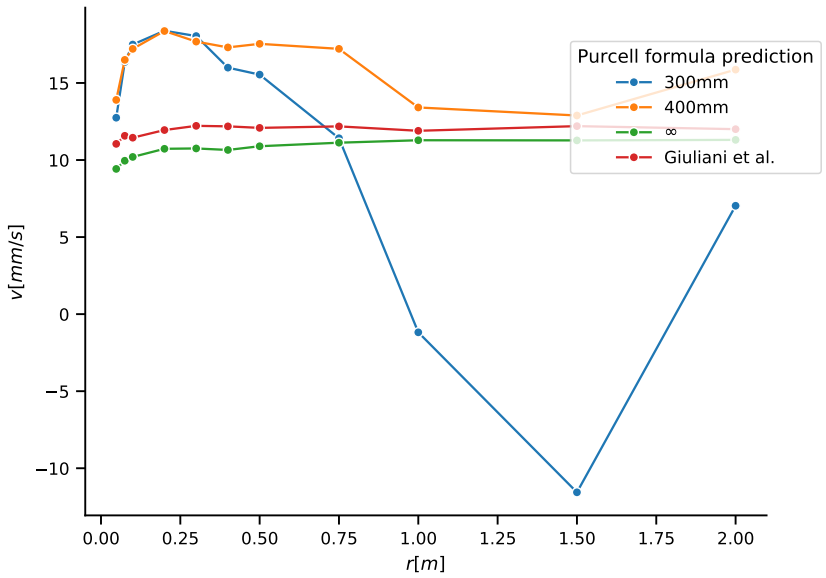

FIGURE 4.29: Predictions of the swimming velocity: case of tail as double helix.

Bibliography

[1] A. Allendes, E. Otárola, and A. J. Salgado. "A posteriori error estimates for the Stokes problem with singular sources". In: *Computer Methods in Applied Mechanics and Engineering* 345 (2019), pp. 1007–1032. ISSN: 0045-7825. DOI: https://doi.org/10.1016/j.cma.2018.11.004. URL: http://www.sciencedirect.com/science/article/pii/S0045782518305590.

[2] M. S. Alnæs et al. "The FEniCS Project Version 1.5". In: *Archive of Numerical Software* 3.100 (2015). DOI: 10.11588/ans.2015.100.20553.

[3] F. Alouges, A. DeSimone, and A. Lefebvre. "Optimal strokes for low Reynolds number swimmers: an example". In: *Journal of Nonlinear Science* 18.3 (2008), pp. 277–302.

[4] F. Alouges et al. "Energy-optimal strokes for multi-link microswimmers: Purcell's loops and Taylor's waves reconciled". In: *New Journal of Physics* 21 (2019), p. 043050.

[5] F. Auguste and J. Magnaudet. "Path oscillations and enhanced drag of light rising spheres". In: *Journal of Fluid Mechanics* 841 (2018), pp. 228–266.

[6] F. Auguste and J. Magnaudet. "Path oscillations and enhanced drag of light rising spheres". In: *Journal of Fluid Mechanics* 841 (2018), pp. 228–266. DOI: 10.1017/jfm.2018.100.

[7] S. Balay et al. *PETSc Users Manual*. Tech. rep. ANL-95/11 - Revision 3.11. Argonne National Laboratory, 2019. URL: https://www.mcs.anl.gov/petsc.

[8] Y. Bazilevs, K. Takizawa, and T. E. Tezduyar. *Computational Fluid-Structure Interaction: Methods and Applications*. John Wiley & Sons, 2013.

[9] M. Brunetti, S. Vidoli, and A. Vincenti. "Bistability of orthotropic shells with clamped boundary conditions: An analysis by the polar method". In: *Composite Structures* 194 (2018), pp. 388–397. ISSN: 0263-8223. DOI: https://doi.org/10.1016/j.compstruct.2018.04.009. URL: http://www.sciencedirect.com/science/article/pii/S0263822317342150.

[10] Y. Cha et al. "Energy harvesting from a piezoelectric biomimetic fish tail". In: *Renewable Energy* 86 (2016), pp. 449–458. ISSN: 0960-1481. DOI: https://doi.org/10.1016/j.renene.2015.07.077. URL: http://www.sciencedirect.com/science/article/pii/S0960148115301737.

[11] S. Childress. *Mechanics of Swimming and Flying*. Cambridge Studies in Mathematical Biology. Cambridge University Press, 1981. DOI: 10.1017/CBO9780511569593.

[12] S. Childress. *Some notes on locomotion at low and intermediate Reynolds numbers*. June 2010.

[13] M. Chrust, G. Bouchet, and J. Dušek. "Effect of solid body degrees of freedom on the path instabilities of freely falling or rising flat cylinders". In: *Journal of Fluids and Structures* 47 (2014), pp. 55–70.

[14] M. Chrust, G. Bouchet, and J. Dušek. "Effect of solid body degrees of freedom on the path instabilities of freely falling or rising flat cylinders". In: *Journal of Fluids and Structures* 47 (2014). Special Issue on Unsteady Separation in Fluid-Structure Interaction-l, pp. 55–70. ISSN: 0889-9746. DOI: https://doi.org/10.1016/j.jfluidstructs.2013.09.016. URL: http://www.sciencedirect.com/science/article/pii/S0889974613002016.

[15] Cicconofri, G. and DeSimone, A. "Motion planning and motility maps for flagellar microswimmers". In: *Eur. Phys. J. E* 39.7 (2016), p. 72.

[16] E. T. Copson. "On certain dual integral equations". In: *Proceedings of the Glasgow Mathematical Association* 5.1 (1961), pp. 21–24.

[17] G. Corsi et al. "A neutrally stable shell in a Stokes flow: a rotational Taylor's sheet". In: *Proceedings of the Royal Society A* 475.2227 (2019), p. 20190178.

[18] A. Daddi-Moussa-Ider et al. "Dynamics of a microswimmer microplatelet composite". In: *Physics of Fluids* 32.2 (2020), p. 021902. DOI: 10.1063/1.5142054.

[19] M. Dasgupta et al. "Speed of a swimming sheet in Newtonian and viscoelastic fluids". In: *Phys. Rev. E* 87 (1 Jan. 2013), p. 013015. DOI: 10.1103/PhysRevE.87.013015.

[20] A. DeSimone. "Spontaneous bending of pre-stretched bilayers". In: *Meccanica* 53.511 (2018). ISSN: 1572-9648. DOI: 10.1007/s11012-017-0732-z.

[21] A. DeSimone, F. Alouges, and A. Lefebvre. "Biological Fluid Dynamics: Swimming at low Reynolds numbers". In: *Encyclopedia of Complexity and System Science* (2008).

[22] A. Djellouli et al. "Buckling Instability Causes Inertial Thrust for Spherical Swimmers at All Scales". In: *Phys. Rev. Lett.* 119 (22 Nov. 2017), p. 224501. DOI: 10.1103/PhysRevLett.119.224501. URL: https://link.aps.org/doi/10.1103/PhysRevLett.119.224501.

[23] J. Donea et al. "Arbitrary Lagrangian–Eulerian Methods". In: *Encyclopedia of Computational Mechanics*. American Cancer Society, 2004. Chap. 14. ISBN: 9780470091357. DOI: 10.1002/0470091355.ecm009. eprint: https://onlinelibrary.wiley.com/doi/pdf/10.1002/0470091355.ecm009. URL: https://onlinelibrary.wiley.com/doi/abs/10.1002/0470091355.ecm009.

[24] R. Dreyfus et al. "Microscopic artificial swimmers". In: *Nature* 437.7060 (2005), pp. 862–865. DOI: 10.1038/nature04090. URL: https://doi.org/10.1038/nature04090.

[25] A. Ern and J. Guermond. *Theory and Practice of Finite Elements*. Applied Mathematical Sciences. Springer New York, 2004. ISBN: 9780387205748. URL: https://books.google.it/books?id=CCjm79FbJbcC.

[26] C. Geuzaine and J.-F. Remacle. "Gmsh: a three-dimensional finite element mesh generator with built-in pre- and post-processing facilities". In: *International Journal for Numerical Methods in Engineering* 79.11 (2009), pp. 1309–1331.

[27] N. Giuliani, L. Heltai, and A. DeSimone. "Predicting and Optimizing Microswimmer Performance from the Hydrodynamics of Its Components: The Relevance of Interactions". In: *Soft Robotics* 5.4 (2018), pp. 410–424. DOI: 10.1089/soro.2017.0099.

[28] J. L. Guermond, P. Minev, and J. Shen. "Error Analysis of Pressure-Correction Schemes for the Time-Dependent Stokes Equations with Open Boundary Conditions". In: *SIAM Journal on Numerical Analysis* 43.1 (2005), pp. 239–258. DOI: 10.1137/040604418.

[29] J. L. Guermond and J. Shen. "Velocity-Correction Projection Methods for Incompressible Flows". In: *SIAM Journal on Numerical Analysis* 41.1 (2003), pp. 112–134. DOI: 10.1137/S0036142901395400.

[30] S. Guest and S. Pellegrino. "Analytical models for bistable cylindrical shells". In: *Proceedings of the Royal Society Series B Mathematical, Physical and Engineering Sciences* 462.2067 (2006), pp. 839–854.

[31] J. S. Hale et al. "Simple and extensible plate and shell finite element models through automatic code generation tools". In: *Computers & Structures* 209 (2018), pp. 163–181. ISSN: 0045-7949. DOI: https://doi.org/10.1016/j.compstruc.2018.08.001. URL: http://www.sciencedirect.com/science/article/pii/S0045794918306126.

[32] W. Hamouche et al. "Basic criteria to design and produce multistable shells". In: *Meccanica* 51.10 (2016), pp. 2305–2320.

[33] W. Hamouche et al. "Multi-parameter actuation of a neutrally stable shell: a flexible gear-less motor". In: *Proceedings of the Royal Society of London A: Mathematical, Physical and Engineering Sciences* 473.2204 (2017). ISSN: 1364-5021. DOI: 10.1098/rspa.2017.0364. eprint: http://rspa.royalsocietypublishing.org/content/473/2204/20170364.full.pdf. URL: http://rspa.royalsocietypublishing.org/content/473/2204/20170364.

[34] J. Happel and H. Brenner. *Low Reynolds number hydrodynamics*. Martinus Nijhoff Publishers, 1983.

[35] M. Jenny, J. Dusek, and G. Bouchet. "Instabilities and transition of a sphere falling or ascending freely in a Newtonian fluid". In: *Journal of Fluid Mechanics* 508 (2004), p. 201.

[36] M. Jenny and J. Dušek. "Efficient numerical method for the direct numerical simulation of the flow past a single light moving spherical body in transitional regimes". In: *Journal of Computational Physics* 194.1 (2004), pp. 215–232. ISSN: 0021-9991. DOI: https://doi.org/10.1016/j.jcp.2003.09.004. URL: http://www.sciencedirect.com/science/article/pii/S0021999103004674.

[37] D. F. Katz. "On the propulsion of micro-organisms near solid boundaries". In: *Journal of Fluid Mechanics* 64.1 (1974), pp. 33–49. DOI: 10.1017/S0022112074001984.

[38] H. Lamb. *Hydrodynamics*. Cambridge University Press, 1932.

[39] E. Lauga and T. R. Powers. "The hydrodynamics of swimming microorganisms". In: *Reports on Progress in Physics* 72.9 (2009), p. 096601. URL: http://stacks.iop.org/0034-4885/72/i=9/a=096601.

[40] E. Lauga. "Propulsion in a viscoelastic fluid". In: *Physics of Fluids* 19.8 (2007), p. 083104. DOI: 10.1063/1.2751388. URL: https://doi.org/10.1063/1.2751388.

[41] L. Li and S. E. Spagnolie. "Swimming and pumping of rigid helical bodies in viscous fluids". In: *Physics of Fluids* 26.4 (2014), p. 041901. DOI: 10.1063/1.4871084. eprint: https://doi.org/10.1063/1.4871084. URL: https://doi.org/10.1063/1.4871084.

[42] J. Lighthill. "Flagellar Hydrodynamics". In: *SIAM Review* 18.2 (1976), pp. 161–230. DOI: 10.1137/1018040.

[43] S. Michelin and O. Doaré. "Energy harvesting efficiency of piezoelectric flags in axial flows". In: *Journal of Fluid Mechanics* 714 (2013), pp. 489–504. DOI: 10.1017/jfm.2012.494.

[44] L. N. Milne Thomson. *Theoretical Hydrodynamics*. 4th. The Macmillan and Company, 1962.

[45] M. Mortensen and K. Valen-Sendstad. "Oasis: A high-level/high-performance open source Navier–Stokes solver". In: *Computer Physics Communications* 188 (2015), pp. 177–188. ISSN: 0010-4655. DOI: https://doi.org/10.1016/j.cpc.2014.10.026. URL: http://www.sciencedirect.com/science/article/pii/S0010465514003786.

[46] G. Mougin and J. Magnaudet. "The generalized Kirchhoff equations and their application to the interaction between a rigid body and an arbitrary time-dependent viscous flow". In: *International Journal of Multiphase Flow* 28.11 (2002), pp. 1837–1851. ISSN: 0301-9322. DOI: https://doi.org/10.1016/S0301-9322(02)00078-2. URL: http://www.sciencedirect.com/science/article/pii/S0301932202000782.

[47] A. Plaza and G. Carey. "Local refinement of simplicial grids based on the skeleton". In: *Applied Numerical Mathematics* 32.2 (2000), pp. 195–218. ISSN: 0168-9274. DOI: https://doi.org/10.1016/S0168-9274(99)00022-7. URL: http://www.sciencedirect.com/science/article/pii/S0168927499000227.

[48] C. Pozrikidis. *Boundary Integral and Singularity Methods for Linearized Viscous Flow*. Cambridge University Press, 1992.

[49] E. M. Purcell. "Life at low Reynolds numbers". In: *Am. J. Phys.* 45 (1977), pp. 3–11.

[50] E. M. Purcell. "The efficiency of propulsion by a rotating flagellum". In: *Proceedings of the National Academy of Sciences* 94.21 (1997), pp. 11307–11311. ISSN: 0027-8424. DOI: 10.1073/pnas.94.21.11307. eprint: https://www.pnas.org/content/94/21/11307.full.pdf. URL: https://www.pnas.org/content/94/21/11307.

[51] M. RIVERO, J. MAGNAUDET, and J. FABRE. "Quelques résultats nouveaux concernant les forces exercées sur une inclusion sphérique par un écoulement accéléré". In: *Comptes rendus de l'Académie des sciences. Série 2, Mécanique, Physique, Chimie, Sciences de l'univers, Sciences de la Terre* 312.13 (1991), pp. 1499–1506.

[52] M. Sauzade, G. J. Elfring, and E. Lauga. "Taylor's swimming sheet: Analysis and improvement of the perturbation series". In: *Physica D: Nonlinear Phenomena* 240.20 (2011). Special Issue: Fluid Dynamics: From Theory to Experiment, pp. 1567–1573. ISSN: 0167-2789. DOI: https://doi.org/10.1016/j.physd.2011.06.023. URL: http://www.sciencedirect.com/science/article/pii/S0167278911001801.

[53] K. Seffen and R. McMahon. "Heating of a uniform wafer disk". In: *International Journal of Mechanical Sciences* 49 (2007), pp. 230–238.

[54] E. Setter, I. Bucher, and S. Haber. "Low-Reynolds-number swimmer utilizing surface traveling waves: Analytical and experimental study". In: *Phys. Rev. E* 85 (6 June 2012), p. 066304. DOI: 10.1103/PhysRevE.85.066304. URL: https://link.aps.org/doi/10.1103/PhysRevE.85.066304.

[55] J. D. Sherwood. "Resistance coefficients for Stokes flow around a disk with a Navier slip condition". In: *Physics of Fluids* 24.9 (2012).

[56] I. N. Sneddon. *Mixed boundary value problems in potential theory*. John Wiley, 1966.

[57] J. P. Tanzosh and H. A. Stone. "A general approach for analyzing the arbitrary motion of a circular disk in a Stokes flow." In: *Chemical Engineering Communications* 148-150 (1996), pp. 333–346.

[58] G. Taylor. "Analysis of the swimming of long and narrow animals". In: *Proceedings of the Royal Society of London. Series A. Mathematical and Physical Sciences* 214.1117 (1952), pp. 158–183. DOI: 10.1098/rspa.1952.0159. eprint: https://royalsocietypublishing.org/doi/pdf/10.1098/rspa.1952.0159. URL: https://royalsocietypublishing.org/doi/abs/10.1098/rspa.1952.0159.

[59] G. Taylor. "Analysis of the swimming of microscopic organisms". In: *Proceedings of the Royal Society of London A: Mathematical, Physical and Engineering Sciences* 209.1099 (1951), pp. 447–461. DOI: 10.1098/rspa.1951.0218. eprint: http://rspa.royalsocietypublishing.org/content/209/1099/447.full.pdf. URL: http://rspa.royalsocietypublishing.org/content/209/1099/447.

[60] C. J. Tranter. "A further note on dual integral equations and an application to the diffraction of electromagnetic waves". In: *Quarterly Journal of Mechanics and Applied Mathematics* 7.3 (1954), pp. 317–325.

[61] M. Uhlmann and J. Dušek. "The motion of a single heavy sphere in ambient fluid: A benchmark for interface-resolved particulate flow simulations with significant relative velocities". In: *International Journal of Multiphase Flow* 59 (2014), pp. 221–243. ISSN: 0301-9322. DOI: https://doi.org/10.1016/j.ijmultiphaseflow.2013.10.010. URL: http://www.sciencedirect.com/science/article/pii/S0301932213001559.

[62] G. N. Watson. *A trestise on the theory of bessel functions.* Cambridge University Press, 1944.

[63] W. Wittrick, D. Myers, and W. Blunden. "Stability of a bimetallic disk". In: *Quarterly Journal of Mechanics and Applied Mathematics* 6.1 (1953), p. 15.

[64] W. Zhang and H. A. Stone. "Oscillatory motions of circular disks and nearly spherical particles in viscous flows". In: *Journal of Fluid Mechanics* 367 (1998), pp. 329–358. DOI: 10.1017/S0022112098001670.